University of Cyprus

Department of Mechanical and Manufacturing Engineering

Computational and experimental analyses of cancer mechano-pathology

PhD *THESIS*

CHRYSOVLANTIS VOUTOURI

2018

Πανεπιστήμιο Κύπρου
Τμήμα Μηχανικών Μηχανολογίας
και Κατασκευαστικής

Computational and experimental analyses of cancer mechano-pathology

PhD *THESIS*

ΧΡΥΣΟΒΑΛΑΝΤΗΣ ΒΟΥΤΟΥΡΗ

Διατριβή η οποία υποβλήθηκε προς απόκτηση διδακτορικού τίτλου σπουδών στο Πανεπιστήμιο Κύπρου

2018

VALIDATION PAGE

Doctoral Candidate: Chrysovalantis Voutouri

Doctoral Thesis Title: Computational and experimental analyses of cancer mechano-pathology

This Doctoral Dissertation was submitted in partial fulfillment of the requirements for the degree of Doctor of Philosophy at the **Department of Mechanical and Manufacturing Engineering** and approved on the …….. by the **Examination Committee**.

Examination Committee:

Research Advisor:

Dr.Triantafyllos Stylianopoulos ……..……..……

Other Members:

Dr. Andreas Alexandrou ……...……

Dr.Loucas Louca ……..…….

Dr.Alkiviadis Tsamis ……..……..……

Dr. Leonidas Alexopoulos ……..…….....

DECLARATION OF DOCTORAL CANDIDATE

The present doctoral dissertation was submitted in partial fulfilment of the requirements for the degree of Doctor of Philosophy of the University of Cyprus. It is a product of original work of my own, unless otherwise mentioned through references, notes, or any other statements.

……

……

Περίληψη

Οι όγκοι παράγουν μηχανικές δυνάμεις κατά τη διάρκεια της ανάπτυξης και της εξέλιξης τους. Αυτές οι δυνάμεις είναι ικανές να συμπιέζουν αγγεία, μειώνοντας τα ποσοστά αιμάτωσης και οξυγόνου. Τόσο η μειωμένη αιμάτωση όσο και η αυξημένη πίεση του υγρού εμποδίζουν την μεταφορά φαρμακευτικών σκευασμάτων μέσω του αίματος, μειώνοντας την αποτελεσματικότητα της χημειοθεραπείας και νανοθεραπείας. Παρά τη μεγάλη σημασία του μικροπεριβάλλοντος για την παθολογία του καρκίνου, υπάρχουν λιγοστές μελέτες για τη μοντελοποίηση και πειραματική μέτρηση των μηχανικών ιδιοτήτων των όγκων και για το πώς αυτές οι παράμετροι επηρεάζουν την ανάπτυξη του όγκου. Σε αυτή την διδακτορική διατριβή αρχικά χαρακτηρίσαμε τις μηχανικές ιδιότητες καρκινικών όγκων και υπολογίσαμε το εύρος των αναπτυσσόμενων δυνάμεων. Στη συνέχεια, παρουσιάζονται στοιχεία για το πώς η χρήση φαρμάκων τα οποία σκοπό έχουν να μειώσουν τις δυνάμεις αυτές θα μπορούσαν να χρησιμοποιηθούν σε συνδυασμό με την χημειοθεραπεία για τη βελτίωση της αποτελεσματικότητας της θεραπείας. Τέλος, επικεντρωθήκαμε στην μελέτη της μοντελοποίησης των μηχανισμών αγγειογένεσης σε καρκίνους του εγκεφάλου (γλιοβλαστώματα), μέσω των οποίων τα καρκινικά κύτταρα μπορούν να οξυγονόνονται και κατ'επέκταση να διατηρούν την περαιτέρω ανάπτυξη του όγκου.

Στο πρώτο κεφάλαιο πραγματοποιήσαμε πειράματα μηχανικής συμπίεσης σε δύο τύπους καρκινικών όγκων και διαπιστώσαμε ότι η πειραματικά απόκριση προσαρμόζεται καλύτερα σε μια καταστατική εξίσωση εκθετικής μορφής. Ακολούθως, ενσωματώσαμε την καταστατική αυτή εξίσωση, καθώς και άλλες κοινές για συνδετικούς ιστούς εξισώσεις σε ένα υφιστάμενο μοντέλο ανάπτυξης καρκινικών όγκων. Παρατηρήθηκε ότι οι αναπτυσσόμενες δυνάμεις καθώς και ο ρυθμός ανάπτυξης του όγκου ήταν ανεξάρτητος από την επιλογή της καταστατικής εξίσωσης, αλλά εξαρτόταν έντονα από τις μηχανικές αλληλεπιδράσεις με τον περιβάλλοντα φυσιολογικό ιστό. Στο δεύτερο κεφάλαιο, μελετήσαμε την δυνατοτητα χρήσης του αντι-ινωτικού φαρμάκου Tranilast (Rizaben®) για την μείωση των μηχανικών δυνάμεων σε δύο μοντέλα όγκων του μαστού. Αποδείξαμε πειραματικά ότι το Tranilast μειώνει τις μηχανικές δυνάμεις, βελτιώνει την αιμάτωση του όγκου και ενισχύει σημαντικά την αποτελεσματικότητα των εγκεκριμμένων φαρμάκων για καρκίνους του μαστού: doxorubicin, Abraxane® και Doxil®. Στο τρίτο κεφάλαιο, σχεδιάσαμε νέα πειράματα, χρησιμοποιώντας τέσσερα μοντέλα καρκινικών όγκων, για να μετρήσουμε την μηχανική τάση που αναπτύσσεται λόγω της διόγκωσης του υαλουρονικού

οξέως στο εσωτερικό των όγκων και για να συσχετίσουμε την τάση αυτή με τα δομικά συστατικά των καρκινικών όγκων, καθώς και της αιμάτωση τους. Τα δεδομένα μας αποκάλυψαν μια αντίστροφη σχέση μεταξύ της αιμάτωσης και της τάσης διόγκωσης του όγκου, υποδηλώνοντας ότι η μείωση της τάσης διόγκωσης, που μπορεί να προέλθει με μείωση των επιπέδων υαλουρονικού οξέως. Στο τέταρτο κεφάλαιο, χρησιμοποιώντας πειραματικά δεδομένα από δύο μοντέλα καρκίνου του μαστού και χορηγώντας στους όγκους δύο κλινικά εγκεκριμένα αντι-ινωτικά φάρμακα (tranilast and pirfenidone), διαπιστώσαμε ότι η συσσώρευση των δυνάμεων σε όγκους συσχετίζεται με την περιεκτικότητα τους σε υαλουρονικό οξύ και με το μέτρο ελαστικότητας τους. Τέλος, χρησιμοποιώντας μια σειρά από πειραματικά δεδομένα σε γλοιώματα και μεταστάσεις στον εγκέφαλο από κύτταρα καρκίνου του μαστού, προερχόμενα από το εργαστήριο του καθηγητή Rakesh K. Jain του Γενικού Νοσοκομείου της Μασσαχουσέτης των ΗΠΑ αναπτύχθηκε ένα μαθηματικό μοντέλο για τους μηχανισμούς αγγιογένεσης στους όγκους αυτούς και προτάθηκαν μεθοδολογίες για την επιτυχή στόχευση των μηχανισμών αυτών που μπορούν να οδηγήσουν σε αποτελεσματικότερες θεραπείες.

Abstract

Cancer mechanopathology deals with the causes, consequences and remedies for the effects of tumor mechanics on the pathology of cancer and focuses on the development of therapeutic strategies to reengineer solid tumors in order to improve therapy. Specifically, solid tumors generate mechanical forces during growth and progression. These forces are able to compress blood and lymphatic vessels, increasing the tumor interstitial fluid pressure, reducing perfusion rates, and creating hypoxia. Both hypo-perfusion and elevated fluid pressure hinder delivery of blood-borne therapeutic agents, lowering the efficacy of chemo- and nanotherapies. Despite the great importance of the mechanical microenvironment to the pathology of cancer, there are limited studies for the constitutive modeling and the mechanical properties of tumors and on how these parameters affect tumor growth. In this thesis, we characterized the tissue-level mechanical stresses found in tumor, namely i) the externally applied stress ii) the swelling stress and iii) the growth-induced or residual stress. Subsequently, we tested the hypothesis that alleviation of these mechanical stresses repurposing clinically approved anti-fibrotic drugs can be used in combination with chemotherapy to improve treatment efficacy. Finally, we developed mathematical models for the study of the mechanisms of angiogenesis in brain tumors, incorporating the effect of co-option of the host vasculature by cancer cells, which is a strategy with which some cancer cells can sustain tumor progression.

In the first chapter, we performed unconfined compression experiments in two tumor types and found that the experimentally measured stress-strain response is better fitted to an exponential constitutive equation and we incorporated these constitutive equations into a biomechanical model of tumor growth. We found that the evolution of stress during progression and the growth rate of the tumor are independent from the selection of the constitutive equation, but depend strongly on the mechanical interactions with the surrounding host tissue. In the second chapter, using two orthotopic mammary tumor models, we demonstrate that the clinically approved anti-fibrotic drug Tranilast can be repurposed to reduce intratumoral mechanical stresses, improve tumor perfusion and significantly enhance the efficacy of the common anti-cancer drugs: doxorubicin, Abraxane and Doxil. In the third chapter, we designed an experimental strategy, using four orthotopic tumor models, to measure the stress owing to the swelling of hyaluronan and related swelling to the organization of collagen and hyaluronan in the tumors, as well as to tumor perfusion. In the fourth chapter, using experimental data from two orthotopic breast

tumor models and treating tumors with two clinically approved anti-fibrotic drugs (tranilast and pirfenidone), we found that accumulation of residual forces in tumors are associated with hyaluronan content and the elastic modulus of the tumor. Finally, in collaboration with the team of Professor Rakesh K. Jain at Massachusetts General Hospital, we developed a mathematical model for the angiogenic mechanisms of brain tumors, which was validated using a series of experimental data in orthotopic gliomas and brain metastasis from breast cancer cells collected from the group of Professor Jain. The model also proposed strategies for targeting the angiogenic mechanisms in order to improve therapy.

Acknowledgments

I had the great honour and luck to work with Dr. Triantafyllos Stylianopoulos for about six years and all this time I have never doubted that he was the best gifted and insightful advisor I could have asked for. He gave me actuation for started graduate program and i would like to express for the continuous support of my Ph.D study and related research, for his patience, motivation, and immense knowledge. I owe all I have achieved these years to him. I am thankful to him for all his help, not only as an advisor but also as a father through all these years of working together and i look forward working with him again in the future.

I also thank all the members of the Cancer Biophysics laboratory's group for their friendship. Working in the lab was always fun and I am happy for being part of it. I am particularly thankful to Dr. Christiana Polydorou and Dr. Vasiliki Gkretsi for sharing their fluorescent immunohistochemistry and in vitro skills and Dr. Panos Papageorgis and Dr. Fotios Mpekri who taught me and helped me so much with all techniques in animal studies.

Finally, my family should be acknowledged for their support and love all these years.

Contents

1 Introduction

The tumor microenvironment and pathophysiology

Finding the cure for cancer is a true challenge undertaken by hundreds of research groups worldwide, each one focusing on different aspects of the disease in an attempt to better understand the mechanism of cancer progression and identify a more effective therapy. From the mechanical point of view, all tumor components interact with each other resulting in generation of mechanical stresses between them that could elucidate disease pathogenesis. A cancerous region is typically composed of the blood and lymphatic vessels, the interstitial space, the cancer cells and the stromal/healthy cells (**Fig. *1-1***). The blood vessels are responsible for the supply of blood, nutrients and drugs to the tumor. Just like the healthy vessels, tumor vessels have pores in their walls, permitting the extravasation of blood from the vessels. The area outside the vessels, is called the interstitial space. The interstitial space, is consisted mainly of collagen and hyaluronan fibers, which form a dense fiber network, with a density that varies depending on the tumor type. Apart from the vascular network, there are also the lymphatic vessels. The lymphatic vessels are responsible for the absorption of the excess amount of blood plasma and other fluids that enter the interstitial space through the pores of the blood vessels. In this way any excess fluid is removed from the interstitial space and therefore the hydrostatic pressure in the healthy regions, is kept at 0 mmHg.

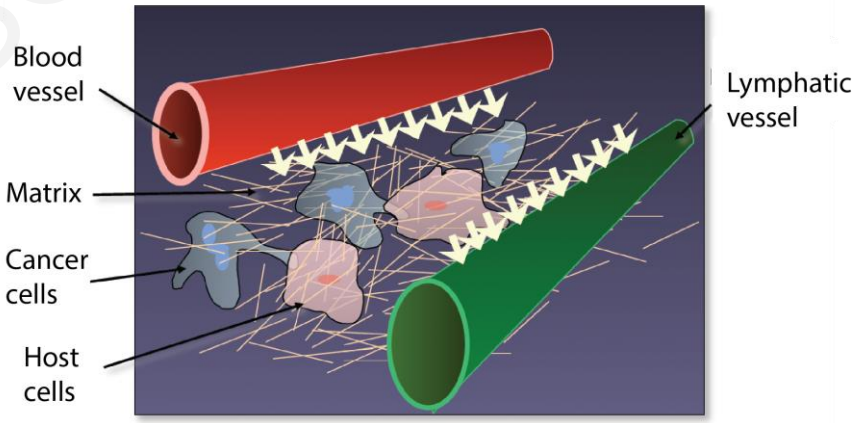

***Fig.* 1-1.** *A simplified model of the tumor microenvironment*

Abnormal vascular network and vessel wall structure

The cardiovascular system (heart, arteries, veins and capillaries) controls the blood circulation and the transportation of nutrients and other compounds. The arteries carry the oxygenated blood towards all the organs of the human body, and then branch into smaller arterioles and capillary vessels (**Fig. *1-2*** A). The capillaries, are the vessels with the smallest diameter, and have very thin walls. Through the capillary walls, the blood compounds are transferred to the cells. The non-oxygenated blood is removed from the cells through the capillary vessels, passes on to the venules, and then to the veins, from where it is carried back to the heart and sent to the lungs for oxygenation. However, in contrary to the normal tissues, blood vessels in tumor areas have a highly irregular architecture, due to the aggressive progression of the tumor. Therefore, the hierarchy in the branching of the normal vessels is not observed in the cancerous vessels. Tumor vessels have a chaotic and disorganized structure, and their diameter may vary considerably [4]. **Fig. *1-2***B depicts a tumor angiography, where the abnormal structure of the tumor vessels can be clearly distinguished from the organized structure of the surrounding healthy vessels.

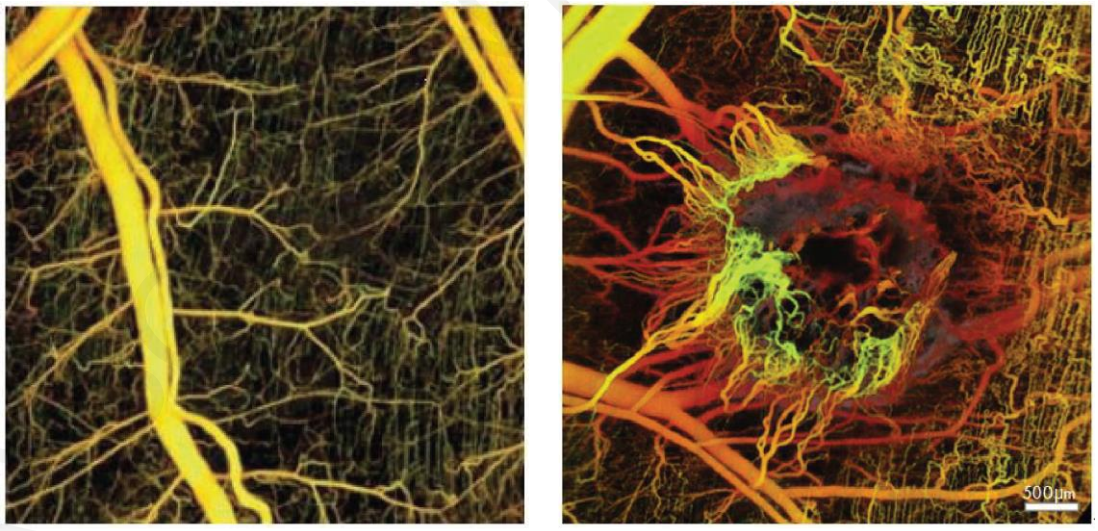

***Fig.* 1-2.** *Comparison of the vascular network in (A) normal tissues (B) tumor tissues [1].*

The endothelial cells are located in the inside of the blood vessels and form the vessel lumen, through which the blood flows. In healthy tissues, the endothelial cells are well connected with each other, leaving only very small gaps (pores) in their structure - in the

order of 7-12nm - allowing the blood to be normally transported through the vascular network **Fig. *1-3***A.

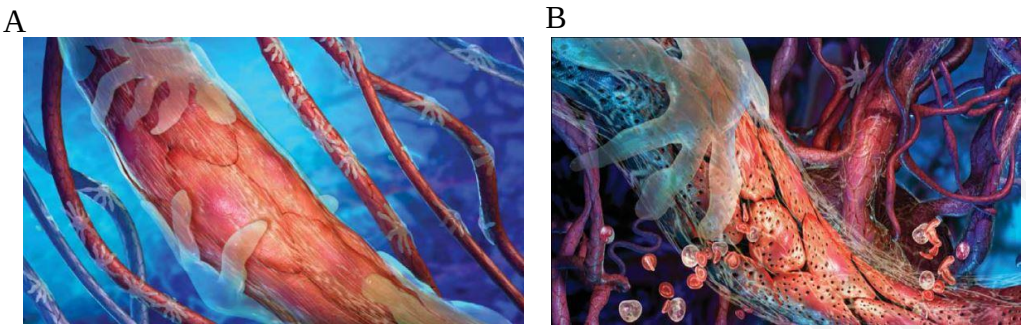

Fig. *1-3*. (A) Normal vessel wall (B) Tumor vessel wall [3]. Tumor vessels are leaky (hyper-permeable) allowing for fluid communication between the vascular and interstitial (extravascular) space of the tumor.

Tumor vessels generally lack the endothelial membrane, whose function is to hold the endothelial cells in their proper position. This creates larger openings on the vessel lumen, allowing the blood to extravasate from the vessels and enter the tumor interstitial space **Fig. *1-3***B. This usually leads to an increase in the amount of plasma that enters the interstitial space and thus, rises the interstitial fluid pressure (IFP). Indeed, the uniform elevation of the tumor interstitial space is a hallmark of tumor pathophysiology.

In healthy capillary vessels, the pore size diameter is usually 7-12nm, whereas in tumor capillaries the pore size is much larger, mainly due to the discontinuity of the endothelial cells. The pore diameter in tumor vessels varies within a range of 100 to 780nm. It is possible though, that the pores reach a diameter up to 2μm [5]. The lymphatic vessels are responsible for the absorption of the excess fluid (blood and other substances) from the interstitial space, in order to maintain normal interstitial pressure levels and avoid the creation of edema. However, in tumors, the development of mechanical stresses causes the compression of the lymphatic vessels, which become dysfunctional, leading to inadequate drainage of fluid from the tumor interior. Dysfunction of lymphatic vessels is another abnormality of the tumor microenvironment that along with vessel leakiness contributes to elevation of interstitial fluid pressure.

Abnormal extracellular matrix (ECM)

The interstitial (i.e., extravascular) space of tumors consists of the various cells and the extracellular matrix (ECM). The ECM in tumors is composed of a dense network of collagen and hyaluronan fibres (**Fig. *1-4***), which hinders the penetration of nano-drugs within the tumor and also decreases the hydraulic conductivity of the tissue, which defines the ease by which interstitial fluid percolates through the interstitial tumor space. The low hydraulic conductivity is another reason that along with vessel leakiness and lymphatic dysfunction causes IFP elevation.

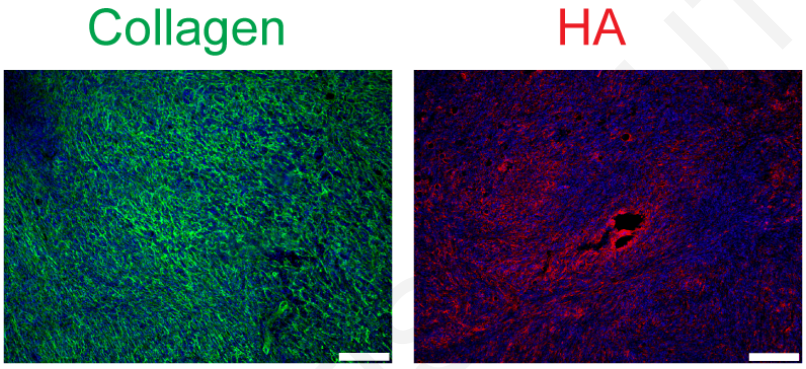

Fig. *1-4*. Immunofluorescence staining for collagen (green), hyaluronan (red) and Dapi (blue) of a tumor section.

Mechanical Stresses

Mechanical stresses in tumors, similar to other tissues, stem either from the solid components of a tumor, mainly cancer and stromal cells and the dense ECM or from the interstitial fluid. In the former case, the stress of the solid, structural tumor components is known as solid stress, whereas the stress from the interstitial fluid is referred to as the interstitial fluid pressure (IFP) [6].

Intratumoral solid stresses can be divided to three types: i) externally applied stress exerted by the surrounding host tissue on the tumor due to mechanical interactions between the two tissues [6-8], ii) growth-induced or residual stress which are the stresses that remain in the tumor when it is excised, and external loads are removed [2], and iii) swelling stress, which is developed owing to the negatively charged hyaluronan chains that exert repulsive electrostatic forces on each other as they are closely packed in the dense tumor ECM, causing tissue swelling [9,10].

The stresses of the fluid phase of tumors mainly consist of the hydrostatic fluid pressure of the tumor interstitial space as well as the vascular pressure and the fluid shear on the luminal side of the tumor blood vessel wall [11-13]. Within tumor interior, the IFP is uniformly elevated and can be as high as the vascular pressure [11,13]. **Fig. *1-5***[11,14].

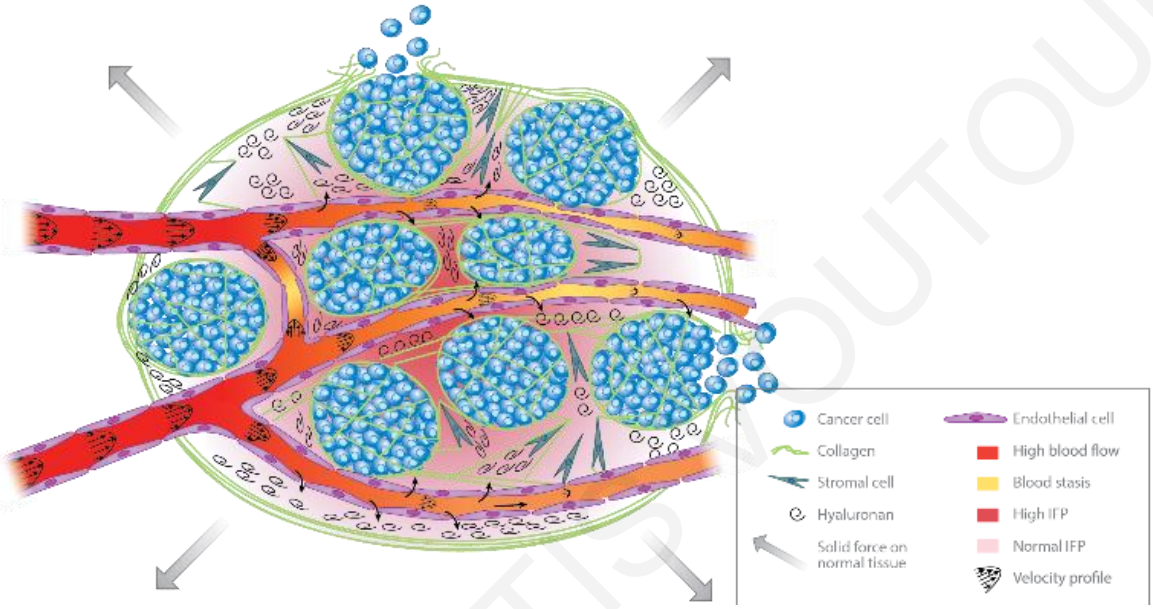

Fig. *1-5*. Schematic of the tumor mechanical microenvironment. Cancer cells along with cancer associated fibroblasts (stromal cells) stretch collagen fibers and compress hyaluronan storing growth-induced solid stress. This stress can compress or even collapse intratumoral vessels reducing blood flow. The remaining uncompressed vessels are often leaky resulting in excessive fluid crossing the vessel wall and contributing to elevated interstitial fluid pressure. Vessel leakiness further reduces perfusion and along with vessel compression can cause blood stasis. At the macroscopic scale the tumor pushes against the surrounding normal tissue, which in turn restricts tumor expansion [13].

Growth-induced stress is believed to be generated owing to the fact that solid stresses in tumors are contained within viscoelastic structural components of the tissue, and thus, some stresses are maintained even if a tumor is excised. Mechanical interactions that could generate growth-induced stress could be the stretching and remodelling of extracellular fibers by cancer cells or activated cancer-associated fibroblasts (CAFs) and the hydration of hyaluronan that resists compressive forces within the tumor. Growth-induced stress in tumors has been quantified in previous research by excising tumors and making a cut along their long axis at about ~80% of their thickness [2]. The tumor opens

up as a result of stress release and tissue relaxation and the resulting opening is measured, called tumor opening hereafter (**Fig. *1-6*** and **Fig. *1-7***).

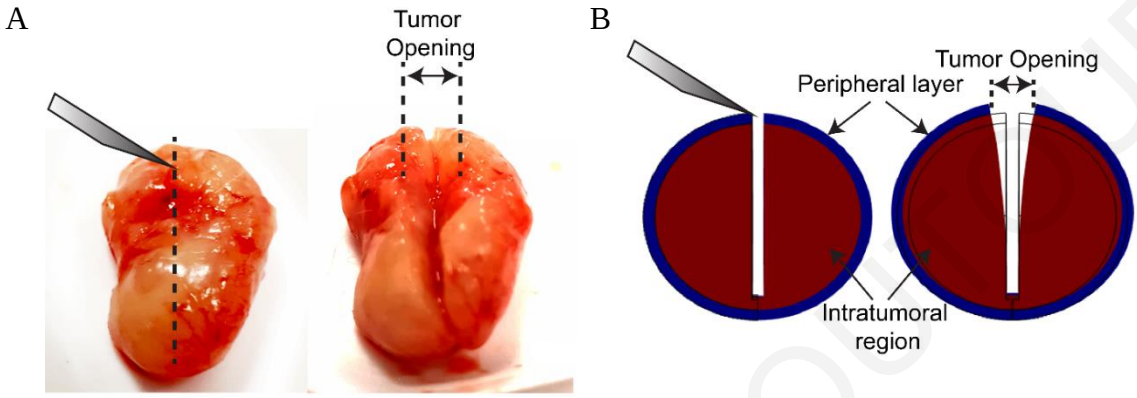

Fig. *1-6*. Schematic of tumor opening experiment and calculations. (A): Typical experimental procedure showing the tumor before and after the cut has been made. The measured tumor opening appears in the figure. (B): Representative computational results in the beginning and at the end of the simulation. In the model, the tumor consists of two domains, the tumor and a peripheral layer with thickness 5% of the tumor diameter. The simulations were used for the calculation of the growth-induced stress from the measured displacement/opening of the tumor.

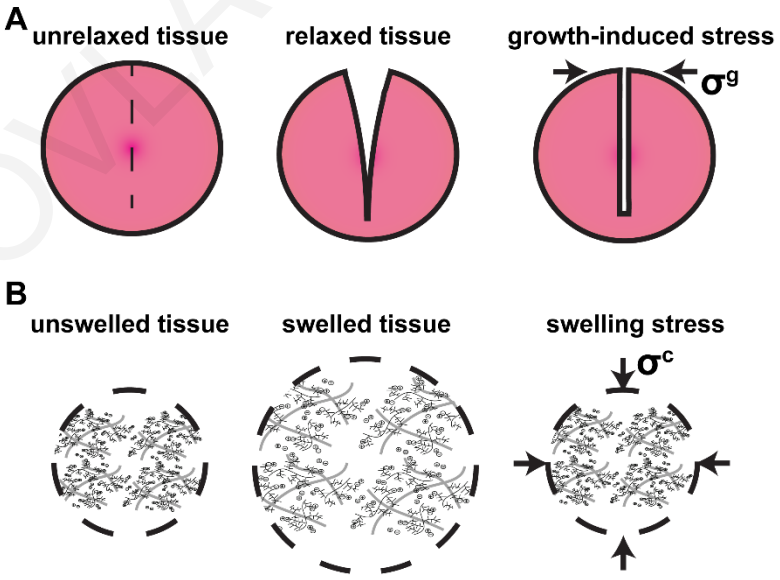

Fig. *1-7*. Schematic of growth-induced stress and swelling stress. (A): Growth-induced stress/residual stress, $\boldsymbol{\sigma}^g$, equals to the stress required to close the tumor after tumor

relaxes and stress is released. (B**):** Swelling stress, $\boldsymbol{\sigma^c}$, is the stress required to compress tumor to initial radius from swelled tissue condition.

Tumors rich in hyaluronan (e.g. breast and pancreatic cancers and sarcomas) are characterized by a high-net negative charge density owing to the negatively charged groups of hyaluronan, quantified as the fixed charge density (FCD) [15]. Because of its negative charge, hyaluronan immobilizes interstitial fluid forming gel-like regions within the tissue [16]. Repulsive electrostatic forces among the closely spaced negative groups cause the swelling of these regions - an effect known as chemical expansion - which in turn generates a swelling solid stress (or swelling stress for brevity), since it is generated by solid components of a tumor (**Fig. *1-7***B). IFP is also elevated owing to the hyper-permeability of some tumor blood vessels, which allows excessive plasma to enter the tumor, and due to the dysfunction of most intratumoral lymphatic vessels, which cannot drain adequately the interstitial fluid [11,14]. Additionally, in hyaluronan-rich tumors, because of the presence of FCD and in order for the tumor to meet the electro-neutrality condition, a large number of counter ions must be present within the interstitial space. Therefore, there might be an excess of cations within the tumor interstitial space, creating a Donnan osmotic fluid pressure difference between the internal and external environment of the tissue [17,18].

The swelling stress is quantified as the stress required to compress a swollen sample from thickness δ to δ_{ref} **Fig. *1-8***. δ_{ref} is defined as the thickness attained when NaCl concentrations are isotonic enough to shield electrostatic interactions, $\delta > \delta_{ref}$ tumor swelling in hypotonic solutions (the thickness of the sample increases). To measure swelling stress a tumor specimen is placed in a confined chamber, NaCl solution of specified concentration is added causing the swelling of the tissue and a load cell measures the force that is developed to keep the tissue to its initial height **Fig. *1-8***.

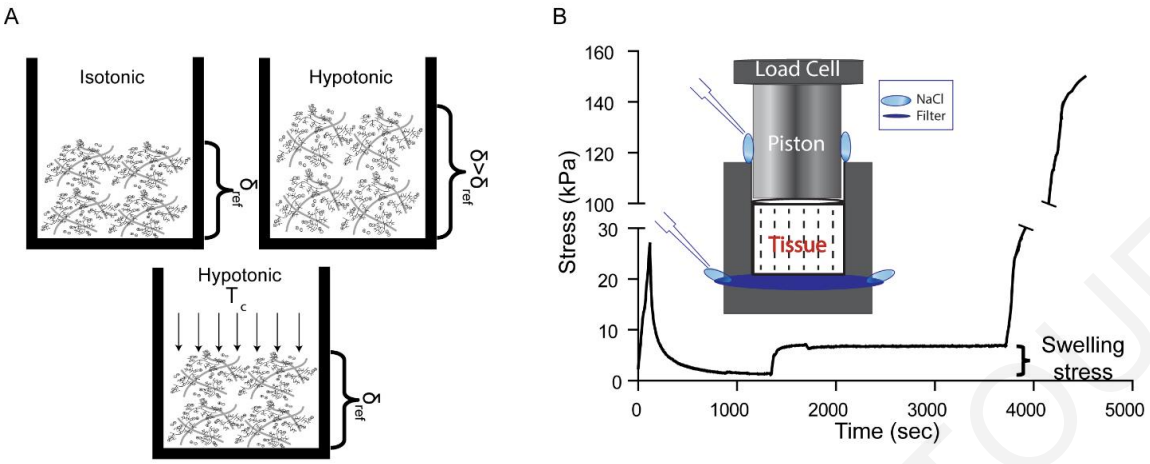

Fig. *1-8.* Measuring tumor swelling. (A) δ_{ref} is defined as the thickness attained when NaCl concentrations are isotonic enough to shield electrostatic interactions, $\delta > \delta_{ref}$ tumor swelling in hypotonic solutions (the thickness of the sample increases), the stress required to compress the sample from thickness δ to δ_{ref} defines the swelling stress, T_c. (B) The tumor specimen was initially compressed to 10% strain and allowed to relax. Subsequently, NaCl solution (hypotonic) of specified concentration was added causing the swelling of the tissue, which reached a new equilibrium. Finally, the specimen was compressed for another 20% strain. The difference in the stress between the two equilibriums was quantified as the swelling stress. Islet shows a schematic of the experimental set up.

Impact of mechanical stresses on tumor growth and response to treatment

Elevated solid and fluid stresses determine in large part tumor progression and response to treatment [13,19]. On one hand, elevated solid stresses can directly compress cancer cells to reduce their proliferation rate and increase their invasiveness and metastatic potential [20-25]. These stresses can also compress intratumoral blood and lymphatic vessels and thus, cause hypoxia and hypo-perfusion **Fig. *1-9*** [6,26,27].

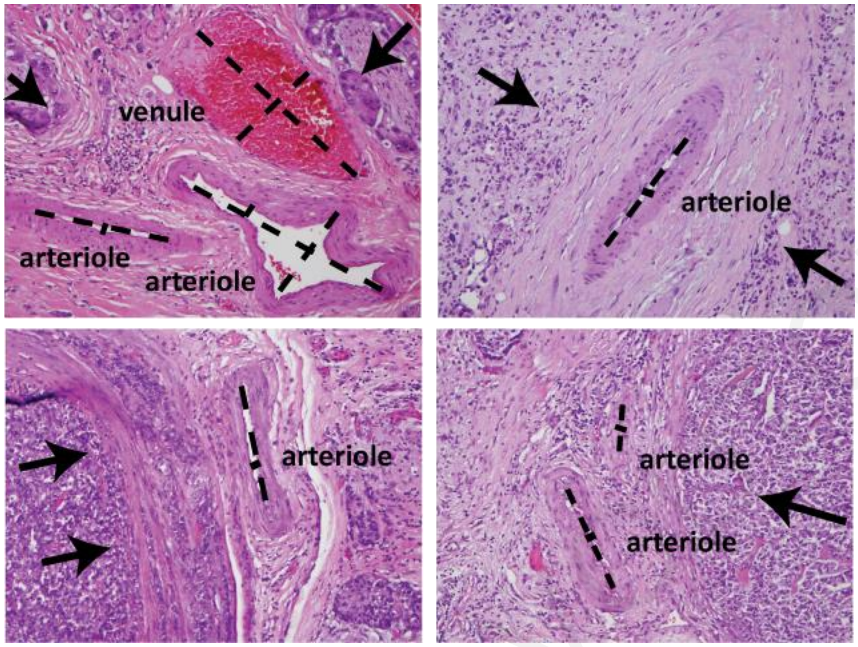

Fig. *1-9*. Histological section of human tumors show the deformation of peritumoral arterioles and venules [2]. Arrows show the position of cancer cells.

Hypoxia, among other effects, imposes a survival advantage for cancer cells, enhances their ability to invade and metastasize, harbors the cancer stem cells and compromises the efficacy of radiotherapy [28]. Hypo-perfusion drastically reduces the systemic delivery of drugs to the tumor site and consequently, the efficacy of chemo- and nanotherapeutics [29]. On the other hand, elevated IFP poses an additional barrier to the delivery of nano-scale drugs and facilitates transport of growth factors and cancer cells from the tumor to the surrounding tissue fueling tumor growth, progression and lymphatic metastasis [30,31].

Stress alleviation strategy

Alleviation of solid and fluid stresses by targeting specific components of the tumor microenvironment has emerged as a new therapeutic strategy to enhance cancer therapy based on promising preclinical evidence [2,29,32-36] and the first clinical trial being already in progress (clinicaltrials.gov identifier NCT01821729). Preclinical studies have shown that therapeutic depletion of the dense ECM through alleviates mechanical stresses, and thus, decompresses tumor blood vessels, improving perfusion and the efficacy of chemotherapy **Fig. *1-10*** [32-37].

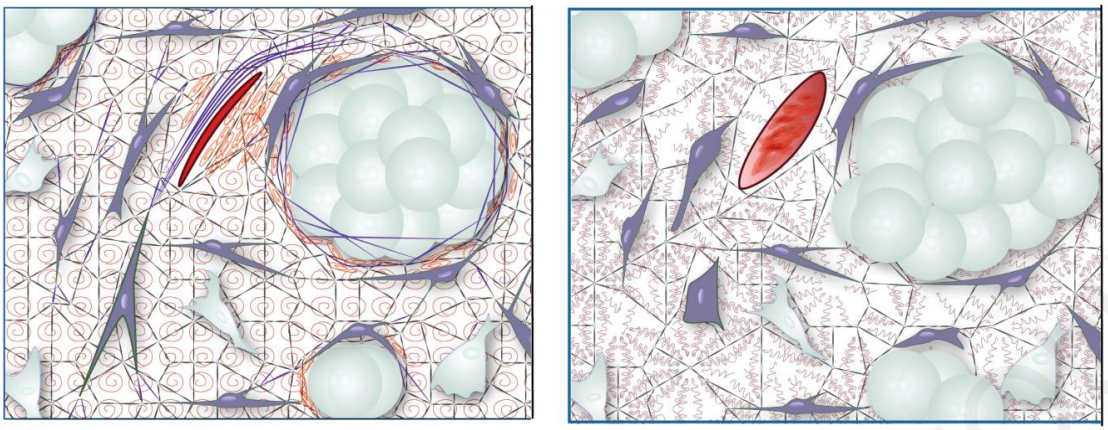

Fig. *1-10*. Left panel: In an untreated tumor, proliferating cancer cells and activated fibroblasts (stromal cells) deform the extracellular matrix resulting in stretched collagen fibers, compressed hyaluronan (HA) and deformed cells – all storing stress. This stress compresses blood vessels reducing drug delivery. Right Panel: Depleting collagen alleviates the stress that was held within these fibers as well as relaxes activated fibroblasts and compressed cancer cells. As a result, collapsed vessels re-open, become perfused and increase delivery of drugs [2].

Despite these encouraging findings, there are no established guidelines on the use of stress alleviation strategies yet, owing in large part to our limited knowledge of tumor mechanical behavior and its relation to tumor pathophysiology [7,13,38]. Therefore, it is high time for in-depth understanding, analysis and better characterization of all mechanical components of the tumor microenvironment that contribute to the acquisition of malignant properties and drug resistance in order to develop new and effective therapeutic interventions.

2 Chapter 2: Role of constitutive behavior and tumor-host mechanical interactions in the state of stress and growth of solid tumors

This research has been published in PLoS ONE: Voutouri C.*, F. Mpekris*, P. Papageorgis, A.D. Odysseos, and T. Stylianopoulos. The role of constitutive behavior and tumor-host mechanical interactions in the state of stress and growth of solid tumors. PLoS One 9(8): e104717. * Equal contribution.

2.1 **Introduction**

Despite the importance of solid stresses on tumor progression and treatment, there is no technique to date to measure solid stress levels in vivo. Therefore, calculations of the evolution and magnitude of stress in tumors is performed only with the use of mathematical modeling. Biomechanical models of tumor growth have been developed by our research group and other researchers, which have been successful in predicting qualitatively the overall mechanical response of tumors [2,6,39-43]. These models, however, face certain limitations that might affect the accuracy of the calculations. There are very few studies to measure the mechanical properties (e.g. stiffness) of solid tumors [44-46] and little work has been performed for their constitutive modeling compared to other biological tissues such as arteries and heart valve leaflets. As a result, general constitutive equations, particularly the neo-Hookean and the Blatz-Ko material, are being used to describe the elastic response of tumors with limited experimental validation and with the mechanical properties taken either arbitrarily or from the few published experimental data. Therefore, the uncertainty of the selection of a proper constitutive equation as well as the corresponding mechanical properties can compromise the accuracy of biomechanical models and thus, our ability to better understand the tumor mechanical microenvironment. Furthermore, while it has been shown with *in vitro* experiments in cancer cell spheroids that the mechanical properties of the host tissue affect the state of stress and the growth of the tumor [20,21,24], the underlying mechanisms for the mechanical interactions between the tumor and the host tissue are not clear yet. In addition,

there are limited studies for the constitutive modeling and the mechanical properties of tumors.

To this end, we performed unconfined compression experiments in two different tumor types and measured the elastic modulus from the experimental stress-strain curves. Subsequently, in order to determine a proper constitutive equation and the corresponding values of the mechanical properties, we simulated the experimental procedure and fitted the stress-strain data to three constitutive models: the neo-Hookean and the Blatz-Ko models that are widely used for tumors and an exponential equation that has been previously developed to model soft biological tissues. Finally, we incorporated this information into a biomechanical model of tumor growth to study the evolution of solid stress in tumors during progression and the contribution of the host tissue to the tumor's state of stress and growth rate.

2.2 **Methods**

2.2.1 Biomechanical modeling of tumor growth.

Solid stress in a tumor has as components: the residual "growth-induced" stress, which accumulates in tumors due to the generation of internal forces among the structural constituents of the tumor and the externally applied stress due to mechanical interactions with the host tissue [6]. To model the growth and mechanical behavior of tumors the multiplicative decomposition of the deformation gradient tensor, **F**, was used [47], a methodology that has been applied successfully to solid tumors [6,39,43,48-50] as well as to other soft tissues [51,52]. The model considered only the solid phase of the tumor and accounted for i) tumor growth, ii) generation of residual, growth-induced stresses and iii) mechanical interactions between the tumor and the surrounding normal tissue. Therefore, **F** was divided into three components:

$$\mathbf{F} = \mathbf{F}_e\mathbf{F}_g\mathbf{F}_r \tag{2.1}$$

where $\mathbf{F_e}$ is the elastic component of the deformation gradient tensor and accounts for mechanical interactions with the surrounding normal tissue or with any other external stimulus, $\mathbf{F_g}$ is the component that accounts for tumor growth and $\mathbf{F_r}$ is the component that accounts for the generation of residual stresses **Fig. *2-1***.

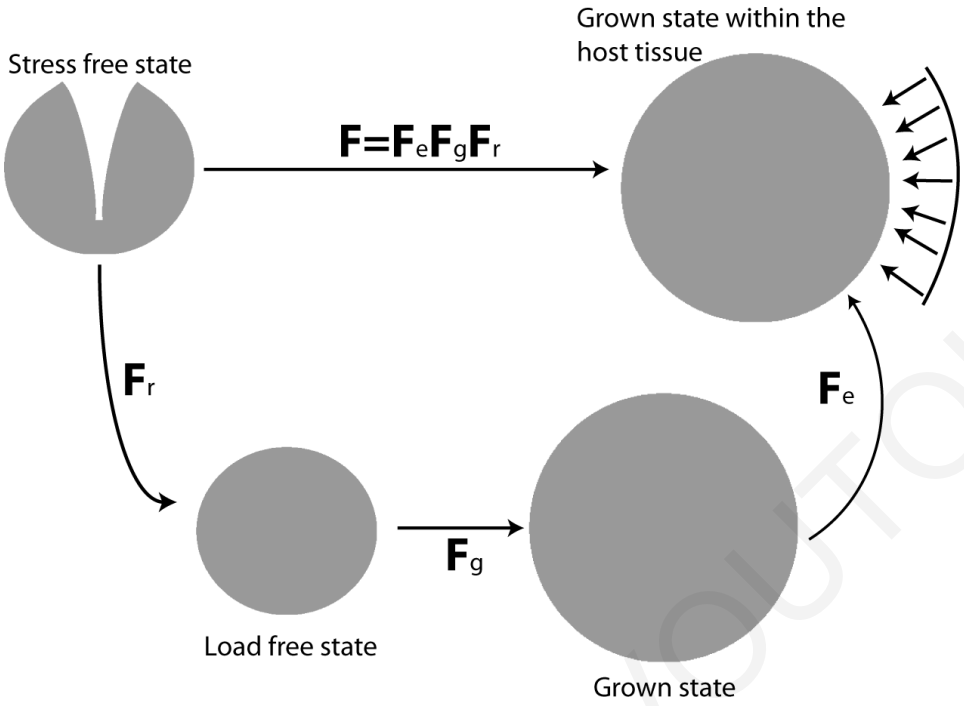

Fig. *2-1*. Multiplicative decomposition of the deformation gradient tensor. The stress free state corresponds to an excised tumor having the growth-induced (residual) component of the solid stress released [2,6]. The load free state corresponds to an excised tumor currying no external loads but holds residual stress, described by $\mathbf{F}_r$. The grown state corresponds to the volumetric growth of the tumor, which is described by $\mathbf{F}_g$ and the grown state within the host tissue corresponds to the final configuration of the grown tumor accounting for external stresses (arrows) by the host tissue and described by $\mathbf{F}_e$.

We measured and quantified residual stresses in tumors in previous research [2,6,53]. In this analysis, tumors did not exhibit significant levels of residual stress, and thus we set $\mathbf{F_r} = \mathbf{I}$.

Tumor growth was taken to be isotropic and the growth component $\mathbf{F_g}$ was given by:

$$\mathbf{F}_g = \lambda_g \mathbf{I}, \tag{2.2}$$

where λ_g is the growth stretch ratio. The growth stretch ratio was described by a phenomenological Gompertzian equation expressed in differential form as [6]:

$$\frac{d\lambda_g}{dt} = -a\lambda_g \log\left(\lambda_g / \lambda_{\max}\right), \tag{2.3}$$

where t is the time, a describes the growth rate of the cells and λ_{max} is a maximum growth stretch ratio. We further assumed that the parameter a depends on the levels of solid stress through a linear relationship [41]:

$$a = a_0\left(1+\beta\bar{\sigma}\right) \tag{2.4}$$

where a_0 is the growth rate at zero stress, β is a constant that describes the dependence of a on stress and $\bar{\sigma}$ is the bulk solid stress calculated as the average of the radial, σ_{rr}, and circumferential ($\sigma_{\theta\theta}, \sigma_{\phi\phi}$) components of the Cauchy stress tensor (i.e., $\bar{\sigma} = \left(\sigma_{rr}+\sigma_{\theta\theta}+\sigma_{\phi\phi}\right)/3$).

Finally, three constitutive equations, commonly used for the elastic response of soft biological tissues were tested: the compressible neo-Hookean model, the Blatz-Ko model and an exponential constitutive equation[54]. The strain energy density functions, *W*, of the equations are:

neo-Hookean:

$$W = 0.5\mu\left(-3+\mathrm{II}_1\right)+0.5\kappa\left(-1+J_e\right)^2 \tag{2.5}$$

Blatz-Ko:

$$W = \frac{G_t f}{2}\left(I_1-3-\frac{2}{q}\left(I_3^{q/2}-1\right)\right)+\frac{G_t(1-f)}{2}\left(\frac{I_2}{I_3}-3-\frac{2}{q}\left(I_3^{-q/2}-1\right)\right) \tag{2.6}$$

exponential:

$$W = A_1(\mathrm{e}^{C_1(-3+\mathrm{II}_1)}-1)+A_2(-1+J_e)^2 \tag{2.7}$$

where the mechanical properties of the neo-Hookean model are the shear modulus μ and bulk modulus κ. The properties of the Blatz-Ko model are the shear modulus G_t, $f \in [0\ 1]$ and $q < 0$ are dimensionless parameters. For isotropic materials *f=1*, and thus only the first term of the right-hand side of Eq. 6 was considered in our study. The parameters of the exponential equation are the constants A_1, A_2 and C_1. J_e is the determinant of the elastic deformation gradient tensor $\mathbf{F_e}$ and $II_1 = I_1 J_e^{-2/3}$. I1, I2 and I3 are the invariants of the right Cauchy-Green deformation tensor, which is evaluated from the elastic part of the deformation gradient tensor, $\mathbf{F_e}$.

The Cauchy stress tensor, $\boldsymbol{\sigma}$, was calculated by the strain energy density function as [55]:

$$\boldsymbol{\sigma} = J_e^{-1}\mathbf{F}_e \frac{\partial W}{\partial \mathbf{F}_e^T} \tag{2.8}$$

Finally, the linear momentum balance was solved assuming a quasi-static problem in the absence of body forces:

$$\nabla \cdot \boldsymbol{\sigma} = \mathbf{0} \tag{2.9}$$

A finite element model was constructed in COMSOL to solve Eqs.(2.1)-(2.9). A detailed description of the implementation of the model can be found in the Supplementary Information.

2.3 Results

2.3.1 Ex vivo stress-strain response is highly nonlinear

The experimental results of the unconfined compression experiments for the individual tumors and for the two tumor types are shown in **Fig. *2-2***. The equilibrium stress-strain response is highly nonlinear in most of the specimens even at the low range of strain employed in the study. The data are typical of soft biological tissues, consisting of a toe region at lower strains and a linear region at higher strains. The elastic modulus was measured from the slope of the linear part of the curves and found to be 288.3 ± 45.5 kPa for the MCF10CA1a tumors and 186.1 ± 25.9 kPa for the SW620 tumors. The difference between the two groups was not statistically significant (p = 0.065).

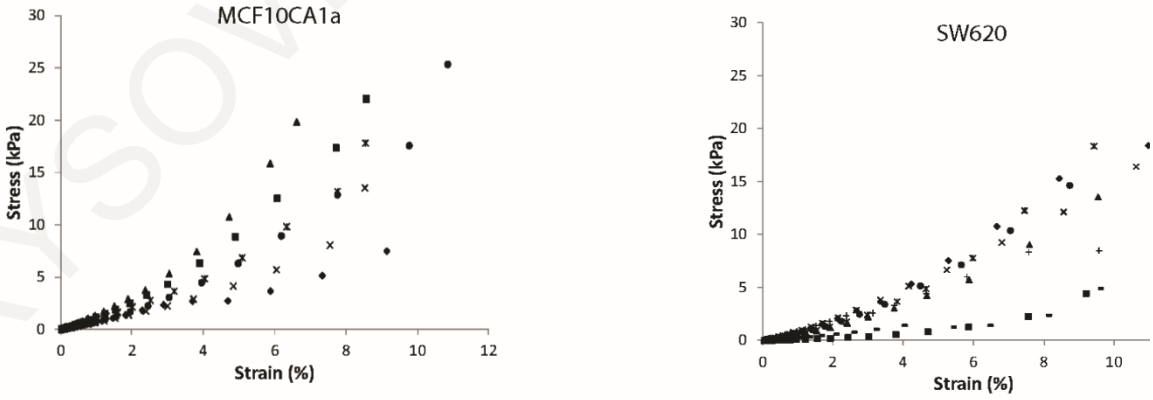

Fig. *2-2*. Experimentally measured elastic stress-strain response of MCF10CA1a and SW620 tumors in unconfined compression. Data show individual tumor behavior.

2.3.2 An exponential constitutive equation better describes tumor's ex vivo mechanical behavior

Subsequently, the biomechanical model was employed to simulate the unconfined compression experiment in order to indentify the most suitable constitutive equation as well as the values of the mechanical properties that provide the best fit to the experimental data. For these simulations $\mathbf{F}_g = \mathbf{I}$, because the experiment was performed *ex vivo* and thus, $\mathbf{F} = \mathbf{F}_e$ in Eq. (2.1) describes the elastic deformation of the tumor during the simulated compression experiment. A three-dimensional finite element model of orthogonal geometry, same in size as that of the real specimens, was constructed consisting of 10,563 tetrahedral finite elements. The model was compressed in one direction and was free to deform in the other two according to the unconfined compression experimental protocol. The mechanical properties of the constitutive equations were varied so that the sum of the squared errors, $\chi^2 = \frac{1}{n}\sum_{i=1}^{n}\left[\left(P^{exp} - P^{model}\right)_i^2\right]$, reached a minimum. P^{exp}, P^{model} are the experimentally measured and predicted by the model 1st Piola-Kirchhoff stresses, respectively, and n the number of experimental data. **Fig. *2-3*** shows a typical fit of the model. The exponential constitutive equation describes the response of the tissue very well, while the neo-Hookean and Blatz-Ko models cannot capture the highly nonlinear response of the tumor. The average values and standard errors of the model parameters and the values of χ^2 are shown in Table 1.

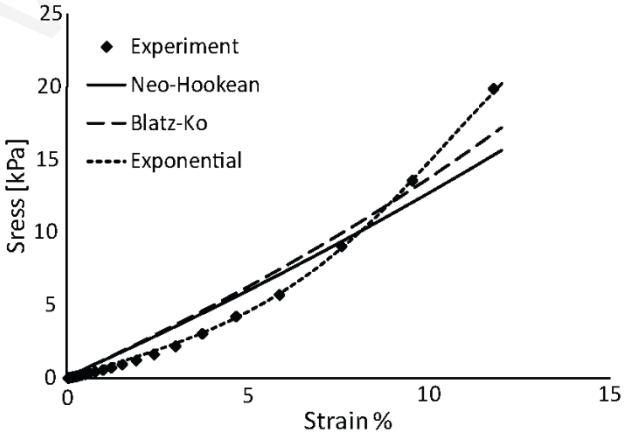

Fig. *2-3*. Representative fitting of the neo-Hookean, the Blatz-Ko and the exponential constitutive equations to the experimentally measured stress-strain response of a tumor specimen.

Table 1: Values of the mechanical properties of the two tumor types derived by fitting the model to the experimental stress-strain curves. Standard errors are shown in parenthesis.

Tumor type	neo-Hookean (Eq. (2.5))			Blatz-Ko (Eq.(2.6))			Exponential (Eq.(2.7))			
	μ (kPa)	κ (kPa)	χ^2	G_t (kPa)	q	χ^2	A_1 (Pa)	A_2 (kPa)	C_1	χ^2
MCF10CA1a	37.8 (6.5)	50.4 (8.6)	0.82 (0.13)	28.9 (6.2)	-1.52 (0.46)	0.66 (0.11)	115.2 (23.7)	31.7 (7.9)	43.3 (3.0)	0.19 (0.04)
SW620	26.7 (6.1)	35.5 (8.1)	1.41 (0.20)	22.1 (6.6)	-2.44 (1.01)	0.71 (0.14)	100.2 (25.1)	18.7 (2.1)	40.3 (5.1)	0.30 (0.04)

2.3.3 The selection of tumor's constitutive equation has a minor effect on the in vivo evolution of solid stress during progression

To model tumor growth, the tumor was represented as a sphere with an initial diameter of 500 μm surrounded by normal tissue. Tumors of this size are large enough to be treated as a continuum and at this size the stresses start to evolve [56]. The normal tissue had a cubic shape and its size was two orders of magnitude larger than that of the tumor to avoid boundary effects. The surrounding host tissue was modeled as a neo-Hookean material with a shear modulus of μ = 15 kPa and a Poisson's ratio of ν = 0.2 [6,54]. Due to symmetry, we solved for the one eighth of the domain, applying a symmetry boundary condition at the symmetric boundaries and a stress free condition at the free surfaces (**Fig. *2-4***). The finite element software accounts automatically for the continuity of the surface tractions and the displacements at the interface of the tumor with the normal tissue. The domain consisted of 49,668 tetrahedral finite elements.

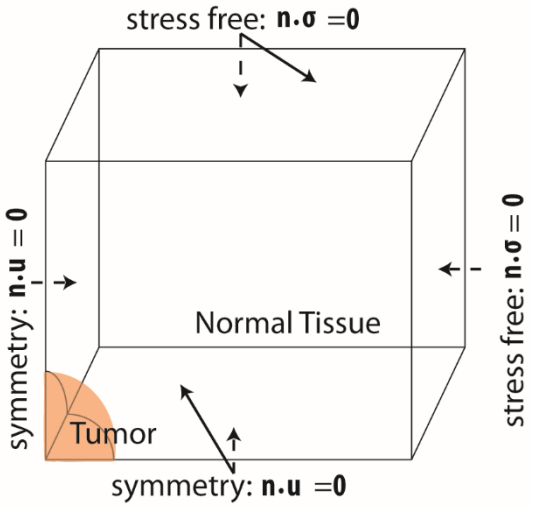

Fig. *2-4*. Boundary conditions employed. Due to symmetry the one eight of the domain was solved. **n** is the unit normal vector and **u** is the displacement vector. The continuity of the displacements and the normal stress at the tumor-host interface are implemented automatically by the software.

The assumption of isotropic tumor growth results in a uniform evolution of compressive solid stress within the tumor, while at the interface with the normal tissue the radial stress diminishes while the circumferential stress turns to tensile (**Fig. *2-5***). These predictions for the spatial distribution of the solid stress are in agreement with previous mathematical models [41,42]. To specify the parameters λ_{max}, α and β (Eqs. (2.3) and (2.4)), we fitted the model to the experimental growth data of the SW620 tumors. Interestingly, the values of these parameters were independent from the choice of the constitutive equation when the mechanical properties presented in Table 1 were used (**Fig. *2-6***). The values were λ_{max} = 50, α = 0.42 day^{-1} and β = 2.2×10^{-5} Pa^{-1} for all three constitutive equations. Moreover, the stresses developed in the tumor did not depend on the selection of the constitutive equation (**Fig. *2-6***B). Therefore, despite the fact that in the *ex vivo* situation the two constitutive equations provide largely different predictions, with the exponential expression being the only accurate (**Fig. *2-3***), in the *in vivo* situation the selection of a constitutive equation for the tumor becomes less important.

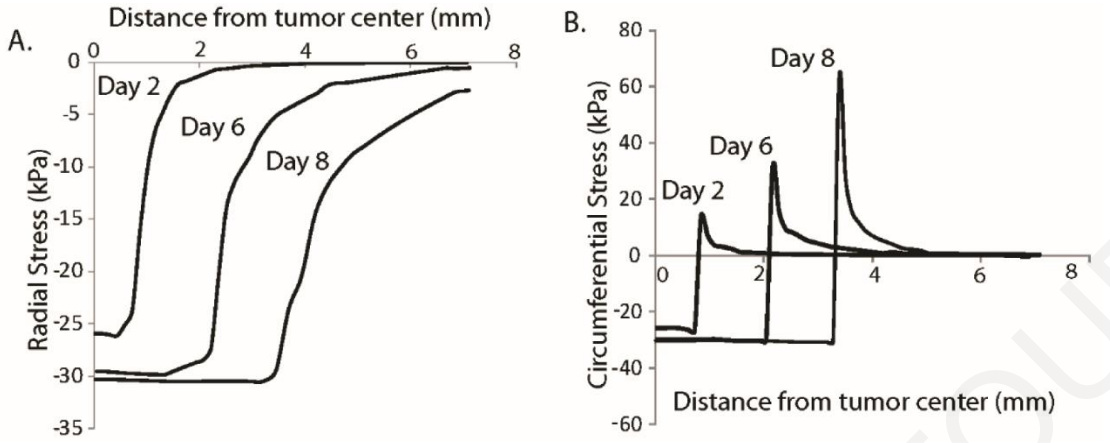

Fig. *2-5*. Spatial profile of the (A)**.** radial and (B**).** circumferential solid stress in the tumor and the surrounding normal tissue at three different time points. Solid stress is compressive and uniform in the tumor interior, while at the interface with the normal tissue radial stress diminishes and circumferential stress turns steeply to tensile.

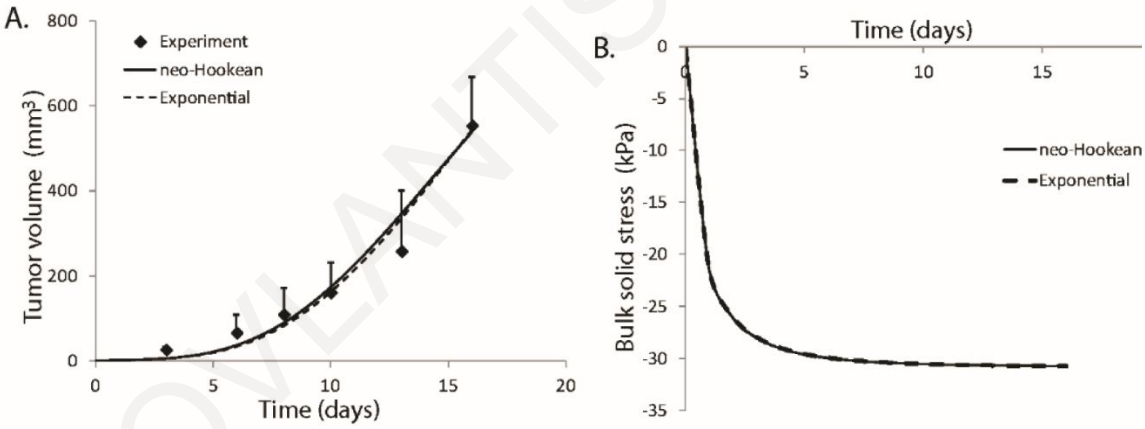

Fig. *2-6*. (A) Model fit to the experimentally measured growth curve of SW620 tumors using the neo-Hookean and the exponential equation. (B) Evolution of bulk solid stress in the tumor interior does not depend on the selection of the constitutive equation. Results using the Blatz-Ko material are omitted for clarity.

2.3.4 Mechanical interactions with the host tissue strongly affect the in vivo state of stress and growth rate of the tumor

The generation of solid stress during progression must depend on the resistance from the host tissue. Provided that the tumor is stiffer than the host tissue, as it grows it would displace the surrounding tissue, which in turn would resist to tumor expansion. Therefore, the stress in the tumor should depend on the mechanical properties of the host. In **Fig. *2-7***A, model predictions for the evolution of the bulk solid stress of the tumor are plotted for three values of the shear modulus of the host tissue, keeping the Poisson's ratio constant to 0.2. The exponential equation and the parameter values given in Table 1 for the SW620 cell line were used for the tumor. The figure shows that the stiffer the surrounding tissue is, the higher the stress in the tumor becomes, which inhibits tumor growth (**Fig. *2-7***B).

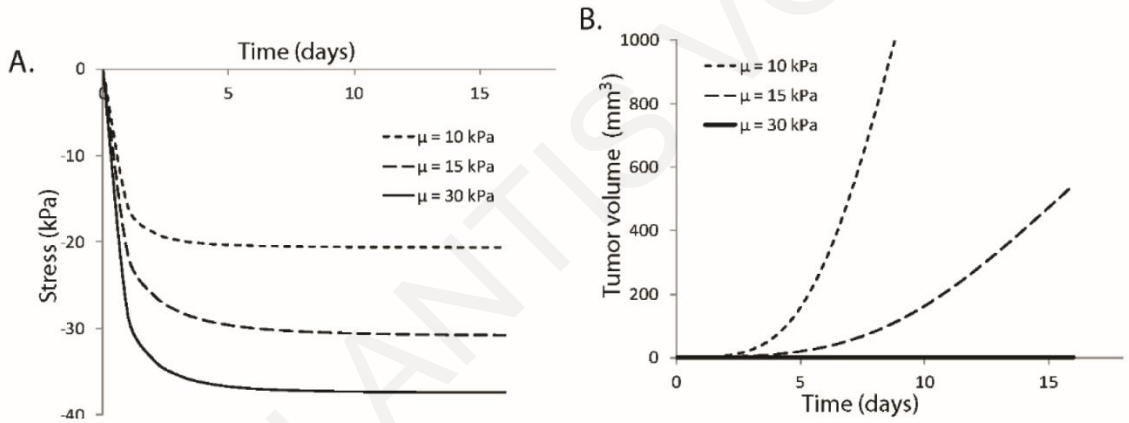

Fig. *2-7*. Dependence of (A) state of stress and (B) growth rate of tumors on the mechanical properties of the host tissue. The host tissue was modeled as a compressible neo-Hookean material with Poisson's ratio of 0.2 and three values of the shear modulus were used, μ = 10, 15 and 30 kPa. The stiffer the host tissue is, the higher the stress in the tumor and the lower its growth rate becomes.

These results of our mathematical model can explain our previously published *in vivo* data, which show that when the same cancer cell line grows in different host tissues, it exhibits different growth rates [2]. Also, our results are in agreement with *in vitro* studies of cancer cell spheroids grown within an agarose matrix. In these studies, they increased the concentration of agarose to increase the stiffness of the matrix as well as the compressive stress exerted on the cells and found that making the agarose matrix stiffer inhibits or even completely ceases the growth of the spheroids [20]. Finally, our analysis suggests that

stiffening of the tumor is essential for the tumor to grow at the expense of the host tissue. Indeed, in many cancers (e.g. various sarcomas, pancreatic, colon and breast cancers) a desmoplastic reaction takes place that results in the production of collagen and other extracellular molecules, which stiffens the tissue. One pathway through which this might occur is the activation of transforming growth factor-β (TGF-β) that regulates the production of matrix-modifying enzymes [23,57,58].

Finally, we used the mathematical model to investigate how stiff a tumor should become relative to the host tissue, so that it will be able to grow in size. *In vitro* studies using cancer cell spheroids grown in a fibrous matrix [20] have shown the existence of a critical value of the relative stiffness of the tumor compared with the host tissue above which tumors can grow, but quantification of this critical stiffness can be estimated only with mathematical modeling. **Fig. *2-8*** presents the bulk stress and the volume of the tumor as a function of the relative stiffness, μ^*. μ^* is defined as the ratio of the tumor's shear modulus over the shear modulus of the normal tissue. We modeled both tissues with the neo-Hookean equation, the value of the shear modulus given in Table 1 for the SW620 cell line was used for the tumor, while the shear modulus of the normal tissue was varied. The results correspond to day 5 of the simulations and two values of the parameter β were used, the one found by fitting the model to the experimental data of **Fig. *2-3*** and a value of zero, which renders the growth stretch ratio, λ_g, independent from the stress, and thus, the inhibitory effect of stress on tumor growth diminishes. The compressive solid stress in the tumor interior increases as the shear modulus of the host tissue increases (i.e., μ^* becomes smaller), but interestingly it reaches a plateau when the shear modulus of the host tissue is equal to or higher than the modulus of the tumor (**Fig. *2-8***A). Also, in agreement with the *in vitro* studies, **Fig. *2-8***B suggests that the stiffness of the tumor should exceed a critical value compared with the stiffness of the host tissue, so that the tumor will be able to physically displace the tissue and grow in size. The model further predicts that this critical value of relative stiffness should be on the order of 1.5. It is noted, however, that apart from mechanical factors, biological factors that are not accounted for in our analysis, such as the expression of matrix-modifying agents (e.g., matrix metalloproteinases) or the supply of oxygen and nutrients also affect the progression of the tumor.

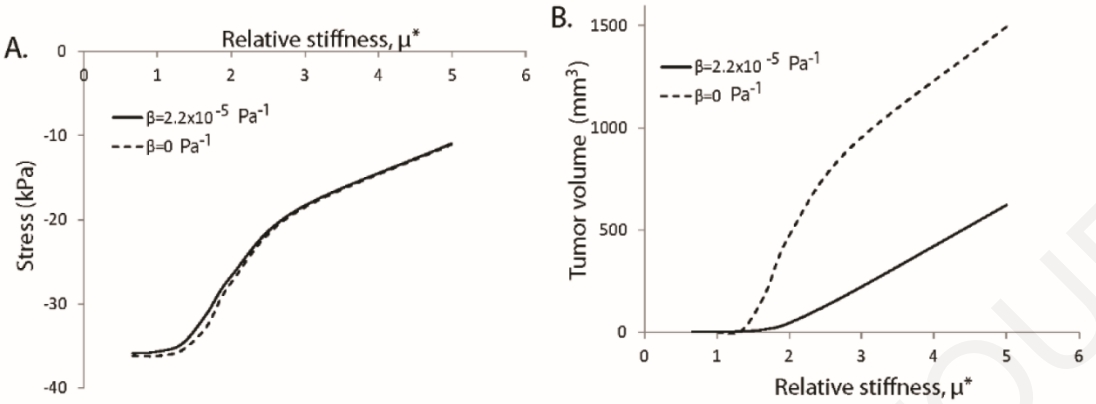

Fig. *2-8*. Dependence of (A) the state of stress and (B) tumor volume on the relative stiffness of the tumor compared to the normal tissue, μ^*. Relative stiffness is the ratio of the tumor shear modulus to that of the host. Results correspond to day 5 of the simulations. Tumor solid stress increases with stiffening of the surrounding host tissue and reaches a plateau when the stiffness of the tumor becomes the same as or lower than the stiffness of the host (panel A). The tumor has to reach a critical stiffness compared with that of the normal tissue to be able to displace the tissue and grow (panel B).

2.4 **Discussion**

Mechanical forces shape the tumor microenvironment and largely determine tumor progression and therapeutic outcome [59]. Despite the important role of the mechanical behavior of solid tumors, to date there is no experimental method to quantify solid stress levels *in vivo*. Only recently, we invented an *ex vivo* technique to quantify the growth-induced, residual component of the solid stress [2]. Therefore, the estimation of solid stress levels during progression requires the use of mathematical modeling. The accuracy of current mathematical models, however, is limited because of a lack of experimental studies to characterize the mechanical response of tumors.

This study had two major objectives. The first objective was to perform unconfined compression experiments in two tumor types in order to measure the visco-elastic response of the tumors, derive their elastic modulus and tan(δ) in compression and determine a suitable constitutive equation that reproduces the experimentally measured *ex vivo* elastic response. The second objective was the use of a biomechanical model of tumor growth to

determine to what extent the selection of a constitutive equation affects solid stress levels in a growing tumor and what is the contribution of the mechanical interactions with the host tissue to the state of stress and growth of the tumor. We found that solid tumors exhibit a highly nonlinear elastic response in compression, even at very low strains (**Fig. *2*-*2***), similar to most soft biological tissues including arteries, tendons and ligaments [54]. The elastic modulus was measured to be 288.3 ± 45.5 kPa for the MCF10CA1a and 186.1 ± 25.9 kPa for the SW620 tumors. These values are comparable to the elastic moduli of other soft biological tissues, such as the arterial wall [60], and at least an order of magnitude higher than previous measurements in tumors [44,45]. The discrepancy with the previous studies is due to the fact that in those measurements a small piece of the tumor (< 5 mm) was used as a specimen, while in our study we tested almost the entire tumor. Therefore, our results correspond to the macroscopic, tissue-level, response of the tissue.

We also found that due to the highly nonlinear *ex vivo* elastic response of solid tumors, the commonly used neo-Hookean and Blatz-Ko constitutive equations fail to capture the mechanical behavior of the tumor. An exponential equation more accurately reproduces the experimental response and it should be preferred in mathematical models along with the corresponding mechanical properties, given in Table 1. In the *in vivo* situation, however, the evolution of solid stress in the tumor depends strongly on the properties of the host tissue and the selection of the constitutive equation becomes less important. The fact that variations in the choices of properties and constitutive models all led to the same conclusion is a finding that suggests a fundamental phenomenon and not an artifact of arbitrary modeling choices. It should be noticed, however, that in the current study we used constitutive equations of compressible materials. In previous research [6] we showed that treating tumors as incompressible can lead to higher stresses than the compressive case. Whether solid tumors are compressible or incompressible still remains an open question. Taken together, we conclude that apart from the mechanical behavior of the tumor, one should measure and incorporate into mathematical models the properties and mechanical response of the host tissue as well. Given the direct correlation between mechanical compression and inhibition of cancer cell proliferation [24], the mechanical behavior of the host tissue plays also an important role in the growth rate of the tumor. We highlighted here that the host tissue inhibits tumor growth not only by suppressing cancer cell proliferation but also by resisting to the expansion of the tumor.

The biomechanical model presented in this study is limited in that it does not account for the effect of solid stress on the compression of blood vessels, which reduces perfusion and the supply of oxygen and nutrients. Vascular compression is an indirect way that inhibits tumor growth, independently from the direct effect of solid stress [20,24,29]. Incorporation of vessel compression by solid stress would further inhibit the growth rate of the tumor. Also, we did not consider in our analysis the growth-induced, residual component of solid stress. Growth-induced stress contributes less than 30% to the total solid stress of the tumor, which suggests that the external stress by the host tissue is the dominant component of solid stress[6]. Another parameter not considered in our study was the contribution of the interstitial fluid to the total stress and the pathology of cancer [31]. Interstitial fluid pressure is additive to the bulk solid stress to yield the total stress of the tissue. Typical interstitial fluid pressure values in murine tumors are in the range of 1.0-4.0 kPa (10-30 mmHg) [61], much lower than solid stress, and because it is uniformly distributed in the tumor interior has no effect on solid stress levels [6]. Finally, as many other biological tissues, solid tumors are highly heterogeneous structures, consisting of multiple structural components, such as cancer and stromal cells, collagen and hyaluronan [62,63]. Each of these constituents has a different contribution to the mechanics of a tumor [2] and their concentration and organization in the tissue can vary considerably in the same tumor during progression, between the primary tumor and its metastases and among tumors of different types. Therefore, further studies are required to relate the structure to the mechanical function of tumors. Structure-based models [64,65] should be better suited to investigate this correlation compared to continuum-level constitutive equations, like these employed in our study.

3 Chapter 3: Tranilast-induced stress alleviation in solid tumors improves the efficacy of chemo- and nanotherapeutics in a size-independent manner.

This research has been published in Scientific Reports: Papageorgis P., C. Polydorou, F. Mpekris, C. Voutouri, E. Agathokleous, C. P. Kapnissi-Christodoulou, and T. Stylianopoulos. Tranilast-induced stress alleviation in solid tumors improves the efficacy of chemo- and nanotherapeutics in a size-independent manner. *Scientific Reports* 7:46140. [DOI: 10.1038/srep46140].

3.1 **Introduction**

Accumulation of mechanical stresses during cancer progression can induce blood and lymphatic vessel compression, creating hypo-perfusion, hypoxia and interstitial hypertension which decrease the efficacy of chemo- and nanotherapies. Stress alleviation treatment has been recently proposed to reduce mechanical stresses in order to decompress tumor vessels and improve perfusion and chemotherapy. However, it remains unclear if it improves the efficacy of nanomedicines, which present numerous advantages over traditional chemotherapeutic drugs. Furthermore, we need to identify safe and well-tolerated pharmaceutical agents that reduce stress levels and may be added to cancer patients' treatment regimen. In this Chapter, we show mathematically and with a series of *in vivo* experiments that stress alleviation improves the delivery of drugs in a size-independent manner. Importantly, we propose the repurposing of tranilast, a clinically approved anti-fibrotic drug as stress-alleviating agent. Using two orthotopic mammary tumor models, we demonstrate that tranilast reduces mechanical stresses, decreases interstitial fluid pressure (IFP), improves tumor perfusion and significantly enhances the efficacy of different-sized drugs, doxorubicin, Abraxane and Doxil, by suppressing TGFβ signalling and expression of extracellular matrix components. Our findings strongly suggest that repurposing tranilast could be directly used as a promising strategy to enhance, not only chemotherapy, but also the efficacy of cancer nanomedicine.

The rationale for the use of macromolecules and nanomedicines to treat cancer is based on the hyper-permeability of some tumor blood vessels that allows large therapeutic agents to selectively accumulate into the tumor tissue, and the dysfunction of intratumoral lymphatic

vessels that retain the drugs into the tumor for a longer time [66,67]. This phenomenon, known as the Enhanced Permeability and Retention (EPR) effect, forms the basis for the passive delivery of drugs to solid tumors [14,68]. Passive delivery of drugs to solid tumors utilizing the EPR effect is size-dependent and drugs larger than 50 nm in diameter might exhibit poor accumulation and penetration into the tumor [69-71].

In previous research, it has been shown that normalization of tumor blood vessels with judicial use of anti-angiogenic agents improves the delivery and thus, the efficacy of macromolecules and small nanomedicines, up to 12 nm in size [72-74]. Recently, it was found that this strategy might improve the efficacy of particles as large as 40nm [75]. Inability of anti-angiogenic therapies to improve drug efficacy in a size-independent manner is owing to the fact that vascular normalization repairs the abnormally large pores in the tumor blood vessel wall making them less permeable. Decreasing vessel wall pore size reduces IFP but at the same time prevents large nanoparticles from crossing the tumor vessel wall into the tumor interior. Furthermore, vascular normalization treatment cannot treat compressed tumor blood vessels, which are the result of the accumulation of mechanical stresses in the tumor owing to the growth of it in the confined space of the host tissue [6,26,27]. Blood vessel compression is another factor that drastically affects tumor perfusion as it reduces the capacity of a vessel to carry blood. This explains why anti-angiogenic agents have failed in desmoplastic tumors, such as pancreatic and breast cancers, which exhibit high stress levels leading to abundant compressed vessels [76,77]. The extracellular matrix (ECM) components, namely collagen and hyaluronan are a major contributor to the accumulation of mechanical stress in tumors, as has been already mentioned. Even though it has been shown that depletion of collagen and hyaluronan using angiotensin inhibitors can improve the efficacy of chemotherapeutics by alleviation of mechanical stresses and decompression of tumor blood vessels [32], this principle is still not well defined and there is yet no or experimental evidence to demonstrate the effect of this approach using drugs of different sizes. Finally, angiotensin inhibitors are commonly used as anti-hypertensive drugs and thus, might affect the blood pressure of patients. Therefore, we urgently need to identify other safe and well tolerated pharmaceutical agents that reduce stress levels and may be added to cancer patients' treatment regimen.

In this Chapter study in experimentally the alleviate mechanical stress with anti-fibrotic agent, where reduces ECM components.To this end, using mathematical modeling and in

vivo experiments we show that stress alleviation improves the delivery of drugs in a size-independent manner. Furthermore, we hypothesize that Tranilast, a clinically approved and inexpensive anti-fibrotic drug with decades of safe use can be repurposed to alleviate mechanical stress in solid tumors and that Tranilast-induced stress alleviation can improve the delivery and efficacy of common anticancer drugs of all sizes. In this work, to experimentally test our hypotheses, we employed two breast cancer cell lines (MCF10CA1a and 4T1) and three drugs of different sizes, namely doxorubicin (<1nm), Abraxane (10nm) and Doxil (100nm) and showed that Tranilast can improve the efficacy of all drugs by alleviating tumors' solid and fluid stresses.

3.2 **Methods**

3.2.1 Animal tumor models and treatment protocols

Orthotopic xenograft breast tumors were generated by implantation of 5×10^5 MCF10CA1a cells in 40 μl of serum-free medium into the mammary fat pad of 6-week old female CD1 nude immunodeficient mice. Orthotopic syngeneic models for murine mammary tumors were generated by implantation of 10^5 4T1 mouse mammary cancer cells in 40 μl of serum-free medium into the mammary fat pad of 6-week old BALB/c female mice. In both animal tumor models, tranilast (200mg/kg) was administered orally once a day from day 4 post-implantation. During the course of each experiment, tumor growth was monitored daily and the planar dimensions (x, y) were measured using a digital caliper. Tumor volume was calculated using the volume of an ellipsoid and assuming that the third dimension, z, is equal to $\sqrt{xy}$. All in vivo experiments were conducted in accordance with the animal welfare regulations and guidelines of the Republic of Cyprus and the European Union (European Directive 2010/63/EE and Cyprus Legislation for the protection and welfare of animals, Laws 1994-2013) under a license acquired and approved (No CY/EXP/PR.L1/2014) by the Cyprus Veterinary Services committee, the Cyprus national authority for monitoring animal research for all academic institutions.

3.2.2 Experimental procedure

To measure alterations in the tumor microenvironment, right before the end of the experiment, animals were anesthetized by i.p. injection of Avertin (200mg/kg) and interstitial fluid pressure was measure using the wick-in-needle technique [2,61,78]. Next,

mice were injected intracardially with 100μl biotinylated lectin (1mg/ml, Vector Labs) which was allowed to distribute throughout the body for 7 minutes [79]. Finally, mice were sacrificed via CO_2 inhalation and tumors were excised for measurement of mechanical properties and/or histological analysis.

3.2.3 Fluorescent immunohistochemistry and vessel perfusion histology

MCF10CA1a and 4T1 breast tumors were excised from mice, fixed and embedded in optimal cutting temperature compound (OCT). Transverse 40μm-thick tumor sections were produced using the Tissue-Tek Cryo3 (SAKURA) and immunostained with antibodies against collagen I, CD31 and hyaluronan. For Ki67 staining, tumors were fixed in paraformaldehyde and embedded in paraffin before sectioning[37].

For blood vessel perfusion analysis, mice were slowly injected with 100 μl of 1 mg/ml biotinylated lycopersicon esculentum lectin (Vector Labs) via intracardiac injection 7 minutes prior to euthanization and tumor removal. Upon excision, tumors were fixed in paraformaldehyde, embedded in OCT and frozen. Transverse 60 μm-thick tumor sections were produced and stained with an antibody CD31, streptavidin-conjugated and fluorescently-labeled secondary antibodies.

In addition, MCF10A1a tumors were immunostained with an anti-phosphorylated-Smad2 (Ser465/467)/Smad3 (Ser423/425) antibody and counterstained with anti-β-tubulin. Images from anti-collagen I, anti-CD31, anti-hyaluronan and anti-biotin-stained sections were analysed based on the area fraction of positive staining. Images from collagen I, hyaluronan and CD31 stained sections were analysed based on the area fraction of positive staining using an in-house code in MATLAB (MathWorks, Inc., Natick, MA, USA) [2]. Vessel diameter was calculated from the CD31 images. Specifically, the procedure of the identification of the non-collapsed vessels was automated in the MATLAB code. The CD31 staining that forms a loop was considered to be a vessel and the short axis of a cross-section fit to an oval was taken. Five different sections per tumor (from the interior and the periphery) at ×10 magnification were taken and analysed keeping the analysis settings and thresholds the same for all tumors. Mechanical testing measurements for calculation of elastic modulus and hydraulic conductivity

3.2.4 Unconfined compression experiments for calculation of elastic modulus and hydraulic conductivity

Stress-strain experiments - calculation of elastic modulus

Unconfined compression, stress-strain and stress-relaxation experiments were carried out using a commercial high precision mechanical testing system (Instron 5944, Norwood, MA, USA). The specimens were cut in an orthogonal shape with approximate dimensions 3×3×2 mm (length × width × thickness). According to the stress-strain protocol the specimens were placed between two parallel platens and they were compressed to a final strain of 30% with a strain rate of 0.05mm/min, the minimum rate the system can apply in order to avoid any transient, poroelastic effects. Stress was calculated as the force measured on the load cell divided by the initial surface area of the specimen (i.e., 1st Piola-Kirchhoff stress), and displacement data were converted to strain as $\varepsilon = \Delta l / l_0$, where Δl the change in the length of the specimen in the direction of compression and l_0 the initial, undeformed length. The elastic modulus was calculated from the slope of the stress-strain curve at 30% strain.

Stress-relaxation experiments - Calculation of hydraulic conductivity

For the stress relaxation experiments, specimens underwent four cycles of testing for each of which a 5% compressive strain was applied for 1 minute, followed by a 10 minute hold. Subsequently a common biphasic model of soft tissue mechanics was employed [80] accounting for both the solid components (cells and extracellular matrix) and the fluid phase (interstitial fluid) of the tumor. The solid phase stress, $\boldsymbol{\sigma}^s$, was modeled as a neo-Hookean material and the values of the elastic modulus used in the neo-Hookean model were obtained by the stress-strain experiments, assuming the Poison's ratio to be v=0.45. The fluid phase was assumed to be inviscid (i.e., ideal fluid) with the fluid stress was given by $\boldsymbol{\sigma}^f = -p\mathbf{I}$, where p the interstitial fluid pressure. The interstitial fluid velocity was described by Darcy's law, according to which the velocity is proportional to the interstitial fluid pressure gradient with a proportionality constant the hydraulic conductivity of the interstitial space, i.e., $v = -K_t \nabla p$. The governing equations are: the momentum balance: $\nabla \cdot (\boldsymbol{\sigma}^s - p\mathbf{I}) = 0$ and the mass conservation $\nabla \cdot v^s - K_t \nabla^2 p = 0$. The model was implemented in the finite elements commercial software COMSOL Multiphysics version 4.4 (COMSOL, Inc., Burlington, MA). The unconfined compression, stress relaxation experiment was simulated in the mathematical model and model predictions were fitted to

the experimental data by varying the hydraulic conductivity of the tumor interstitial space **Fig. *3-1***. From the fitting the value of the hydraulic conductivity was determined.

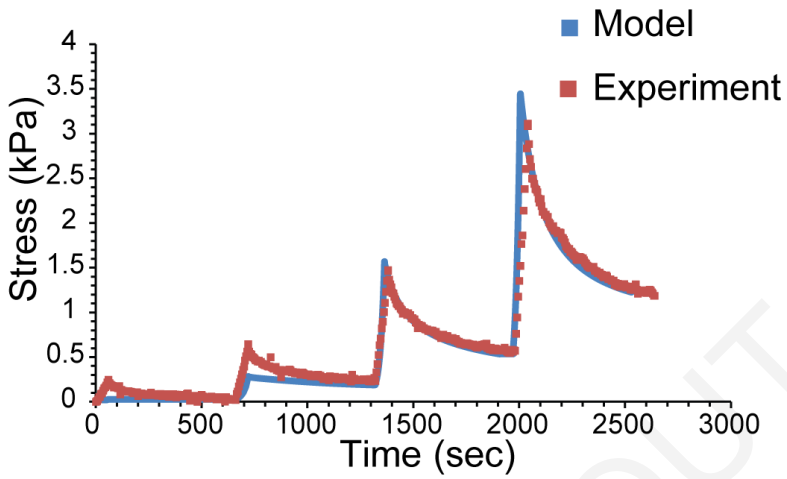

Fig. *3-1*. Typical stress relaxation data of the tumors tested along with the fit of the biphasic model. The only fitting parameter was the hydraulic conductivity of the interstitial space.

3.3 **Results**

3.3.1 Tranilast improves the efficacy of common anticancer drugs in a size-independent manner

Based on these predictions, we hypothesized that Tranilast can improve the efficacy of therapeutics via stress alleviation. To investigate our hypothesis, we developed two orthotopic mouse models for breast cancer; a xenograft model using the human MCF10CA1a cancer cell line and a syngeneic model using the mouse 4T1 cancer cell line and employed three commonly used drugs: doxorubicin, which has a size of less than 1nm; Abraxane, a 130 nm albumin-bound paclitaxel that shrinks to 10nm following dilution to plasma[74]; and Doxil, a ~100 nm pegylated liposomal doxorubicin. Mice received orally mock treatment or Tranilast (200 mg/kg) 4 days post-implantation of cancer cells in the mammary fat pad, whereas anti-tumor drug administration begun on day 11. Higher doses of Tranilast have been previously associated with direct anti-tumor and anti-vascular effects, whereas lower doses did not cause any effect on ECM composition [81-83]. We found that Tranilast alone did not influence primary tumor growth (**Fig. *3-2***). Similarly, doxorubicin

(2 mg/kg to 5 mg/kg, i.p.) had no effect on tumor growth in either animal model. However, combinatorial treatment with Tranilast and doxorubicin significantly delayed tumor growth (**Fig. *3-2***A&B). Next, we investigated the role of Tranilast in the efficacy of nanotherapeutics. Our data indicate that Tranilast dramatically improved the efficacy of i.v. administered Abraxane (20 mg/kg) as depicted by the substantial differences in breast tumor growth rates (**Fig. *3-2***C). Similarly, while initial i.v. administration of 6 mg/kg Doxil had a similar effect in control and Tranilast-treated mice, lowering the dose (3 mg/kg) resulted in a differential response between the two groups (**Fig. *3-2***C). In agreement with model predictions, our data confirm that Tranilast-induced stress alleviation improves the efficacy of drugs in a size-independent manner.

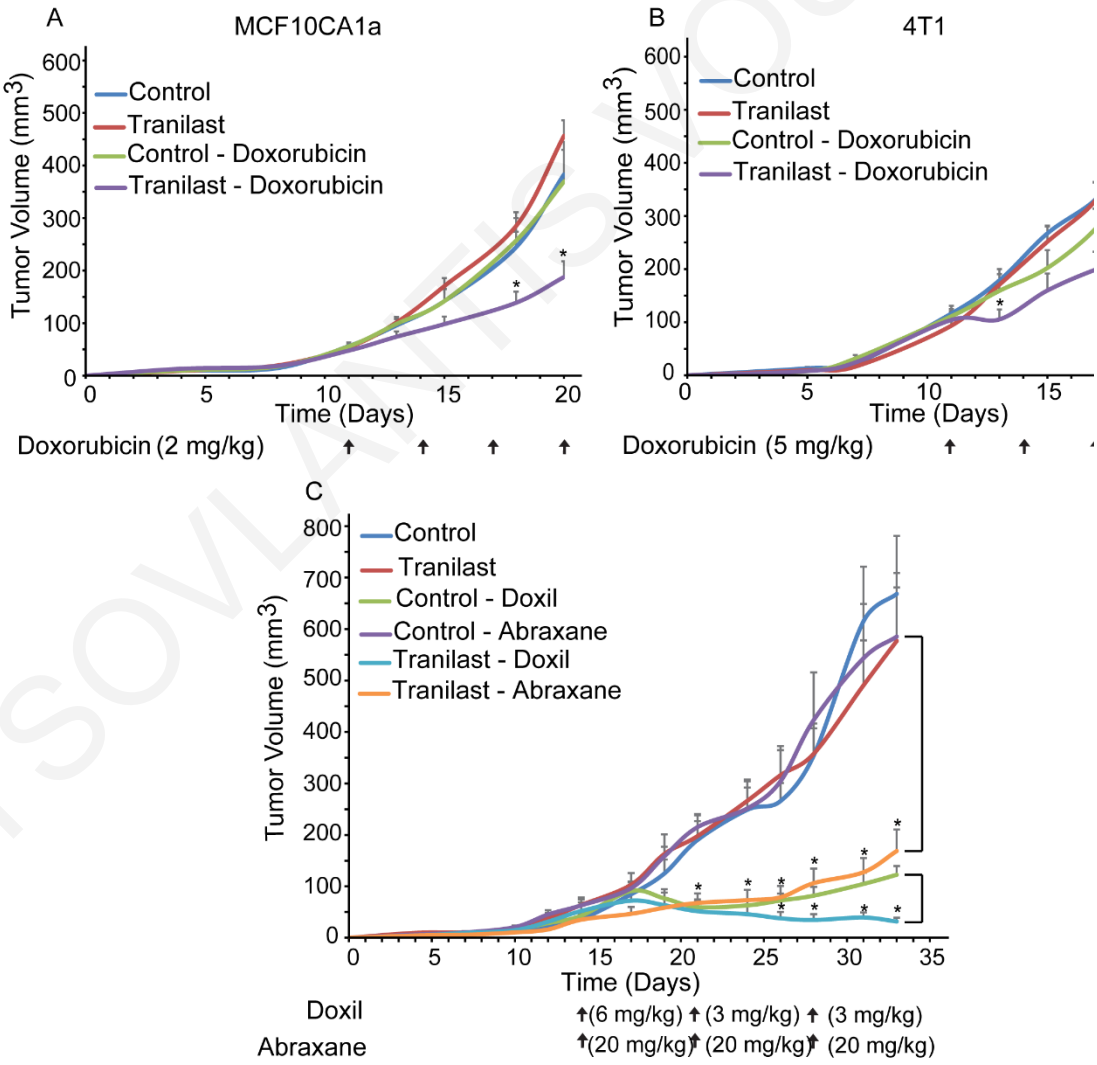

Fig. *3-2*. Tranilast increases anti-tumor efficacy of chemo- and nanotherapy. Tumor volume growth rates of orthotopic MCF10CA1a human breast tumors (A) and 4T1 murine breast tumors (B) implanted in female CD1 nude or BALB/c mice, respectively. Control treatment (NaHCO3 and saline), Tranilast or doxorubicin alone had no effect on tumor growth in both tumor models. Combination of Tranilast (200 mg/kg) and doxorubicin (2 mg/Kg) significantly delayed tumor growth of MCF10CA1a breast tumors compared to doxorubicin monotherapy ($p = 0.01$ on day 20, n = 6-8). Similarly, while doxorubicin alone (5 mg/kg) had no effect on growth of 4T1 murine breast tumors, combination of Tranilast and doxorubicin significantly reduced tumor growth rate ($p = 0.015$ on day 20, n = 6-8). C. Tumor volume growth rates of orthotopic MCF10CA1a breast tumors implanted in CD1 nude mice that were either control-treated (0.9% NaCl for Abraxane, saline for Doxil and NaHCO3 for Tranilast), Tranilast-treated alone (200 mg/kg daily via gavage), Doxil alone (6 mg/kg on day 14 and 3 mg/kg on days 21 and 28 post-implantation, i.v.), Abraxane alone (20 mg/kg on days 14, 21 and 28 post-implantation, i.v.), or Tranilast in combination with either Doxil or Abraxane, as described above. Abraxane alone had no effect on tumor volume, compared to administration of Tranilast with Abraxane, which significantly delayed tumor growth ($p = 0.003$ on day 33, n = 7-9). Doxil monotherapy at 6 mg/kg decreased tumor volume whereas at 3 mg/kg had no effect. In contrast, combination of Doxil 3 mg/kg and Tranilast significantly reduced tumor volume ($p = 0.0001$ on day 33, n = 7-9) compared to Doxil alone. Asterisks indicate a statistically significant difference between compared groups ($p < 0.05$).

3.3.2 Tranilast remodels the tumor microenvironment reducing collagen and hyaluronan levels

To investigate the ability of Tranilast to remodel the tumor ECM, we initially performed histological analysis of tumor cryosections. Tranilast treatment decreased the amount of both collagen and hyaluronan, as represented by area fraction quantification (**Fig. *3-3***). Specifically, area fractions of collagen (**Fig. *3-3***C) were reduced by 20% and 25% and of the hyaluronan (**Fig. *3-3***D) by 40% and 63% in the 4T1 and MCF10CA1a Tralinast-treated tumors, respectively compared to control tumors ($p = 0.025$, 4T1; $p = 0.024$, MCF10CA1a for collagen and $p = 0.043$, 4T1; $p = 0.016$, MCF10CA1a for hyaluronan).

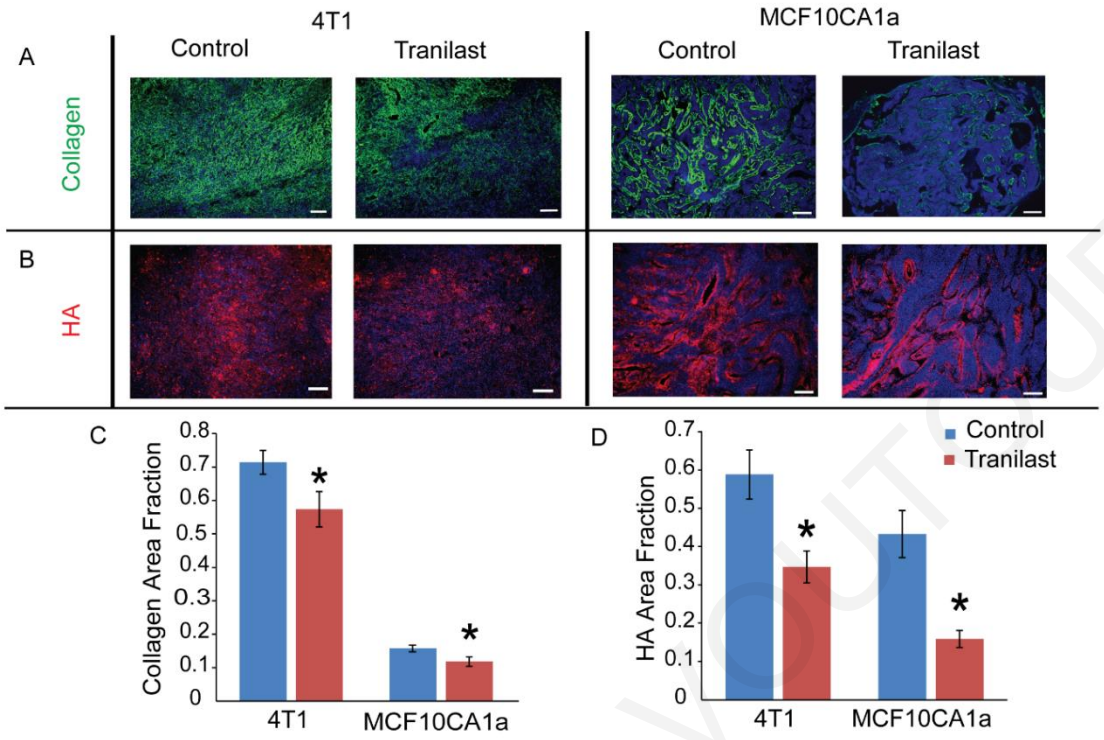

Fig. *3-3.* Tranilast decreases levels of extracellular matrix components. Representative images from histological analysis showing the effect of Tranilast on reducing (A) collagen (green) and (B) hyaluronan (HA, red) levels in 4T1 and MCF10CA1a breast tumors. Area fractions of collagen (C) and hyaluronan (HA) (D) were significantly lower in Tranilast-treated compared to control-treated tumors ($p = 0.025$, 4T1; $p = 0.024$, MCF10CA1a for collagen, $p = 0.043$, 4T1; $p = 0.016$, MCF10CA1a for hyaluronan, $n = 6$ from each group). Asterisks indicate statistically significant difference between groups. Scale bar: 100 μm.

Tranilast alleviates intratumoral solid and fluid stresses

Subsequently, to further explore the potential of Tranilast as a stress-alleviating agent, we performed detailed analysis of the mechanical properties of the tumors. We first measured the growth-induced stresses by employing our previously developed technique, the tumor opening experiment [2]. Upon excision, we cut the tumors along their longest axis at approximately 80% of their thickness. We then allowed tumors to relax and measured the formed distance between the two hemispheres (**Fig. *3-4***A). Control tumors had significantly larger tumor openings, which corresponds to higher growth-induced solid stress compared to Tranilast-treated tumors (**Fig. *3-4***B). We also performed ex-vivo stress-strain experiments, which revealed that Tranilast decreased the elastic modulus of the tumors,

making them less stiff (**Fig. *3-4***C&D). Collectively, our data from the tumor opening and stress-strain experiments clearly suggest that Tranilast decreases solid stresses (i.e., stresses of the solid phase) in both MCF10CA1a and 4T1 tumor models. In addition, we examined the effect of Tranilast on tumor fluid phase features and particularly on the interstitial hydraulic conductivity and fluid pressure. To calculate the hydraulic conductivity, we performed ex vivo stress-relaxation experiments and the data were fitted to a biomechanical mathematical model (**Fig. *2-2***). Treatment with Tranilast increased hydraulic conductivity (**Fig. *3-4***). Consistent to our predictions, using the wick-in-needle technique[78], we found that Tranilast significantly decreased IFP in both tumor models (**Fig. *3-4***F).

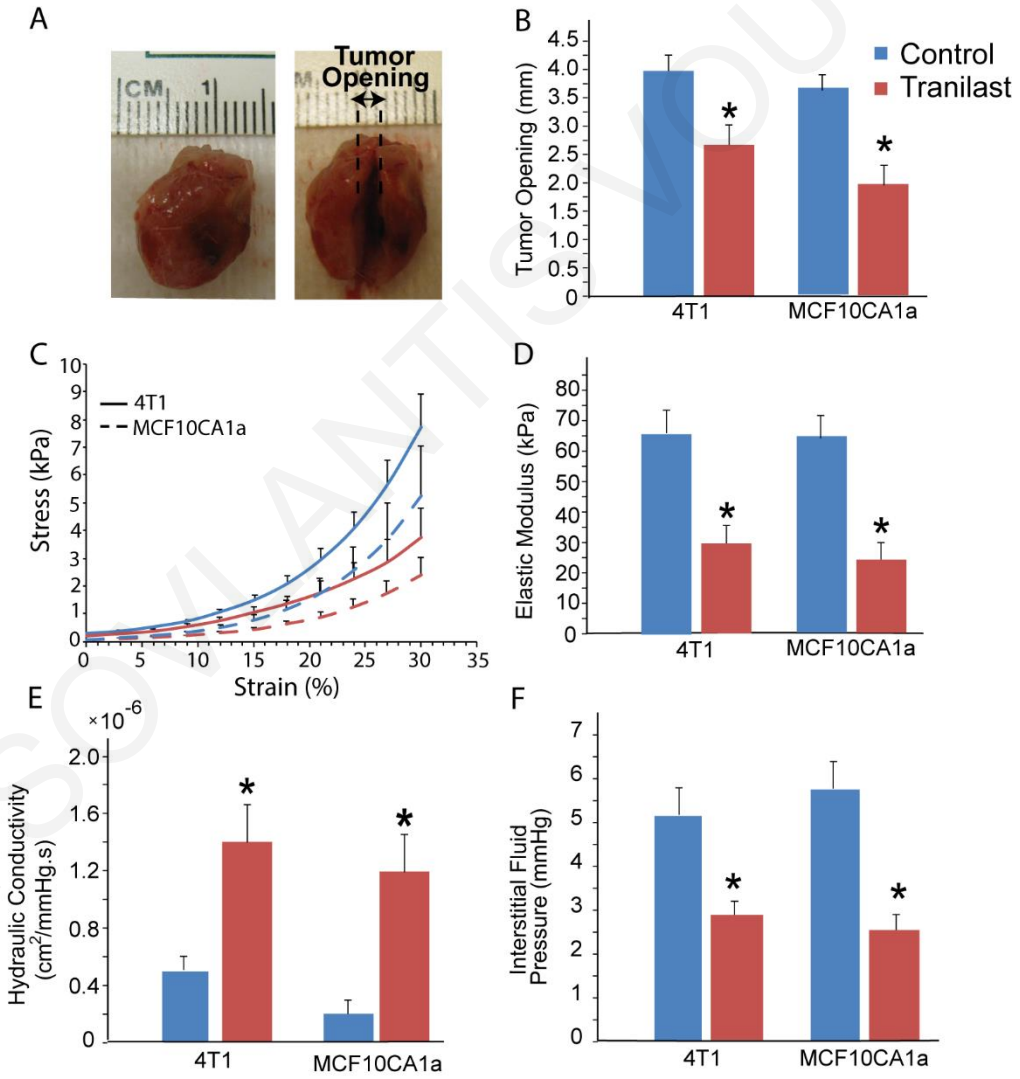

Fig. *3-4*. Tranilast alleviates solid and fluid stresses. (A) Tumor opening experiment was performed as a measure of growth-induce solid stress. After excision a cut was made ~80%

of the thickness of the tumor along the main axis and the tumor opens up as a result of stress release by tissue relaxation. (B). Measurements of tumor opening for the two different cancer cell lines indicate that treatment with Tranilast leads to lower values of relaxation compared to control treatment ($p = 0.013$ for 4T1, $p = 0.005$ for MCF10CA1a), resulting to lower levels of growth-induced stress. (C) Stress-strain curves (means and standard errors) of the two cancer cell lines for the control (blue) and Tranilast-treated (red) groups. (D) The elastic modulus of the two cancer cell lines measured from the slope of the stress-strain curves at 30% strain. The values of the elastic modulus for the Tranilast-treated tumors are significantly lower ($p = 0.002$ for 4T1, $p = 0.041$ for MCF10CA1a). Tranilast-induced reduction in ECM content resulted to lower values of the (E) hydraulic conductivity of the tumor interstitial space ($p = 0.015$ for 4T1, $p = 0.029$ for MCF10CA1a), which in turn caused alleviation of the (F) interstitial fluid pressure ($p = 0.013$ for 4T1 and $p = 0.012$ for MCF10CA1a).

3.3.3 Alleviation of stresses decompresses tumor blood vessels and improves perfusion

To investigate the effect of stress alleviation on the functionality of tumor blood vessels, we calculated the vessel diameter and the percentage of perfused blood vessels after mock or Tranilast treatment, respectively. Tissue cryosections were stained with antibodies against CD31 and biotinylated lectin. Based on the ratio of the number of biotinylated lectin positive (+) to the CD31 positive (+) vessels, the fraction of perfused vessels was calculated. Tranilast-induced stress alleviation resulted in a statistically significant increase in vessel diameter for both tumor models, which in turn caused a significant increase in tumor perfusion (**Fig. *3-5***A-D). Interestingly, despite the small increase in vessel diameter by 10-15%, the fraction of perfused vessels increased significantly by 50-60%. This is in full agreement with our previous studies [2,32] and can be explained by the fact that blood flow rate is proportional to the fourth power of the vessel diameter [$Q=(-\pi d^4)/(128\mu)\nabla P_v$] so that small increases in diameter can improve significantly blood flow. Furthermore, it is also possible a compressed upstream vessel to exclude from blood flow a large number of downstream vessels, which will become functional when the upstream vessel is decompressed. In contrast, the total area of vessels (CD31+ area) remained unaffected (**Fig.**

3-5E), suggesting that Tranilast treatment improved perfusion without affecting tumor angiogenesis.

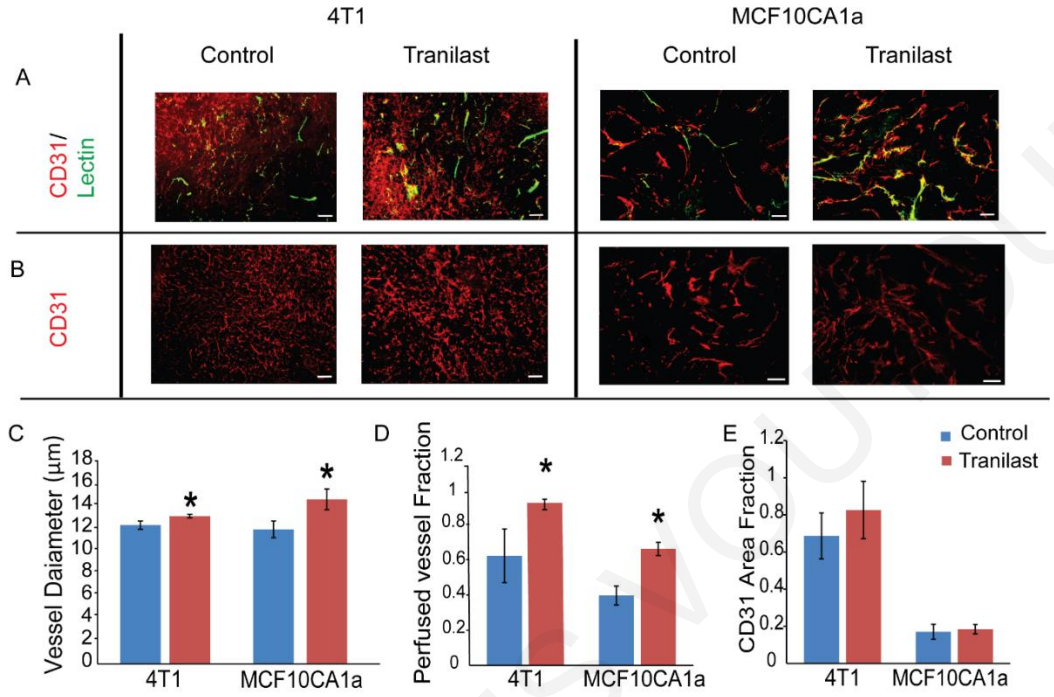

Fig. *3-5.* Tranilast-induced stress alleviation decompresses tumor blood vessel improving perfusion and doxorubicin delivery in tumors. Representative images from histological analysis A. Endothelial cell-specific marker CD31 (red), biotinylated tomato lectin (green) and co-expression (yellow) indicating the presence of perfused vessels, and B. Expression of CD31 (red) indicating blood vessels in 4T1 and MCF10CA1a tumors. Quantification of blood vessel diameter (C), fraction of perfused vessels (D), and CD31 (E) area fractions in control and Tranilast-treated tumors. Vessel diameter was significantly increased in both tumor models ($p = 0.038$, 4T1 and $p = 0.04$, MCF10CA1a, $n = 6$-8), resulting in a significant increase in the perfused vessel fraction ($p = 0.027$, 4T1 and $p < 0.001$, MCF10CA1a, $n = 6$-8), whereas CD31 area fraction was unaffected by Tranilast in both tumor models. Asterisks indicate a statistically significant difference between compared groups. Scale bar: 100 µm. Data represent the average + S.E. values and (*) indicates statistically significant differences between compared groups ($n=7$, $p < 0.05$). Tranilast improved the delivery of doxorubicin in tumors by 2.5 times ($p=0.005$).

3.4 Discussion

To conclude, the objective of our study was two-fold. The first objective was to show the potential of stress alleviation treatment to improve the efficacy of chemo- and nano-therapeutics. Stress alleviation is a recently developed therapeutic strategy, which has shown promising results in improving chemotherapy in preclinical tumor models [32,34,79] but there was no mathematical/theoretical basis for the effects of this strategy and also there was no study to explore its potential use for nanomedicines, where compromised drug delivery is a major barrier to their efficacy. Here, we demonstrated both mathematically as well as experimentally that stress alleviation improves the efficacy of common chemotherapeutics and nanomedicines in a size-independent manner. The second objective was to introduce a safe, well-tolerated drug as a stress-alleviating agent. Tranilast is an inexpensive, clinically approved drug that has already been tested in humans for toxicity and tolerance, rendering the results of our study highly transferable to the clinic. Therefore, Tranilast-induced stress alleviation combined with common anticancer drugs could directly lead to Phase II clinical trials to test the efficacy of this therapeutic strategy in humans.

Stress alleviation strategy is expected to be beneficial for tumors that have abundant compressed vessels. Vessel compression in turn is caused by mechanical stresses exerted by the cells and the extracellular matrix. Therefore, desmoplastic tumors (e.g. pancreatic and breast cancers as well as sarcomas), which contain high levels of stromal cells and ECM components should have a large amount of compressed vessels. In principle, judicious depletion of either stromal cells or ECM components or both will have the ability to alleviate stresses in order to decompress blood vessels and improve perfusion in these tumors[2]. Furthermore, as shown here, stress alleviation strategy is beneficial even for tumors with hyper-permeable vessels (e.g. a subset of breast cancers) where perfusion depends not only on vessel diameter but also on vessel permeability. In the case of tumors with compressed and hyper-permeable vessels, stress alleviation strategy could be combined with vascular normalization so that blood vessels will become decompressed and less permeable, which should optimize perfusion and delivery of small-sized drugs [6]. The degree of vessel compression and permeability, however, can vary considerably not only among tumor types but also within the same tumor type as well as between the primary tumor and its metastases. Therefore, it is difficult to choose an appropriate strategy until the state of that individual

tumor is known. Emerging imaging approaches have the potential to help in this selection[84].

Furthermore, it is reasonable to argue that improving tumor perfusion could also allow more oxygen and nutrients to be transported in the tumor and thus, increase its growth rate. Additionally, the decompressed vessels could potentially assist metastatic cells to leave the primary tumor and form metastases, which has been shown in pre-clinical studies[85,86]. Therefore, drugs that decompress vessels should only be given with concurrent cytotoxic treatments, such as chemotherapy, nanomedicine, radiation therapy or immune therapy. Specifically, as far as the use of Tranilast is concerned, preclinical studies have indicated that it does not enhance metastatic dissemination [81-83].

Finally, even though our mathematical model is general and the mechanism of Tranilast action was not explicitly incorporated, this could be feasible through its involvement in the TGFβ pathway and could be used for the investigation of further interactions between TGFβ and tumor perfusion that go beyond the scope of the current study.

4 Chapter 4: Hyaluronan-Derived Sewlling of solid Tumors, the contribution of collagen and cancer cells and implication for cancer therapy.

This research has been published in Neoplasia: Voutouri C., C. Polydorou, P. Papageorgis, V. Gkretsi, and T. Stylianopoulos. Hyaluronan-derived swelling of solid tumours, the contribution of collagen and cancer cells, and implications for cancer therapy. Neoplasia 18(12): 732-741. [DOI: 10.1016/j.neo.2016.10.001]

4.1 **Introduction**

Little is known regarding the swelling behavior of tumors, as there are only a few studies reporting osmotic fluid pressure measurements [72], while to the best of our knowledge there is no study to measure and characterize the swelling stress. To this end, we designed and performed a series of experiments, and developed a mathematical model to quantify the swelling behavior of tumors, hereafter referred to as tumor swelling. Our objectives were to relate tissue swelling to the composition and organization of the tumor ECM and the functionality of the tumor vessels, compare swelling stress and osmotic pressure to the total solid stress and IFP, investigate how modifications of the ECM affect swelling and perfusion and indentify the contribution of cancer cells to tumor swelling.

In that regard, we employed four orthotopic tumor models; three xenograft models using the human breast MCF10CA1a, pancreatic MiaPaCa2 and fibrosarcoma HT1080 cell lines and a syngeneic model using the mouse 4T1 breast cancer cell line. Furthermore, cancer cell spheroid models were generated to measure swelling of cancer cells *in vitro*. Finally, because the component of the solid stress owing to interactions with the host tissue and the osmotic fluid pressure cannot be measured experimentally, we developed a triphasic biomechanical mathematical model of tumor growth, which accounted for the solid and fluid phase of the tumor as well as the transport of ions and the fixed charged density. The model was informed and specified using our experimental data and predicted the contribution of each stress type to the mechanics of cancer during progression.

4.2 **Methods**

4.2.1 Cell Culture.

MCF10CA1a human breast cancer cell line and 4T1 mouse mammary carcinoma detailed description of the cell culture methods is given in 3.2.1. HT1080 human fibrosarcoma and MiaPaCa2 pancreatic cell lines were purchased from ATCC.

4.2.2 Animal tumor models and experimental protocols.

Animal tumor models and experimental protocols for MCF10CA1a and 4T1 cells were description is given in (3.2.1). Orthotopic fibrosarcoma tumors and ectopic pancreatic tumors were established by subcutaneous implantation of $5x10^6$ human HT1080 cells or $2x10^6$ MiaPaCa2 cells, respectively, into the left flank of 6-8 week old NOD/SCID mice. Tumor growth was monitored every second day same detailed in (3.2.1). The establishment of human orthotopic pancreatic tumors was performed by surgical implantation of MiaPaCa2 cells directly into the pancreas of 6-week old male CD1 nude mice that were anesthetized by i.p. injection of Avertin (250mg/Kg). Briefly, an incision of the skin was performed in the area above the spleen, followed by a small cut on the surface of the abdominal cavity. Then the spleen along with the underlying pancreas were gently pulled out and the entire pancreatic body was exposed. The organ was slightly spread using forceps and $2.5x10^6$ MiaPaCa2 cells resuspended in 20μl serum-free medium were implanted in the pancreas [87]. Upon implantation the abdominal surface and skin were sutured.

4.2.3 Measurement of swelling solid stress and elastic modulus in murine tumors.

The experimental set up was in line with other studies [17] and based on the confined compression experiment using a high precision testing system (Instron 5944, Norwood, MA, USA). Tumors were excised with a scalpel into specimens of cylindrical shape, 4mm in diameter and 5mm long and they were placed into a chamber (**Fig. *1-8***, **Fig. *4-1*** and **Fig. *4-2***). Therefore, each tumor was divided into 3 to 4 pieces and experiments were performed on all of them. In total 20 tumors were used from each tumor type (n=20). At the top side of the chamber, a piston was adjusted to compress the specimen. At the bottom side of the chamber, a filter paper (Whatman, 20-25μm pore size) was placed to allow fluid flow.

Special care was taken to ensure that the tumor was never in direct contact with fluid during storage, so as to minimize potential leakage of FCD from the specimen before testing. The sample was initially compressed to 10% strain in a period of 2 minutes to make sure the piston applies well on the specimen and that the specimen's response to deformations is measurable. Following, the specimen was held for 20 minutes until the stress relaxed and reached an equilibrium. Subsequently, the specimen was kept at the same strain and NaCl dissolved in ultrapure water was added to the chamber at concentrations ranging from 0.001 to 0.3 M (**Fig. *1-8***). Upon addition of NaCl, the stress increased and reached a new equilibrium. Swelling stress was quantified as the change in stress following NaCl addition (**Fig. *1-8***). Finally, the sample was compressed to 30% strain. This allowed for the measurement of the elastic modulus of the specimen from the slope of the stress-strain curve between 10 and 15% compression (**Fig. *1-8***). As a reference condition for all measurements, we used the physiological ionic concentration (0.15M) where tumor swelling is considered to be zero [17].

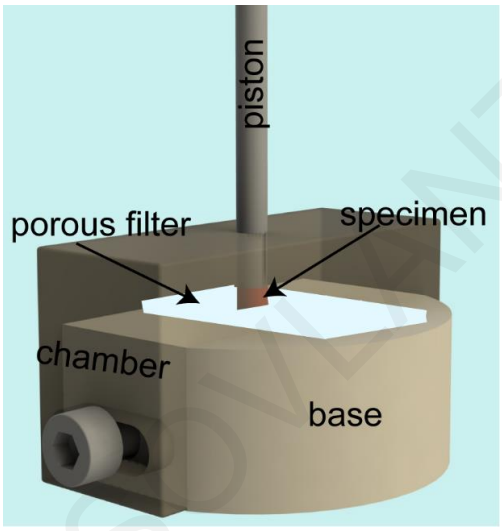

Fig. *4-1.* Design of the experimental set up.

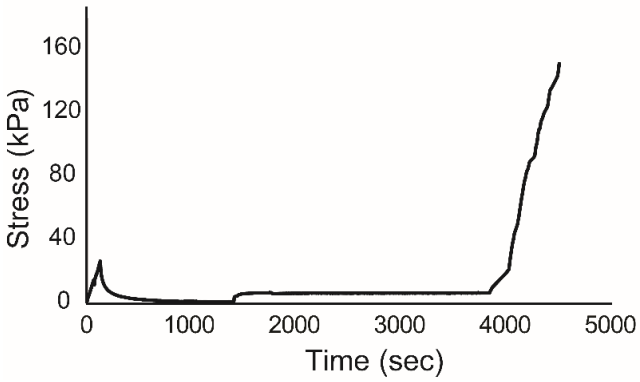

Fig. *4-2*. Typical tumor response during the experimental procedure. The tumor specimen was initially compressed to 10% strain and allowed to relax. Subsequently, solution of NaCl of specified concentration (0.001M) was added causing the swelling of the tissue, which reached a new equilibrium. Finally, the specimen was compressed for another 20% strain. The difference of the two equilibriums was quantified as the swelling stress.

4.2.4 Cancer cell spheroids formation and swelling measurement

MiaPaCa2 and HT1080 cell spheroids were formed using the "hanging drop" technique, as described previously [88,89]. Briefly, cells were trypsinized, counted and put in suspension at a concentration of $2.5x10^4$ cells/ml. Hanging drops containing 500 cells each were placed on the inside of the cover of a culture dish. The plate was brought to its normal positioning and drops were left for at least 24h to allow for spheroid formation. Subsequently, formed spheroids were transferred into wells of a 96-well plate containing 1% agarose using a glass Pasteur pipette. Spheroids were allowed to settle in the new environment being incubated at 37^{o}C for 1h. Pictures were then taken using a Nikon Eclipse optical microscope equipped with a digital camera and this was considered as time zero. Subsequently, NaCl solutions of different molarity were added on top of the spheroids and they were incubated for an additional hour at 37^{o}C. Hypotonic NaCl solution had a concentration of 0.001M, isotonic had a concentration of 0.15M and hypertonic a concentration of 0.3M. Pictures were taken at the 1h time-point, as this proved to be sufficient for cells to equilibrate, and changes in spheroids' size (average of the major and minor axis length) were measured using the Image J software (National Institute of Health software). Two independent experiments were performed and at least six spheroids were monitored for each NaCl condition.

4.2.5 Fluorescent immunohistochemistry

A detailed description of the fluorescent immunohistochemistry is given in (3.2.3).

4.2.6 Interstitial fluid pressure measurement.

Interstitial fluid pressure (IFP) was measured *in vivo* with the wick-in-needle technique[78].

4.3 **Mathematical model.**

4.3.1 Triphasic biomechanical model of tumor growth

To model tumor growth we used the multiplicative decomposition of the deformation gradient tensor[39,47] detailed description of the multiplicative decomposition is given in (2.2.1). Specifically, in this chapter the tensor, **F**, is decomposed into two independent motions: the growth of the tumor, $\mathbf{F}_g$, and the elastic mechanical interactions, $\mathbf{F}_e$, the component that accounts for the generation of residual stresses $\mathbf{F}_r$ equal **I**. Therefore, the final expression of **F** becomes,

$$\mathbf{F} = \mathbf{F}_e\mathbf{F}_g. \qquad (4.1)$$

The tumor was taken to be isotropic and governed by the compressible neo-Hookean constitutive equation with strain energy density function given by

$$W = 0.5\mu(c)\left(-3+II_1\right)+0.5\kappa(c)\left(-1+J_e\right)^2 \qquad (4.2)$$

where μ is the shear modulus, κ is the bulk modulus, J_e is the determinant of the elastic deformation gradient tensor $\mathbf{F}_e$, $II_1 = I_1 J_e^{-2/3}$, and I_1 is the first invariant of the right Cauchy-Green deformation tensor, evaluated from $\mathbf{F}_e$. The shear modulus $\mu=[H_A(1-2\nu)]/[2(1-\nu)]$ and bulk modulus $\kappa=[H_A(1+\nu)]/[3(1-\nu)]$ were calculated assuming Poisson's ratio $\nu=0.45$ from the elastic modulus H_A which was measured experimentally as a function of NaCl external bath concentration c

$$H_A(c) = \left[H_A^{\infty} + (H_A^0 - H_A^{\infty}) \exp\left(-\frac{c}{c_H} \right) \right] \qquad (4.3)$$

where H_A^{∞}, H_A^{0} represent the values at the highest and lowest NaCl concentration, and c_H is a material parameter calculated by fitting the equation to the experimental data (**Fig. *4-7***) and characterize the concentration dependence of the elastic modulus. The Poisson's ratio was assumed to remain unaffected by the NaCl concentration [17].

The concentration c in Eq. *(4.3)*, is the effective NaCl concentration within the tissue, which is related to the concentration of anions c^- and cations c^+ by [90]

$$c = c^{\pm}\left(1 \pm \frac{c^f}{c^{\pm}}\right)^{1/2} \tag{4.4}$$

where c^f is the fixed charged density.

4.3.2 Mass conservation equations

The equations for solid and fluid phase conservation are:

$$\frac{d\varphi^s}{dt} + \nabla \cdot \left(\mathbf{v}^s \varphi^s\right) = S^s \tag{4.5}$$

$$\frac{d\varphi^w}{dt} + \nabla \cdot \left(\mathbf{v}^w \varphi^w\right) = Q \tag{4.6}$$

where φ^s and φ^w are the volume fractions of the solid and fluid phase, respectively and $\mathbf{v}^s$ and $\mathbf{v}^w$ are the corresponding solid and fluid velocities. Q describes the fluid entering the tissue from the vasculature and exiting the tissue through the lymphatics.

The quantity S^s in Eq. *(4.5)* was calculated as[41]:

$$S^s = \frac{\lambda_c c_{ox}}{k_c + c_{ox}} F \varphi^s (1 - \varphi^s) \tag{4.7}$$

where c_{ox} is the oxygen concentration, F is a parameter, which accounts for the inhibitory effect of solid stress on tumor growth, given by $F = \left(1 + \beta \bar{\sigma}\right)$ where β is a constant that describes the dependence of growth on solid stress and $\bar{\sigma}$ is the bulk solid stress calculated as the average of the radial, σ_{rr}, and circumferential ($\sigma_{\theta\theta}, \sigma_{\phi\phi}$) components of the Cauchy stress tensor (i.e., $\bar{\sigma} = \left(\sigma_{rr} + \sigma_{\theta\theta} + \sigma_{\phi\phi}\right)/3$) and λ_c and k_c are constant parameters derived from experimental data[91,92].

The quantity Q in Eq. *(4.6)* was calculated from Starling's approximation[93]:

$$Q = \frac{L_p S}{V}\left(p_v - p\right) - \frac{L_{pl} S_l}{V_l}\left(p - p_l\right) \qquad (4.8)$$

where p_v, L_p and (S/V) are the micro-vascular pressure, hydraulic conductivity and vascular density of the blood vessels, respectively, and p_l, L_{pl} and $(S/V)_l$ are the corresponding quantities for the lymphatics.

4.3.3 The momentum balance equations

The total stress of the tissue is the sum of solid (elastic and swelling) and fluid (IFP and osmotic) stresses. The quasi-static linear momentum balance suggests that the divergence of the total stress tensor should equal zero:

$$\boldsymbol{\sigma}^{total} = \boldsymbol{\sigma}^{s} - T_c\mathbf{I} - p\mathbf{I} + p_{osm}\mathbf{I} \qquad (4.9)$$

$$\nabla\cdot\left(\boldsymbol{\sigma}^{total}\right) = \mathbf{0} \qquad (4.10)$$

$$-k\nabla^2 p + \nabla\cdot\mathbf{v}^{s} = Q + S^{s} + k\left[F_c c^{f}\nabla^2\Psi + F_c\nabla c^{f}\nabla\Psi - RT\left(\varphi - 1\right)\nabla^2 c^{k}\right] \qquad (4.11)$$

where $\boldsymbol{\sigma}^{s}$ is the elastic solid stress tensor, p is the IFP, T_c is the swelling solid stress, p_{osm} is the Donnan osmotic fluid pressure, k is the hydraulic conductivity of the interstitial space, F_c is Faraday's constant, Ψ is the electric potential, c^f is the concentration of the fixed ions, c^k is the sum of the free anions and cations within the tissue, and φ is the osmotic coefficient. The osmotic pressure was then calculated from the concentration of free ions as $p_{osm} = \varphi RTc^{k}$.

The dependence of the swelling stress T_c on the ion concentration was quantified based on the work of Eisenberg and Grodzinsky [17]

$$T_c = \beta_0 \exp\left(-\frac{c}{c_\beta}\right), \qquad (4.12)$$

where β_0 is the swelling stress value at the lowest concentration and c_β is a material constant calculated by fitting the equation to the experimental data.

The ion transport equations for the cations, c^+, and anions, c^-, are[94]:

$$\frac{\partial(\varphi^w c^+)}{\partial t} + \nabla c^+ \cdot \left(\varphi^w \mathbf{v}^w\right) - \nabla \cdot [\varphi^w D^+ (\nabla c^+ + \frac{F_c c^+}{RT} \nabla \Psi)] = 0 \qquad (4.13)$$

$$\frac{\partial(\varphi^w c^-)}{\partial t} + \nabla c^- \cdot \left(\varphi^w \mathbf{v}^w\right) - \nabla \cdot [\varphi^w D^- (\nabla c^- - \frac{F_c c^-}{RT} \nabla \Psi)] = 0 \qquad (4.14)$$

where D^+ and D^- are the diffusion coefficients of the cations and anions, respectively and Ψ is the electric potential. Subtraction and addition of Equations *(4.13)* and *(4.14)*, replacing where $c^- = \frac{c^k - c^f}{2}$ and $c^+ = \frac{c^k + c^f}{2}$ yields:

$$\frac{dc^f}{dt} + \nabla c^f \cdot \mathbf{v}^w = D^a \nabla^2 c^f - \frac{c^f}{\varphi^w} \frac{d\varphi^w}{dt} + D^a \left\{ \begin{array}{l} \nabla \varphi^w \cdot \nabla c^f + \frac{F_c}{RT} \left(\varphi^w c^k \nabla^2 \Psi + \varphi^w \nabla \Psi \cdot \nabla c^k + c^k \nabla \Psi \cdot \nabla \varphi^w \right) \\ + \frac{D^d}{D^a} \left[\nabla \varphi^w \cdot \nabla c^k + \varphi^w \nabla^2 c^k + \frac{F_c}{RT} \left(\varphi^w c^f \nabla^2 \Psi + \varphi^w \nabla \Psi \cdot \nabla c^f + c^f \nabla \Psi \cdot \nabla \varphi^w \right) \right] \end{array} \right\} \qquad (4.15)$$

$$\frac{dc^k}{dt} + \nabla c^k \cdot \mathbf{v}^w = D^a \nabla^2 c^k - \frac{c^k}{\varphi^w} \frac{d\varphi^w}{dt} + D^a \left\{ \begin{array}{l} \nabla \varphi^w \cdot \nabla c^k + \frac{F_c}{RT} \left(\varphi^w c^f \nabla^2 \Psi + \varphi^w \nabla \Psi \cdot \nabla c^f + c^f \nabla \Psi \cdot \nabla \varphi^w \right) \\ + \frac{D^d}{D^a} \left[\nabla \varphi^w \cdot \nabla c^f + \varphi^w \nabla^2 c^f + \frac{F_c}{RT} \left(\varphi^w c^k \nabla^2 \Psi + \varphi^w \nabla \Psi \cdot \nabla c^k + c^k \nabla \Psi \cdot \nabla \varphi^w \right) \right] \end{array} \right\} \qquad (4.16)$$

where $D^a = (D^+ + D^-)/2$ and $D^d = (D^+ - D^-)/2$, R is the gas constant and T is the temperature.

Finally, the electric potential Ψ was calculated by the solution of the Poisson-Boltzmann equation (e.g. [95]):

$$\nabla^2\Psi = \frac{2F_c c_0}{\varepsilon}\sinh\left(\frac{F_c\Psi}{RT}\right) - \frac{F_c c^f}{\varepsilon} \qquad (4.17)$$

where ε is the dielectric permittivity and c_0 is the ion concentration of the tissue.

To calculate the solid stress, the IFP and the concentration of fixed and free ions, we solved the above system of equations. We used the finite element method and the commercial finite element software COMSOL to solve the system. The boundary conditions and the values of the model parameters employed for our analysis are described in the following sessions.

4.3.4 Boundary conditions

We assumed a spherical tumor within a host tissue of cubic shape. The tumor had an initial diameter of 1 mm and the length size of the surrounding tissue was taken to be two orders of magnitude larger to avoid any boundary effects[6]. Because of symmetry we solved for the one eighth of the domain. Symmetry boundary conditions for the displacements, u, the concentrations, the phase volume fractions and the electric potential were employed at the symmetry planes:

$$\begin{aligned}
&\mathbf{n}\cdot\mathbf{u} = 0,\\
&\mathbf{n}\cdot\left(-D^{\alpha}\nabla c^f + \mathbf{v}^w c^f\right) = 0,\\
&\mathbf{n}\cdot\left(-D^{d}\nabla c^k + \mathbf{v}^w c^k\right) = 0,\\
&\mathbf{n}\cdot\left(\nabla\varphi^s\right) = 0,\\
&\mathbf{n}\cdot\left(\nabla\Psi\right) = 0.
\end{aligned} \qquad (4.18)$$

At the interface with the normal tissue the conditions for the continuity of the stresses, displacements and ion concentrations were automatically applied by COMSOL.

To simulate the experimental procedure we followed the methodology and boundary conditions employed previously by Wilson et al. [96]for the study of the swelling behavior of articular cartilage.

4.3.5 Fitting data

To calculate the material constants c_H and c_β in Equations *(4.3)* and *(4.12)* we fitted these equations to the experimental data of the confined compression experiment. We used the

Solver of excel to calculate the values of c_H for the elastic modulus and c_β for the swelling stress by minimizing the sum of the squared errors:

$$\chi^2 = \frac{1}{n}\sum_{i=1}^{n}\left[\left(X^{\exp} - X^{model}\right)_i^2\right] \qquad (4.19)$$

X^{exp} and X^{model} are either the elastic modulus or the swelling stress for the experiment and the mathematical model, respectively and n the number of experimental data.

4.3.6 Model parameters

We modeled murine breast tumors that grow within a period of 14 days. The hydraulic conductivity of the interstitial space, k, was set to 1×10^{-8} cm^2/mmHg-s for the host tissue (i.e., mouse skin), if it is not otherwise stated [93], whereas the hydraulic conductivity of the tumor was found to be 7.73×10^{-8} cm^2/mmHg-s for MCF10CA1a tumors by fitting the experimental measurements of the interstitial fluid pressure (**Fig. *4-3***) and 9.06×10^{-8} cm^2/mmHg-s for the 4T1 tumors. The vascular and lymphatic pressures were set to $p_v = 15\ mmHg$, $p_l = 0.0\ mmHg$ [93]. The hydraulic conductivity of the normal blood and lymphatic vessel wall were taken to be L_p = 3.6×10^{-8} cm/mmHg-s, and $L_{pl}(S/V)_l$ = 0.05 (mmHg-s)$^{-1}$, respectively [93,97]. The hydraulic conductivity of the vessel wall for the tumor tissue is not constant. Since the production of cytokines, that increase vascular hydraulic conductivity and permeability (e.g., VEGF), increases with tumor growth and tumor growth depends on time, we have chosen the dependence of L_p on time. Therefore, in the model L_p is a linear function of time starting from the value of the normal tissue and at day 14, L_p becomes that of a tumor, L_p = 2.8×10^{-7} cm/mmHg-s [6]. The vascular density of the tumor and host tissue was (S/V) = 200 cm^{-1} and (S/V) = 70 cm^{-1}, respectively [93,97]. The shear modulus of the tumors was calculated by the elastic modulus (Eq. *(4.3)*) taking $H_A^0 = 943.34\ kPa$ and $H_A^\infty = 306.06\ kPa$ for the MCF10CA1a and $H_A^0 = 1070$ kPa and $H_A^\infty = 652\ kPa$ for the 4T1 tumors. The parameters β_0, c_β, and c_H appearing in Equations *(4.3)* and *(4.12)*, were found to be β_0=8.32kPa, c_β=0.045M and c_H=0.00998M respectively for the MCF10CA1a tumors and β_0= 3.36 kPa, c_β =0.081M and c_H =0.023M for the 4T1 by fitting Equations *(4.3)* and *(4.12)* to the experimental data. The growth rate parameter λ_c was set

1.6×10^{-4} (s^{-1}) and 0.9×10^{-4} (s^{-1}) for MCF10CA1a and 4T1 tumors, respectively so that model predictions for tumor growth were in agreement with the experimental data (**Fig. *4-4***).

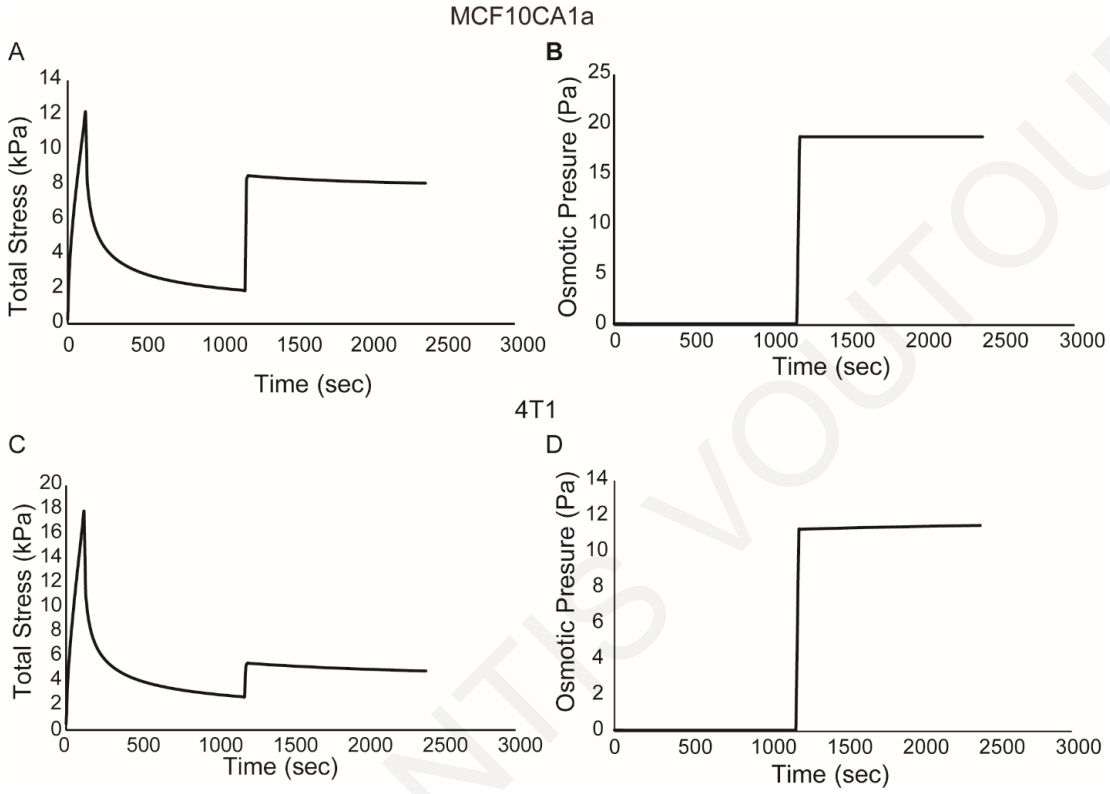

Fig. *4-3*. Simulated the experimental procedure. (A) Total stress for MCF10CA1a. (B) Osmotic pressure for MCF10CA1a. (C) Total stress for 4T1. (D) Osmotic pressure for 4T1, as a function of experiment time.

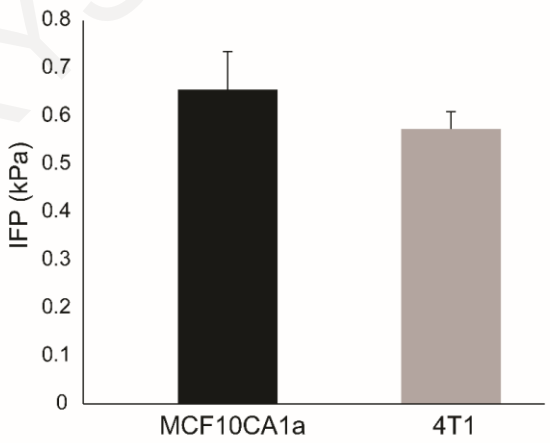

Fig. *4-4*. Experimental measurements of the interstitial fluid pressure for the two cancer cell lines.

The concentration of fixed charges, c^f, of the tumor and the host tissue were estimated from values of the GAG content taken from the literature [15,44] and using a relationship to relate GAG content to c^f [98,99]:

$$c^f = \frac{2 \cdot \rho \cdot [GAG]}{502.5} \qquad (4.20)$$

were 2 are the moles of charge per mole of GAG, ρ is the tumor density set to 1.1 g wet/ml [2], [GAG] is the concentration in mg/g wet and 502.5 is the molecular weight of GAG (g/mole). The amount of GAG in the tumor was assumed to increase linearly with time from zero to a given value within an 8 days period. A nonlinear relationship would change the results only qualitatively. The final amount of GAG was set to 0.4 mg/g wet wt, which corresponds to values taken from the literature [15,44], unless otherwise is stated. The initial concentration of the free ions, c^k, at day 0 was taken to be twice as much as c^f [100]. The physiological values of model parameters are summarized in Table 2.

Table 2. Physiological values of model parameters.

Parameter	**Value**	**Reference**
Fc, Faraday constant	9.64×104 [C·mol−1]	
R, Gas constant	8.314 [J·(mol·K)−1]	
T, Temperature	310 [K]	
ε, Dielectric Permittivity	7.08×10−10 [c2·(J·m)−1]	[101]
D+, Diffusivity of cations	0.5×10−9 [m2·s−1]	[101]
D−, Diffusivity of anions	0.8×10−9 [m2·s−1]	[100]
φ, Osmotic coefficient	0.8	[100]
k, Hydraulic conductivity of normal and tumor tissue	1.0×10−8 [cm2·(mmHg-s)−1] (normal) 7.73×10−8 [cm2·(mmHg-s)−1] (tumor MCF10CA1a) 9.06×10−8 [cm2·(mmHg-s)−1] (tumor 4T1)	[44] This work This work
pv, Vascular pressure	15.0 [mmHg]	[102],[6]

pl, Lymphatic pressure	0.0 [mmHg]	[6]
Lp, Hydraulic conductivity of blood vessel wall of normal and tumor tissue	3.6×10−8 [cm·mmHg-s](normal) 2.8×10−7 [cm·mmHg-s](tumor)	[93]
S/V, Vascular density of normal and tumor tissue	70 [cm-1] (normal) 200 [cm-1] (tumor)	[93]
$Lpl(S/V)_l$, Permeability of Lymphatics	0.05 [(mmHg-s)−1]	[93]
μ, Shear modulus of normal/host tissue	21 [103]	This work
κ, Bulk modulus of normal/host tissue	19.4 [103]	This work
λc, Growth rate parameter	1.6×10-4 [s-1] (MCF10CA1a) 0.9×10-4 [s-1] (4T1)	This work
kc, Growth rate parameter	8.3×10-3 [mol·m-3]	[91,92]
λn, Oxygen uptake parameter	2.2×10-3 [mol·(m3-day)-1]	[91,92]
kn, Oxygen uptake parameter	4.64×10-3 [mol·m-3]	[91,92]
Dc, Oxygen Diffusion in the Tumor	1.55×10-4 [m2·(day)-1]	[104]
Dc, Oxygen Diffusion i Normal Tissue	1.86×10-4 [m2·(day)-1]	[49]
co, Ion Concentration	0.15 [M]	Physiological value
β0, Swelling Stress Parameter	7.05 [103] (MCF10CA1a) 3.36 [103] (4T1)	This work
cβ, Material constant	0.045 [M] (MCF10CA1a) 0.081 [M] (4T1)	This work
$\boldsymbol{H_A^0}$, Elastic Modulus Parameter	943.34 [103] (MCF10CA1a) 1070 [103] (4T1)	This work

H_A^{∞}, Elastic Modulus Parameter	306.06 [103] (MCF10CA1a) 652 [103] (4T1)	This work
cH, Material constant	0.0099 [M] (MCF10CA1a) 0.023 [M] (4T1)	This work

4.4 Results

4.4.1 Osmotic pressure is low for physiological values of GAG and increases with GAG content

First were performed simulations for GAG concentrations for sarcomas, melanomas, breast and colon cancers [15,44]. The amount of GAG increased linearly from zero to 0.4 mg/g wet wt, in a period of 8 days. The GAG content of the host tissue was taken to be constant (4.5 mg/g wet wt). The results of our analysis are shown in **Fig. *4-5***. The concentration of fixed charges, c^f, and the sum of free ions, c^k, increase with time as the GAG content increases.

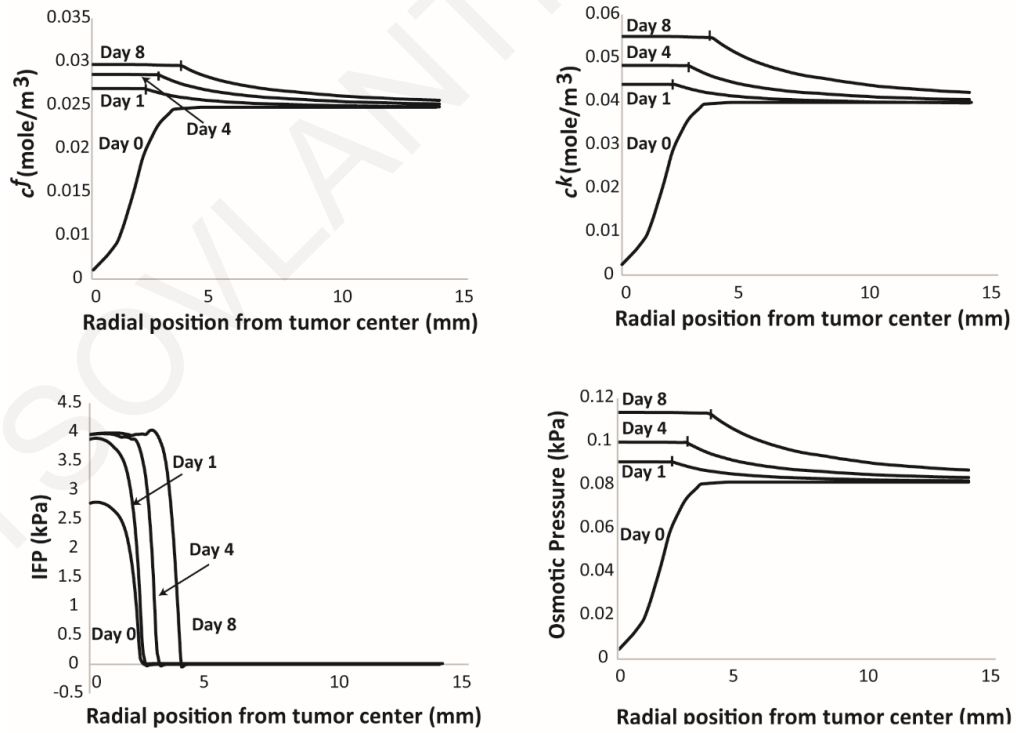

Fig. *4-5*.. Spatial distribution of the concentration of fixed, c^f, and free, c^k, ions, of the interstitial fluid pressure (IFP) and the osmotic pressure in the tumor and the surrounding

normal tissue. The GAG content of the tumor varied from zero to 0.4 mg/g wet wt at day 8. The GAG content of the normal tissue was set to 4.5 mg/g wet wt. Vertical lines on the plot depict the interface of tumor and normal tissue.

The resulting osmotic pressure was negative and negligible compared with IFP. Subsequently, the amount of GAG was increased by an order of magnitude to 4.5 mg/g wet wt, keeping the GAG concentration in the host tissue at 4.5 mg/g wet wt (**Fig. *4-6***). We conclude that an increase in the GAG content of the tumor did not cause any increase in the concentration of fixed and free ions or in the magnitude of the osmotic pressure. After day 0, the charge concentration (fixed and free) inside the tumor becomes comparable to the concentration outside the tumor and it increases slowly with time the subsequent days, as the GAG content in the tumor increases.

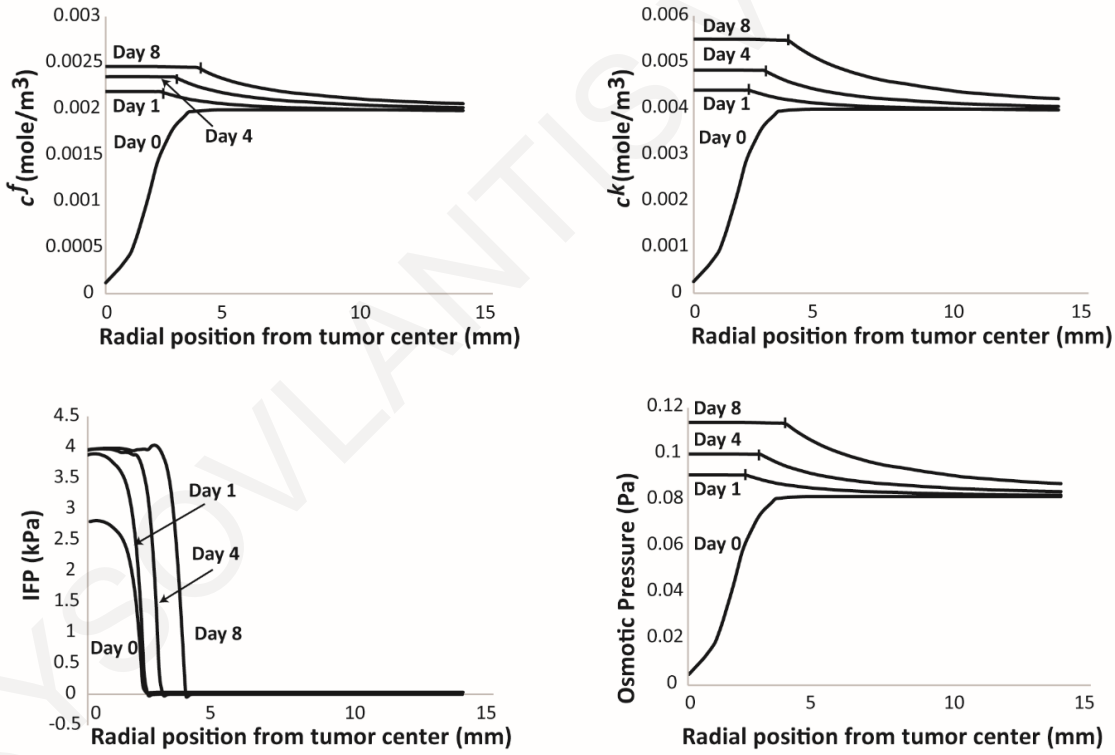

Fig. *4-6*. Spatial distribution of the concentration of fixed, c^f, and free, c^k, ions, interstitial fluid pressure (IFP) and osmotic pressure. The GAG content of the tumor varied from zero

at day 0 to 4.5 mg/g wet wt at day 8. The GAG content of the normal tissue was set to 4.5 mg/g wet wt.

4.4.2 Swelling stress is evident in all tumor models and increases with hypotonic conditions

To measure the swelling stress of the four orthotopic tumor models as a function of the concentration of electrolytes we designed an experimental approach as depicted in **Fig. *1-8***A&1B. The swelling stress increased upon addition of hypotonic saline, while it remained stable at zero upon addition of isotonic or hypertonic solutions (**Fig. *4-7***). As hypotonic solutions exhibit low ionic strength, the Debye length that defines the range of electrostatic interactions increases. For NaCl concentrations closer to or higher than the physiological value of 0.15M, the electrostatic repulsive forces become negligible owing to the small value of the Debye length (~ 0.8 nm) and thus, no swelling was observed. For the lowest concentration of NaCl, the swelling stress ranged from 16.01 ± 1.66 mmHg for the MiaPaCa2 tumors to 75.38 ± 9.03 mmHg for the HT1080. To confirm that the experimental measurements of the swelling stress did not include any component of Donnan osmotic pressure, we simulated the experimental procedure using our mathematical model. The simulations showed that Donnan osmotic pressure should be negligible (**Fig. *4-3***).

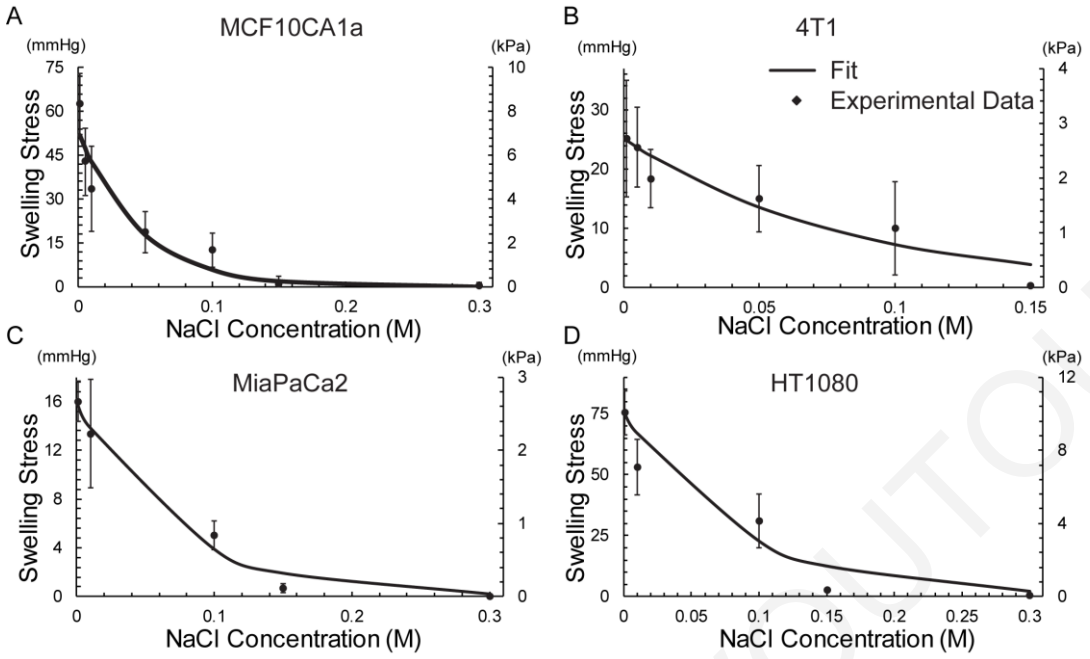

Fig. *4-7.* Experimental data of tumor swelling. Swelling stress as a function of NaCl concentration for the four orthotopic tumor models employed in the study. The experimental data were fitted to Eq. *(4.12)* (solid line).

As far as the elastic modulus is concerned, in all tumor types it exhibited a dependence on NaCl concentration (**Fig. *4-8***). The modulus was higher at low electrolyte concentrations, whereas it dropped to a constant value at higher concentrations, with the exception of MiaPaCa2 tumors in which it remained unaltered for all spectrum of electrolyte concentrations. Swelling stress and elastic modulus fitted well to phenomenological expressions previously employed for cartilage swelling (equations *(4.3)*and *(4.12)*) [17]. The values of the parameters of the equations are given in Table 2.

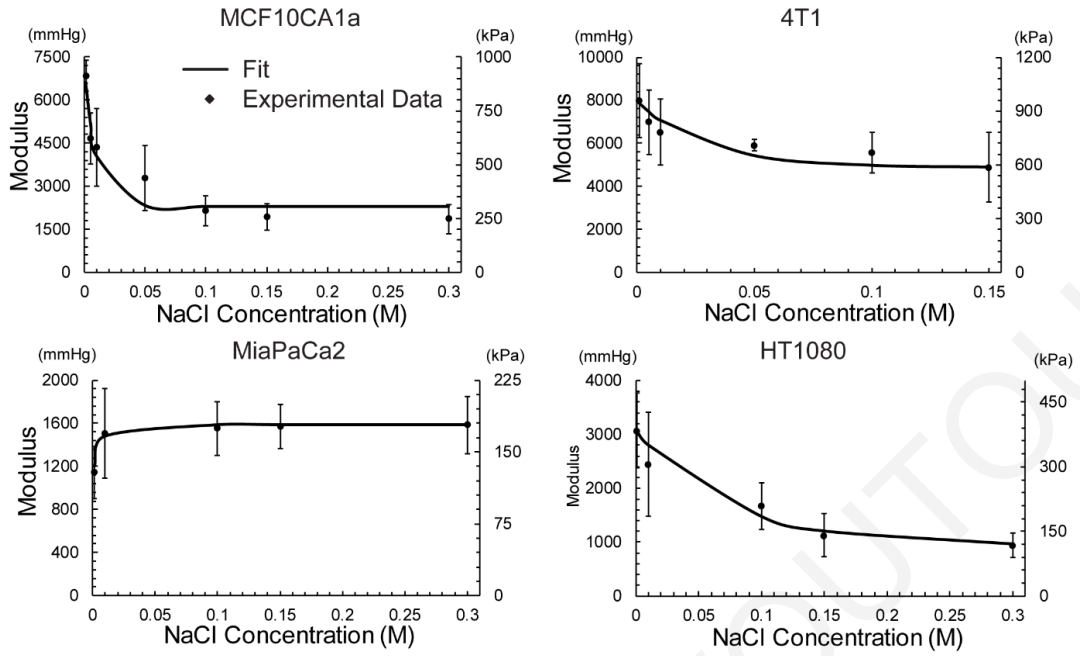

Fig. *4-8*. Experimental data of tumor's elastic modulus. Elastic modulus as a function of NaCl concentration for the four orthotopic tumor models employed in the study. The experimental data were fitted to Eq. *(4.3)*(solid line).

4.4.3 Tumor swelling increases linearly with the ratio of hyaluronan to collagen area fraction

In order to investigate the ECM structure of the tumor types studied, immunofluorescence analysis of collagen and hyaluronan, was performed. Even though other types of glycosaminoglycans might contribute to tumor swelling, we focused on the examination of hyaluronan owing to its abundance in the tumors tested, and because it has been reported to be a target for stress alleviating therapeutic strategies [32-34]. MiaPaCa2 and HT1080 tumors had higher levels of collagen and hyaluronan compared to the two breast tumor types, MCF10CA1a and 4T1 (**Fig. *4-9*** and **Fig. *4-10***). As the data of the lowest electrolyte concentration (0.001M) exhibited the largest variation in swelling, they were selected for further analysis. Thus, correlations between the swelling stress and the composition of the tumor ECM were sought. There was no correlation between swelling and hyaluronan or collagen content alone (**Fig. *4-9***B&C). Interestingly however, when swelling stress was plotted as a function of the relative area fraction of hyaluronan to collagen, a strong linear correlation was revealed that was verified in all tumor types tested (**Fig. *4-9***D), indicating a

dependence of tissue swelling on tumor's collagen and hyaluronan composition. This finding is in accordance with *in vivo* studies in cartilage tissue as well as with studies using *in vitro* models [105-107].

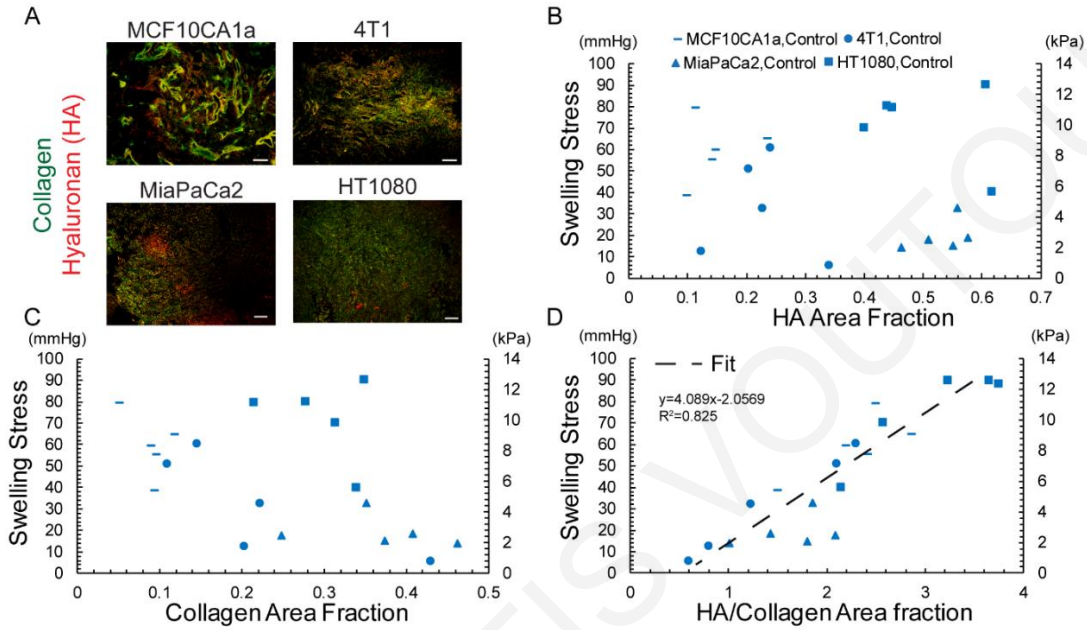

Fig. *4-9*. Effect of ECM composition on swelling stress. (A) Representative immunofluorescence staining sections for hyaluronan (HA) and collagen (scale bar 100μm), (B) Swelling stress as a function of HA area fraction and (C) collagen area fraction showing no correlation. (D) Swelling stress is linearly proportional to the ratio of HA/collagen area fraction (y=4.089x-2.0569, R^2=0.825). Five tumor specimens (n=5) from each tumor type were used.

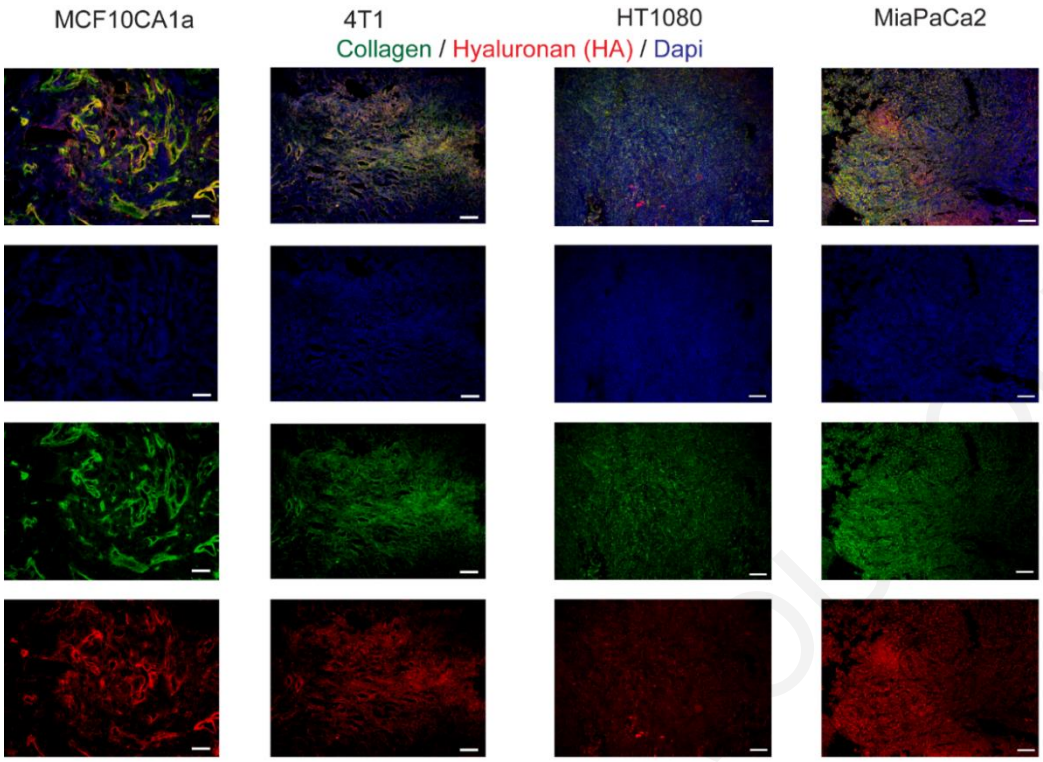

Fig. *4-10*. Representative immunofluorescence staining for collagen and hyaluronan. The different collagen composition and organization is shown. Scale bar 100 μm.

4.4.4 Swelling contributes to tumor mechanical function contrary to negligible Donnan osmotic pressure

Contrary to swelling stress and IFP that can be measured experimentally, there is no *in vivo* or *ex vivo* technique to measure the solid stress owing to mechanical interactions of the tumor with the host tissue and the Donnan osmotic pressure. As mentioned above, in order to assess all components of mechanical stress and investigate their contribution to tumor mechanics, we developed a triphasic biomechanical model of tumor. The solid phase was modeled as a compressible neo-Hookean material with a Poisson's ratio of 0.45 [6] and the elastic modulus was taken by the experimental data accounting for the dependence on ion concentration (**Fig. *4-8***, Equation *(4.3)*). The fluid phase was modeled as ideal (i.e., of no viscosity) and governed by Darcy's law [6]. The hydraulic conductivity of the tumor appearing in Darcy's law was defined by fitting the model to the IFP experimental data (**Fig. *4-4***). To determine the values of model parameters related to tumor growth rate, we fitted the model to our experimental data of tumor growth (**Fig. *4-11*** and Table 2).

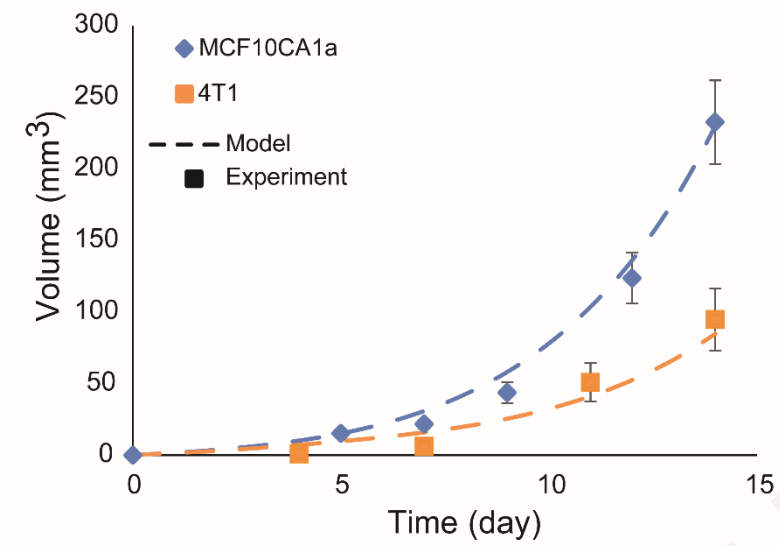

Fig. *4-11*. Model fit to experimental data of tumor growth for the two tumor types employed in the study.

Model predictions for the solid stress, swelling stress, IFP and osmotic pressure during tumor progression are shown in **Fig. *4-12*** and **Fig. *4-13*** for MCF10CA1a and 4T1 tumors, respectively. In both tumor types, the compressive solid stress exerted externally on the tumor by the host was in the order of 300 mmHg (40 kPa) and the swelling stress was ~ 52.5 mmHg (7 kPa) for MCF10CA1a and ~ 25.13 mmHg (3.35 kPa) for the 4T1 tumors. IFP calculations were similar to the experimental measurements, i.e., in the range of 4.5-5.2 mmHg (0.6-0.7 kPa) (**Fig. *4-12*** and **Fig. *4-4***), and the calculated Donnan osmotic pressure ranged from 0.52 to 0.6 mmHg (0.07- 0.08 kPa). Therefore, our calculations indicated that solid stress (external and swelling) is much larger than interstitial fluid pressure and that swelling stress can be important to tumor mechanics, whereas Donnan osmotic pressure is negligible.

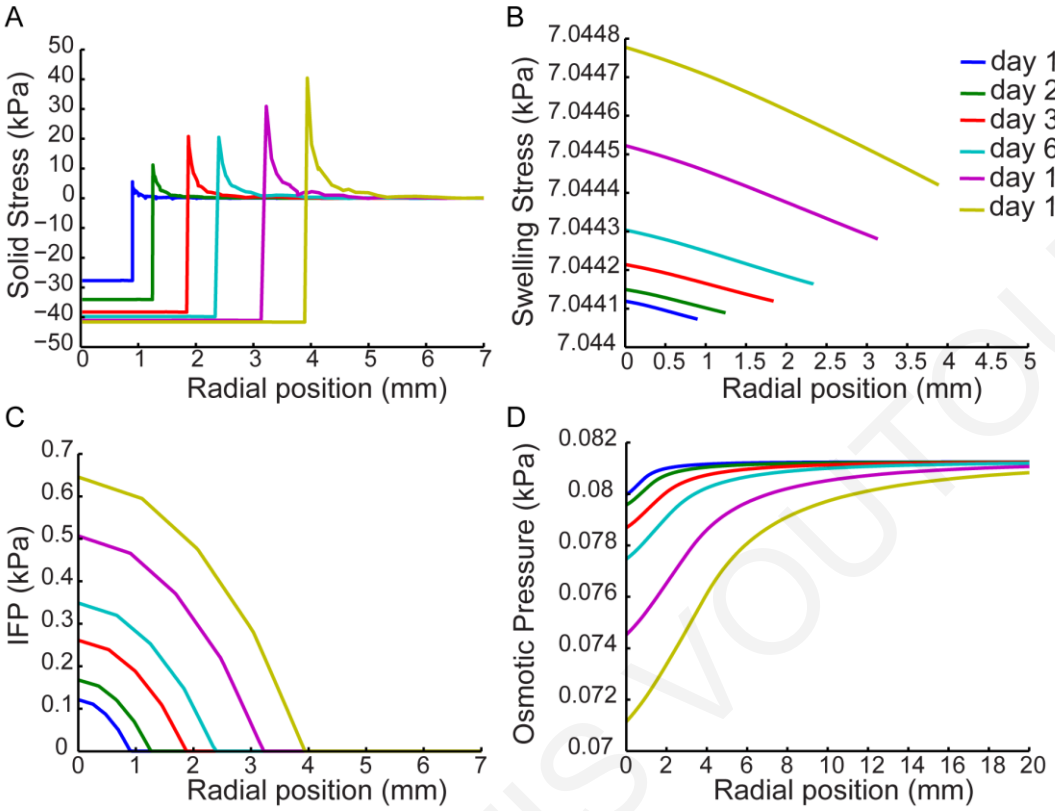

Fig. *4-12*. Model predictions, of (A) solid stress applied externally to the tumor by the host tissue, (B) swelling stress, (C) interstitial fluid pressure (IFP) and (D) Donnan osmotic fluid pressure as a function of the radial position from tumor center at different times. Model was specified for the MCF10CA1a tumors. External solid stress is compressive in the tumor interior and becomes tensile at the periphery, swelling stress remains spatially and temporally uniform, IFP increases with time owing to increased vessel permeability and drops to normal (zero) values at the periphery, while osmotic pressure is negligible.

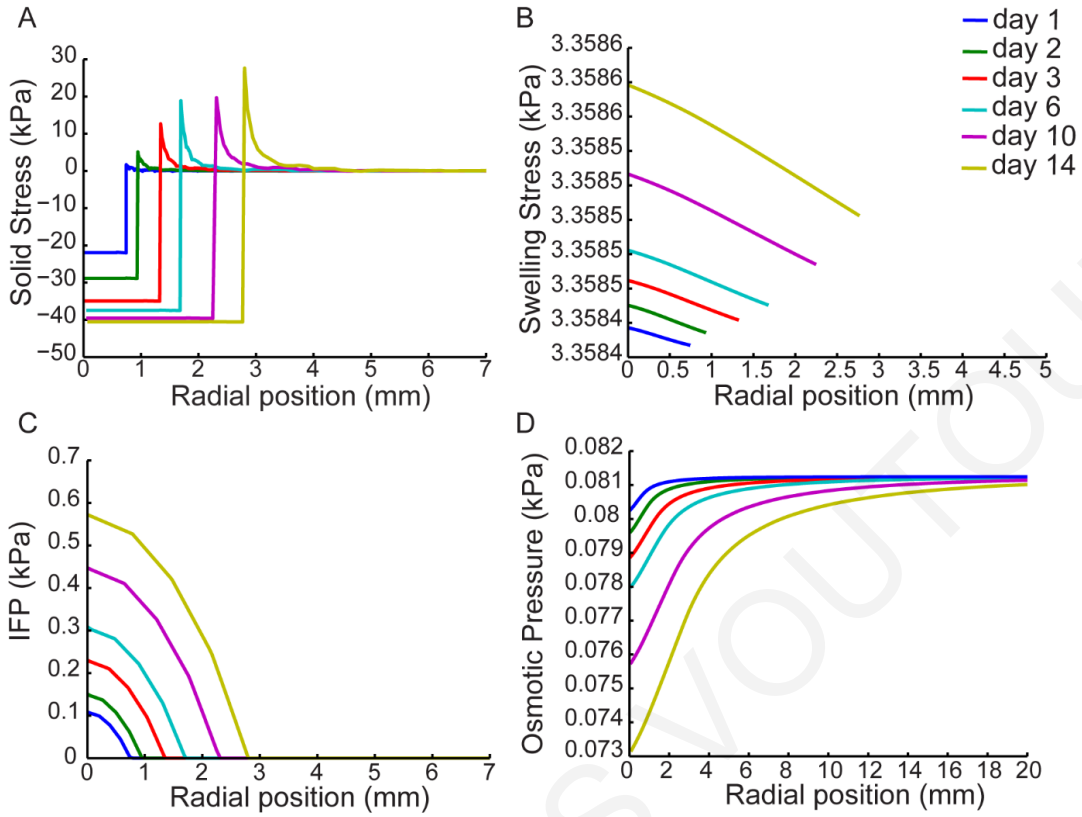

Fig. *4-13*. Model predictions of elastic solid stress (A), swelling solid stress (B), interstitial fluid pressure (IFP) (C) and Donnan osmotic fluid pressure (D) as a function of the radial position from tumor center at different times. Model was specified for the 4T1 tumors.

To further explore the predictive capabilities of the model, a parametric analysis was performed varying the hydraulic conductivity of the tumor and the initial concentration of fixed charges that mostly affect model predictions (**Fig. *4-14*** and **Fig. *4-15***). From the analysis we conclude that model results only change quantitatively.

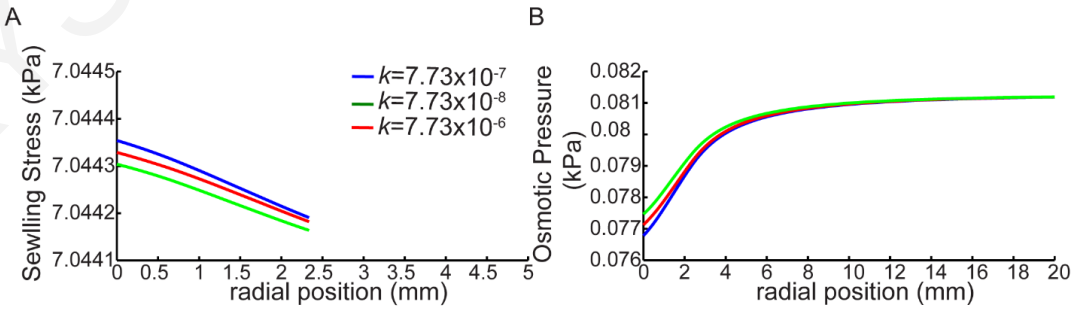

Fig. *4-14*. Model predictions for the effect of tumor's hydraulic conductivity, k [cm^2/mmHg-s], on swelling solid stress (A) and Donnan osmotic fluid pressure (B) as a function of the radial position from tumor center at different times. Model was specified for the MCF10CA1a tumors.

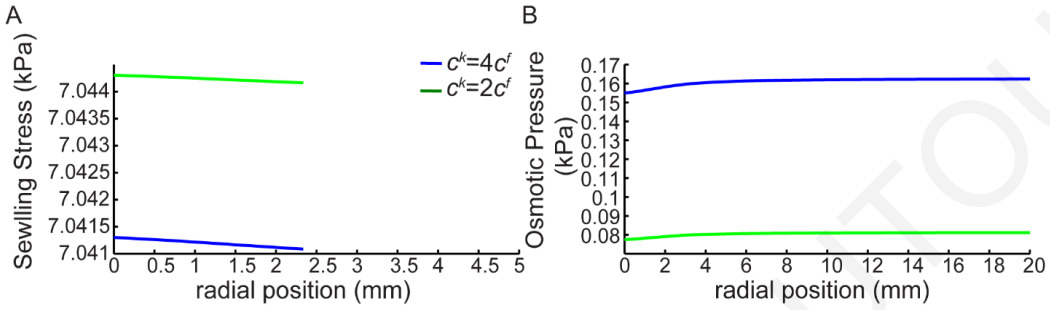

Fig. *4-15*. Model predictions for the effect of free and fixed ions on swelling stress and Donnan osmotic pressure. Two different initial concentrations of free ions of the tumor, $c^k = 2c^f$ and $c^k = 4c^f$, were employed and the results of swelling solid stress (A) and Donnan osmotic fluid pressure (B) as a function of the radial position from tumor center at different times are shown. Model was specified for the MCF10CA1a tumors.

4.4.5 Enzymatic and drug-mediated reduction of ECM components modulates tumor swelling

To further investigate the contribution of collagen and hyaluronan to tumor swelling we treated ectopic MiaPaCa2 and orthotopic HT1080 tumors with enzymes (collagenase and hyalurodinase) as well as with pirfenidone (Esbriet®), a drug prescribed for idiopathic pulmonary fibrosis. Intratumoral injection of 1000 U in 50µl collagenase or 25µg in 50µl hyaluronidase, 2 hours prior to tumor removal significantly reduced collagen and hyaluronan levels, respectively, whereas daily oral administration of 500 mg/Kg pirfenidone reduced levels of both constituents (**Fig. *4-16***A-C). Interestingly, our results show that swelling of hyaluronidase-treated tumors reduced drastically to negligible levels, that of pirfenidone-treated tumors decreased, while the swelling of collagenase-treated tumors increased (**Fig. *4-16***D). Hence, the observed swelling response is exclusively due to hyaluronan and that collagen itself restricts swelling.

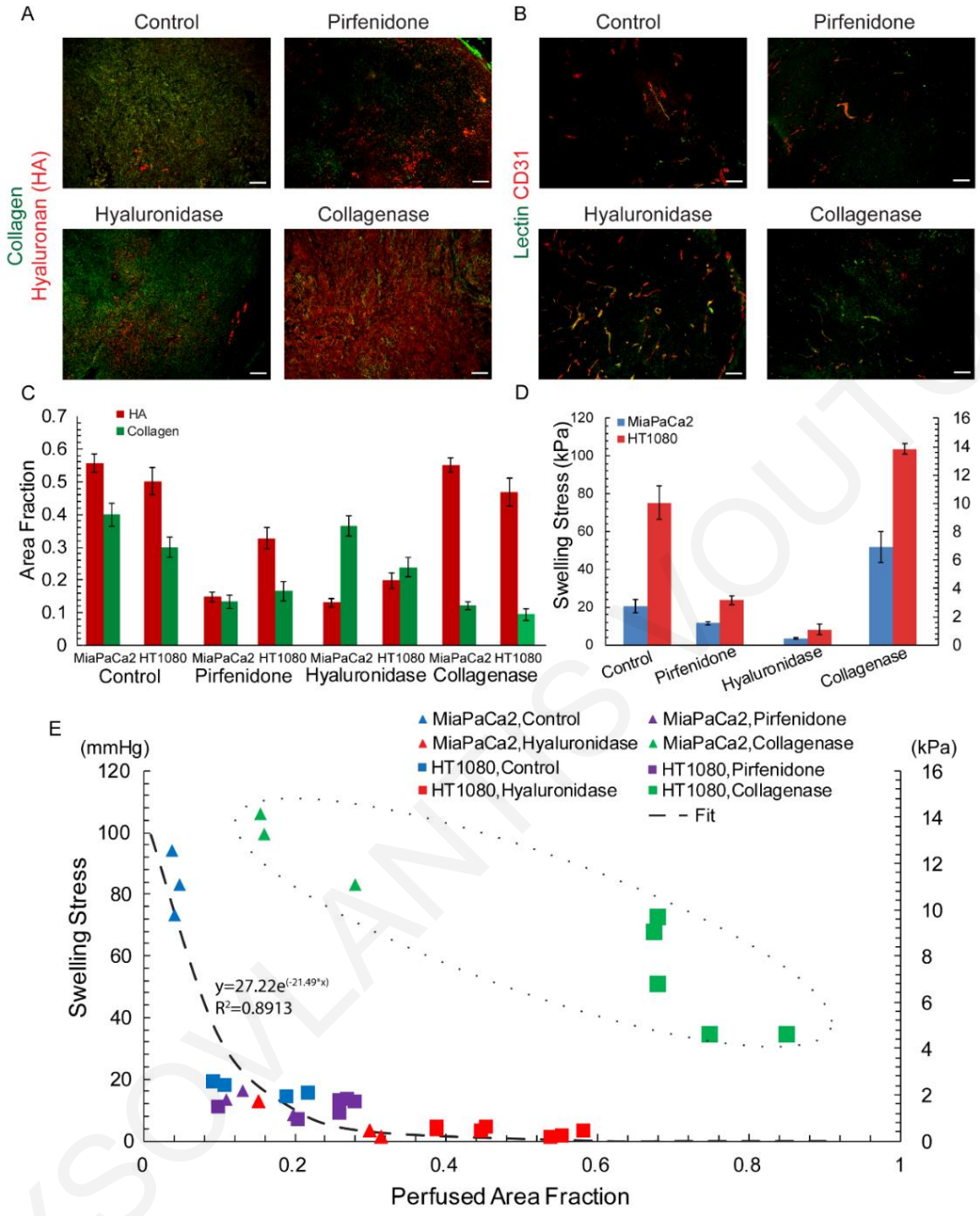

Fig. ***4-16.*** Effect of tissue swelling on vessel perfusion. (A) Representative immunofluorescence staining sections for hyaluronan (HA) and collagen (scale bar 100μm), (B) typical immunofluorescence staining sections for lectin and CD31 (scale bar 100μm), (C) Area fraction of collagen and HA and (D) Swelling stress for the control and treated tumors tested. Changes in stress between the control and each of the treated groups is statistically significant ($p<0.05$) for both tumor types. (E) Fraction of perfused vessels

as a function tumor swelling showing their exponential decay relationship (dash line, y=-27.22e(-21.49x), R^2=0.8913) and also the different mechanism of collagen reduction to improve perfusion (dash cirle).

4.4.6 Tumor swelling inversely correlates with blood vessel functionality

It is well known that solid stress can compress intratumoral blood vessels reducing their diameter and tumor perfusion[11,79]. To investigate any potential correlation of swelling to tumor perfusion, we examined perfused vessels by administering biotinylated lectin to mice via intracardiac injection prior to tumor removal for all tumor types and treatment conditions tested. Interestingly, there is an inverse relationship, well-expressed by an exponential decay function, between the perfused vessel fraction and the swelling stress (**Fig. *4-16***E). A similar inverse correlation between tumor perfusion and the tumor ECM fraction has also been shown previously in pertinent research [32]. Interestingly, hyaluronidase treatment radically reduced tumor swelling to negligible levels and significantly improved its perfusion. Collagen reduction following collagenase treatment on the other hand, was associated with improved perfusion even though exhibiting increased swelling stress, thus implying a different mechanism of action. This could be due to the fact that collagen fibers restrict tissue swelling and their depletion allows the tumor to further swell and relax, alleviating intratumoral swelling stresses. Pirfenidone treatment also resulted in improved perfusion, showing that repurposing of commonly used anti-fibrotic drugs can be used to enhance perfusion, and drug delivery, ultimately improving therapy.

4.4.7 Cancer cell swelling does not contribute to tissue-level effects

Recent work by McGrail et al showed that cancer cells regulate their tonicity and swell in order to survive and resist compressive forces that are developed in the tumor's interior[9]. To determine whether cancer cell swelling can account for the changes we observe in tumor swelling, we employed an *in vitro* model. Specifically, MiaPaCa2 and HT1080 cancer cells were used to generate tumor spheroids that were embedded in a 1% agarose matrix and changes in the spheroids' size was recorded in relation to changes in osmolarity. Our findings show that cancer cell spheroids swelled by approximately 70-80% for a hypotonic solution

(0.001M, NaCl) and shrunk by 60-70% when the solution was changed to hypertonic (0.3 M, NaCl) (**Fig. *4-17***A&B). To convert the observed deformations to stresses, we measured the mechanical properties of the agarose gel and found the Young's modulus to be 3.6 ± 0.56kPa (**Fig. *4-17***C). Subsequently, using our mathematical model, the growth of the spheroids within the agarose matrix was simulated and the stress developed in the spheroids was calculated. **Fig. *4-17***D presents the calculated by the model stress for varying the elastic properties (Young's modulus) of cancer cell spheroids with values taken from the literature [41]. According to our calculations, cancer cell swelling should not contribute to tissue-level swelling of the tumor.

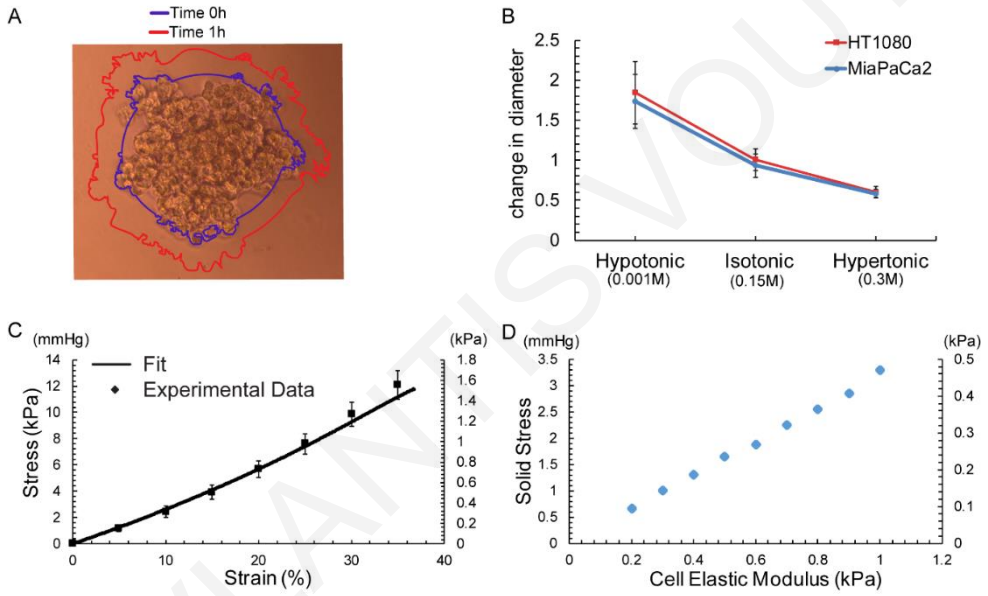

Fig. *4-17*. Cancer cell swelling (A) microscope image of a spheroid. Lines depict the perimeter of the spheroid before (0h) and an hour after addition of electrolyte solution. (B) Change in spheroid's diameter as a function of the tonicity for HT1080 and MiaPaCa2 cancer cells (C) stress strain curve for 1% agarose gel, (D) stress developed on the spheroids as a function of their elastic modulus.

4.5 **Discussion**

It has been well established that mechanical forces modulate the tumor microenvironment and pathophysiology and determine in large part tumor progression and response to therapy[13,59]. However, there has been no study to date to describe the swelling behavior

of tumors, the magnitude of swelling stress and Donnan osmotic pressure, the dependence of swelling on tissue composition, and its contribution to tumor perfusion, which plays a critical role in the efficacy of cancer therapy [77,108]. Here, we performed a series of *in vivo* and *in vitro* experiments coupled with mathematical modeling to elucidate these issues. We found that swelling is evident in breast, pancreatic and sarcoma cell lines and it is high enough to compress intratumoral blood vessels and affect tumor perfusion. Interestingly, our analysis revealed the same linear correlation between swelling stress and the ratio of hyaluronan to collagen content for all tumor types tested, suggesting that tumor swelling is mainly due to the ECM composition. This conclusion was further supported by the finding that tumors treated with hyaluronidase exhibited negligible swelling, while swelling was increased in tumors treated with collagenase. This can be explained by the fact that collagen fibers are stressed during swelling and hinder tissue expansion owing to their property to resist tensile loads. Moreover, this observation regarding the role of collagen is consistent with pertinent studies on cartilage [105,106] and a recent *in vitro* study [107]. Last but not least, *in vitro* experiments on tumor spheroids showed that cancer cell swelling should not significantly contribute to tumor swelling.

More importantly, we found that swelling affects tumor perfusion, and thus could be a significant factor affecting drug delivery. Perfusion is compromised in many tumor types, particularly in desmoplastic tumors (e.g. breast and pancreatic cancers and sarcomas), which are considered to be rich in collagen and/or hyaluronan, because of intratumoral blood vessel compression [2,32,108]. Hypo-perfusion in turn, causes hypoxia, which promotes tumor growth in multiple ways, and reduces the efficacy of radiation therapy, immunotherapy, and chemo/nanotherapy because of the inability of oxygen, immune cells and drugs to reach the tumor site in sufficient amounts [28,77,108,109]. In previous research, we proposed and proved experimentally that alleviation of solid stresses has the potential to decompress tumor blood vessels and thus, improve perfusion [2,32]. In this work, we found that swelling stress is high enough to cause vessel compression and that modulation of swelling stress levels can result in vessel decompression (**Fig. *4-18***) and improved perfusion. Interestingly, our data indicated that alleviation of tumor swelling by hyaluronan depletion as well as increase in tumor swelling by reduction of collagen levels are two different mechanisms to improve perfusion. Furthermore, we demonstrated the repurposing of commonly used anti-fibrotic

drugs could comprise a novel approach to improve delivery of cytotoxic agents by enhancing perfusion.

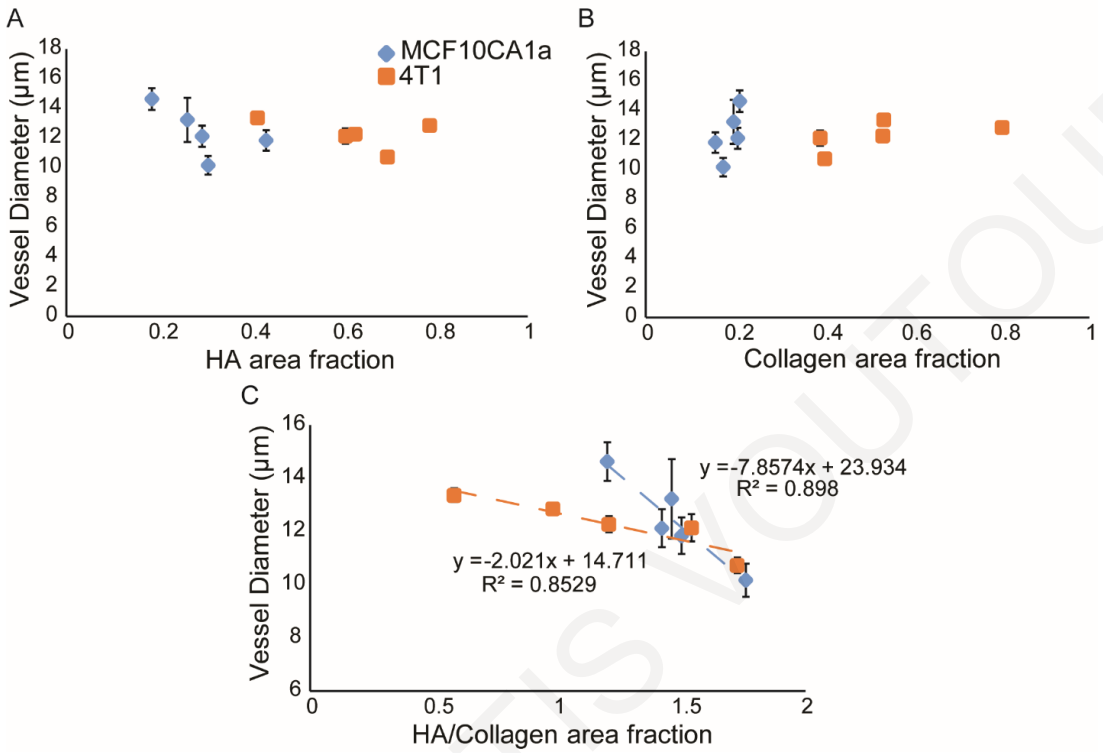

Fig. *4-18*. Blood vessel diameter as a function of tissue composition. (A) No correlation of the modulus to the hyaluronan (HA) or (B) collagen area fraction was observed. (C) Vessel diameter decreased linearly with the HA/collagen area fraction.

5 Chapter 5: Accumulation of mechanical forces in tumors is related to hyaluronan content and tissue stiffness

This research is under review in PLoS ONE: Voutouri C. and T. Stylianopoulos. Accumulation of mechanical forces in tumors is related to hyaluronan swelling and tissue stiffness.

5.1 **Introduction**

Even though hyaluronan swelling could potentially contribute to the accumulation of growth-induced stresses in tumors, any correlation between the two types of stress has not been explored thus far. Importantly, pertinent studies for engineered tissues and blood vessels show a correlation between growth-induced and swelling stress which was analysed in Chapter 4 [107,110-114].

Solid tumors often stiffen as they grow at the expense of the surrounding host tissue. Tissue stiffening is caused by an increase in the amount of cancer cells, stromal cells and the extracellular matrix constituents, mainly collagen and hyaluronan. As a tumor grow, cancer cells divide faster than normal cells, the tumor becomes stiffer and displaces the surrounding normal tissue, which allows tumor progression. Therefore, tumor growth is associated with the generation of mechanical stresses that affect tumor progression and response to treatment in several ways [12,13,59,115,116]. The three tissue-level types of solid stress (i.e., stress of the solid components) that are developed in tumors are: i) stress applied externally to the tumor by the host tissue, ii) growth-induced (or residual) stress, which is accumulated in the tumor and remains even if the tumor is excised, and iii) swelling stress owing to the swelling behavior of the hyaluronan [8].

Swelling stress is developed owing to the negatively charged hyaluronan chains that exert repulsive, “charge-to-charge”, electrostatic forces on each other as they are closely packed in the dense tumor extracellular matrix, causing swelling of the tissue (Fig. 2B) [10,17,117,118]. Swelling stress can be measured by placing a tissue specimen in a confine chamber and measuring with a load cell the force that is developed when the electrolyte

concentration of the chamber is changed to hypotonic, the tissue tries to swell but the chamber prevents its expansion[10,17]. Selective depletion of hyaluronan decreases tissue swelling, while depletion of collagen increases swelling suggesting that collagen fibers, which strongly support tensile loads, are stretched during tumor swelling and thus, resist further swelling of the tumor. Interestingly, using different types of breast and pancreatic cancers as well as soft tissue sarcomas, we found that swelling stress correlates extremely well with the ratio of the hyaluronan to the collagen content through a linear relation (*(5.4)* in Materials and Methods) [10].

Even though both collagen and hyaluronan content contribute to the accumulation of growth-induced stresses in tumors, an analysis of which of the two components is more closely related to this stress type is lacking in the literature. Additionally, a comparison between growth-induced and swelling stress in the same tumors has not been performed thus far. Importantly, pertinent studies for engineered tissues and blood vessels show a correlation between growth-induced and swelling stress [107,110-114]. Furthermore, data from our group have showed that treatment with the anti-fibrotic drugs tranilast or pirfenidone reduced hyaluronan content and hence the growth-induced and swelling stresses in tumor-treated samples [10,113,114]. These data further suggest a potential correlation between the two stress types.

To this end, the objective of this study is the measurement of growth-induced stress in tumors and the investigation of its relation to collagen and hyaluronan content as well as its comparison to swelling stress First, we experimentally measure the tumor opening and elastic modulus in mock-treated tumors and tumors treated with tranilast or pirfenidone. Combining these experimental measurements with mathematical modelling, we predict the growth-induced stress levels for each tumor following our previously developed methodology [2]. Immunofluorescence analysis of the compared groups is also employed to assess the reduction of collagen and hyaluronan components. This is confirmed by measuring the area fraction of collagen and hyaluronan. Swelling stress is predicted by the ratio of hyaluronan to collagen content [10]. Finally, the inter-dependence of tumor opening, growth-induced stress, swelling stress, tumor composition and elastic modulus is explored.

5.2 Material and Methods

5.2.1 Cell Culture

MCF10CA1a human breast cancer cells (Karmanos Cancer Institute, Detroit, MI, USA) and 4T1 mouse mammary carcinoma cells (ATCC) were employed. A detailed description of the cell culture is given in (3.2.1).

5.2.2 Drugs and reagents

Tranilast (Rizaben®, Kissei Pharmaceutical, Japan) was solubilized with 1% $NaHCO_3$ followed by heating at 70ºC for 1 h (33.3mg/ml) [82,83,113]. Pirfenidone (Esbriet®, Roche Pharmaceuticals, Switzerland) was solubilized with sterile water followed by warming at 60ºC for 30min [114]. A detailed description given in (3.2.1). We have previously showed that these drugs can reduce levels of hyaluronan and collagen type I in murine breast tumor models [113,114].

5.2.3 Animal tumor models and experimental protocols

A detailed description of the animal tumor models (MCF10CA1a and 4T1 cells) and experimental protocols is given in (3.2.1).

5.2.4 Fluorescent immunohistochemistry

A detailed description of the fluorescent immunohistochemistry is given in (3.2.3).

5.2.5 Tumor opening Measurements

When tumors reached a size of ~ 1cm in diameter, they were excised and their three dimensions were measured (width, height, thickness). For the tumor opening measurement, a cut was made along the tumor's longest axis (~80% of its thickness). The tumor was then allowed to relax for 10min to allow for any transient, poroelastic response to vanish and the opening at the surface of the tumor was measured as shown in **Fig. *1-6***A [2]. During the experimental procedure the tumors remained hydrated by addition of phosphate buffer saline (PBS). A detailed description given in (3.2.2).

5.2.6 Mechanical testing measurements for calculation of elastic modulus

The unconfined compression experimental protocol was employed for the measurement of the elastic modulus. Following the tumor opening experiment a part of the tumor 3×3×2mm (length × width × thickness) was selected and tumor specimens were loaded on a high precision mechanical testing system (Instron, 5944, Norwood, MA, USA). Stress-strain experiment was performed to a final strain of 30% with a strain rate of 0.05mm/min, the minimum rate the system can apply to avoid any poroelastic effects. The elastic modulus was calculated from the slope of the stress-strain curve in the range of 25-30% strain. A representative stress-strain curve is shown in **Fig. *5-1***

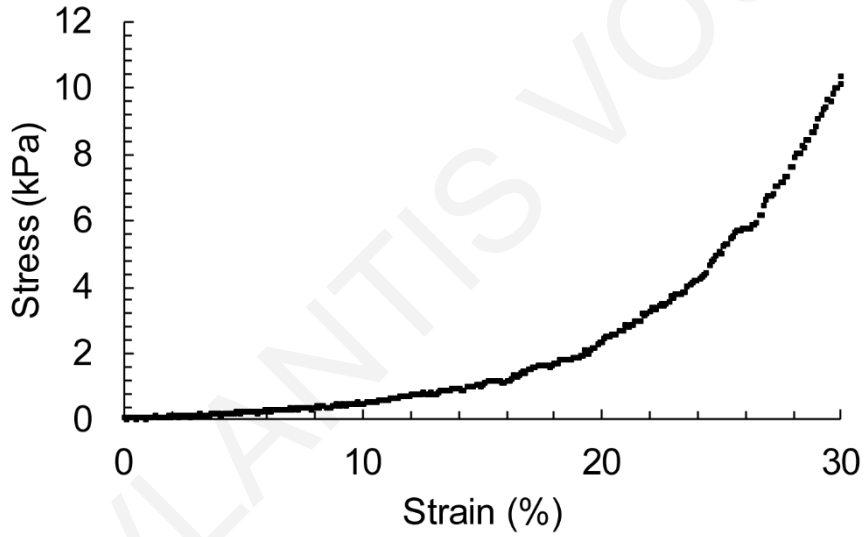

Fig. *5-1*. Representative stress-strain curve of the confined compression experiment.

5.2.7 Mathematical model for calculation of growth-induced stress

To calculate the growth-induced stress from the tumor opening experiment a mathematical model was employed to simulate the opening experiment and convert the measured strain to stresses following our previous methodology (**Fig. *1-6***B)[2]. Notice that this methodology was developed to quantify a residual stress that is stored during growth. Growth-induced stress can also be purely due to cells and can be measured with methodologies that employ

multicellular spheroids growing in permeable elastic capsules[119]. Here we present a summary of our mathematical model.

The tumor mechanical properties were taken to be isotropic and governed by the compressible neo-Hookean constitutive equation with strain energy density function given by [2,7,43,48,120]

$$W = 0.5\mu\left(-3+II_1\right)+0.5\kappa\left(-1+J\right)^2 \qquad (5.1)$$

where μ is the shear modulus, κ is the bulk modulus, J is the determinant of the deformation gradient tensor **F**, and II_1 is the second invariant of the right Cauchy-Green deformation tensor, evaluated from **F**. The values of the shear and bulk modulus that was used in the simulations were calculated for each tumor specimen separately using the experimentally measured elastic modulus and assuming a Poisson's ratio of 0.4 [6,7].

The momentum balance equation

The total stress of the tissue was take to be the sum of solid (elastic and growth-induced) stress [6,10,38,120,121]. The quasi-static linear momentum balance equation suggests that the divergence of the total stress tensor should equal zero:

$$\nabla\cdot\left(\boldsymbol{\sigma}^{total}\right)=\nabla\cdot\left(\boldsymbol{\sigma}^{s}-\boldsymbol{\sigma}^{g}\right)=\mathbf{0} \qquad (5.2)$$

where $\boldsymbol{\sigma}^s$ is the elastic solid stress tensor and $\boldsymbol{\sigma}^g$ is the growth-induced stress tensor.

The elastic Cauchy stress tensor, $\boldsymbol{\sigma}^s$, was calculated by the strain energy density function as:

$$\boldsymbol{\sigma}^{s} = J^{-1}\mathbf{F}\,\frac{\partial W}{\partial \mathbf{F}^{T}} \qquad (5.3)$$

The growth-induced stress tensor $\boldsymbol{\sigma}^g$ represents the stress that was released in the tumor during the opening experiment. Following our assumption for isotropic growth, $\boldsymbol{\sigma}^g$ was assumed to be an isotropic tensor.

5.2.8 Model Parameters and formulation

For each tumor specimen and based on its three dimensions and elastic modulus, we developed a 3D Finite Elements model using the Solid Mechanics Physics in in COMSOL

Multiphysics (COMSOL, Inc., Burlington, MA, USA) (**Fig. *5-4***) to solve the model equations. The number of finite elements comprising the model was 526,467. A mesh-independence analysis of the solution of the model is presented in **Fig. *5-2***. The model has two different regions, the first is the intratumoral region, where the compressive stress at equilibrium is equal to growth-induced stress. The second region is the collagenous peripheral layer that forms a capsule surrounding the tumor. The capsule was assumed to be free from any growth-induced stress component and to be stiffer than the inner region of the tumor (i.e., higher shear modulus) [2]. We measured the thickness of the peripheral layer from histological analysis of the tumors and found it to range from 1.5% to 15% relative to the thickness of the tumor **Fig. *5-3***. For the baseline calculations we took the modulus of the peripheral layer to be 10 times stiffer than the tumor and the thickness of the layer was taken to be 10% of the thickness of the tumor [2]. To calculate the range of growth-induced stress on each tumor sample, we assumed for the modulus and the thickness of the peripheral layer to vary from 1.5 to 20 and from 1.5% to 15% relative to the modulus and thickness of the tumor, respectively. This range is shown in the figures using bars.

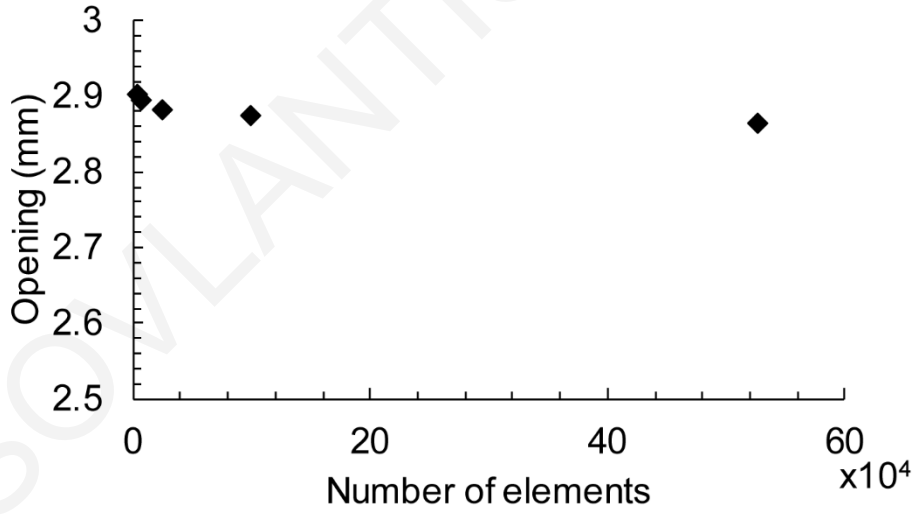

Fig. *5-2*. Mesh-independence analysis of the finite elements model. The number of elements varied from 4,079 to 526,467 elements and the predicted by the model tumor opening was used for comparison.

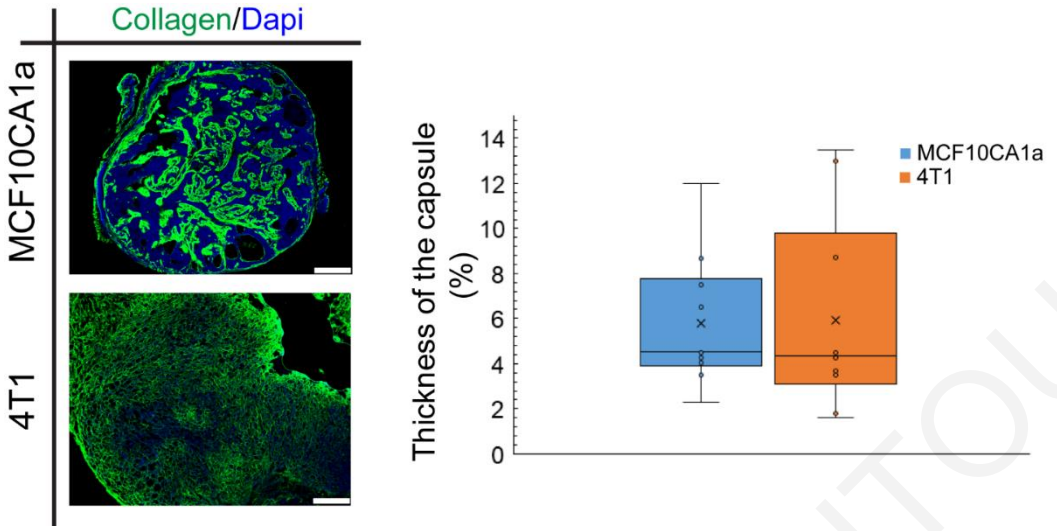

Fig. *5-3*. Measurement of the thickness of the periphery layer. Representative samples of immunofluorescence staining for collagen and dapi showing the peripheral layer of the tumors (left). Image analysis was used to calculate the relative thickness of the peripheral collagen layer (capsule) and results are presented in the box plot (n=8). Scale bar:500μm.

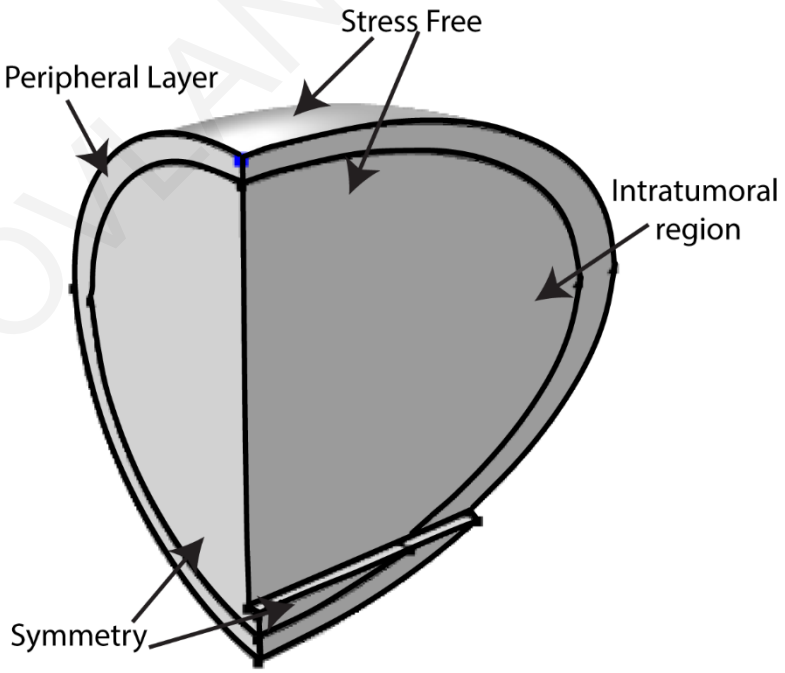

Fig. *5-4*. Boundary Conditions employed by the computational model for calculations of growth-induced stress. Schematic of the tumor domain, we modeled the one-quarter of the domain assuming spherical symmetry. The applied boundary are: stress free at the free surface of the tumor and symmetry at the planes of symmetry. The schematic also shows the two different regions: intratumoral and peripheral region.

The simulation took into account the state of the tumor right after the cut has been made, modeling the bulging of the intatrumoral region and the opening of the tumor. We run simulations for each tumor specimen considering its specific dimensions and mechanical properties and our goal was for the model to match the experimentally measured tumor opening. To achieve this we varied the value of the isotropic growth-induced stress, $\boldsymbol{\sigma}^g$ (*(5.2)*) so that the difference between the experimentally measured and computed tumor opening to be less than 0.01mm.

Because of symmetry we performed our analysis in one-quarter of the domain. The boundary conditions employed are illustrated in **Fig. *5-4***.

5.2.9 Calculation of swelling stress

A detailed description of the calculation of swelling stress can be found in [10]. Briefly, a tumor specimen was placed in a confine chamber and compressed with a piston to 10% strain. Subsequently, it was allowed to relax completely so that any poroelastic response to vanish. Then, NaCl solution of specified concentration was added to the chamber to change the tonicity of the tissue, keeping the position of the piston fixed. Hypotonic solutions caused the swelling of the tissue and the force developed on the fixed piston was measured with a load cell. In previous research, we found a linear relationship to correlate extremely well the swelling stress to the ratio of hyaluronan to collagen area fraction [10]. This relationship is

$$[\text{swelling stress}]=4.09\cdot[\text{HA/collagen}] - 2.057, \qquad (5.4)$$

where [HA/collagen] is the ratio of the area fraction of hyaluronan to collagen. Notice that this equation applies to the most hypotonic solution (0.001M NaCl) employed in [10] and it was found with the use of mathematical modeling to be the same to the *in vivo* situation.

5.2.10 Statistical Analysis.

The experimental data are presented as means with standard errors. We performed an analysis of variance, or ANOVA/Tukey-Kramer paired analysis using the software program GraphPadPrism (6.0 for Windows; GraphPad Prism Software Inc., San Diego, CA) at the 95 percent confidence interval (CI).

5.3 **Results**

5.3.1 Experimental measurements for control and treated breast tumors

Orthotopic MCF10CA1a and syngeneic 4T1 tumors were treated with tranilast (200mg/kg) or pirfenidone (500mg/kg) orally on a daily basis, while there was also mock-treated groups as control. When tumors were excised, they were cut along their longest axis and allowed to relax before measuring the tumor opening (**Fig. *1-6*** and **Fig. *5-5***A,B). In agreement with previous studies [2], tumor opening was higher in the control tumors compared to the treated groups, exhibiting higher levels of growth-induced stress. The results of the immunofluorescence staining and mechanical testing analyses are presented in **Fig. *5-5***C-F. More specifically, tranilast treatment reduced collagen and hyaluronan content in both tumor types. Pirfenidone even though it has been shown to affect both ECM components [10,114], in this study it reduced only hyaluronan levels without affecting collagen (**Fig. *5-5***C,D and **Fig. *5-6***). Modulation of the tumor extracellular matrix resulted in softer tumors of lower elastic modulus compared to the control groups with the exception of tranilast in MCF10CA1a tumors (**Fig. *5-5***E,F). Subsequently, mathematical analysis of the experimental measurements was employed for the assessment of the growth-induced and swelling stress (**Fig. *5-5***G,H). Both stress types were reduced for the treated groups compared to the control. Interestingly, the levels of growth-induced and swelling stress in the corresponding groups were similar.

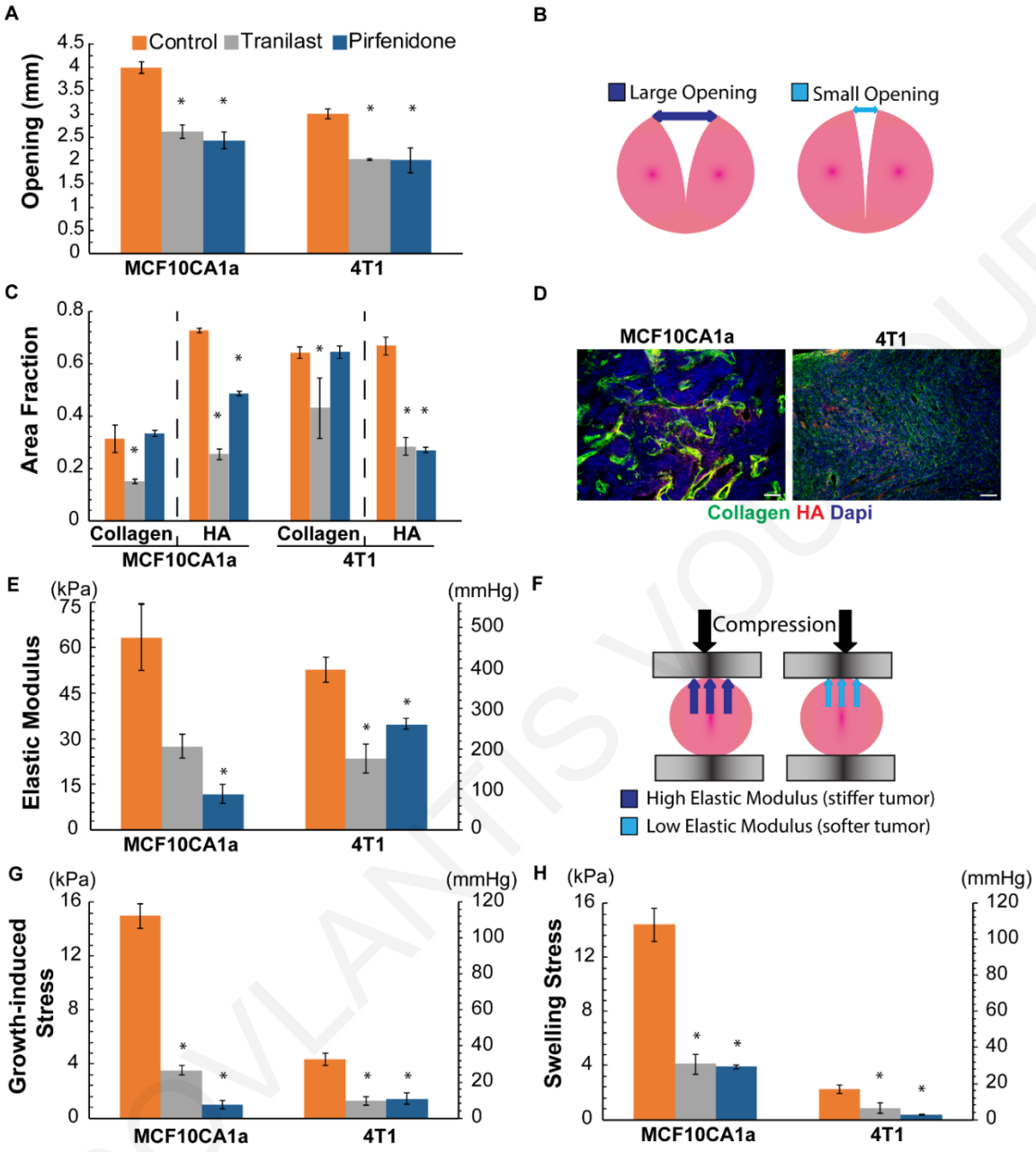

Fig. 5-5. Experimental measurements and calculations for MCF10CA1a and 4T1 tumors. (A): Tumor opening experimental data for the control and the two treated groups. (B): Schematic of the tumor opening measurement, (C): Area fraction quantification of collagen and hyaluronan (HA), (D): Representative immunofluorescent images (Control) for collagen, HA and Dapi (scale bar:100μm). (E): Elastic Modulus experimental data for the two tumors and the different groups employed. (F): Schematic of mechanical measurements, high and low modulus is associated with stiffer and softer tumors, respectively, (G): Growth-induced stress calculated using mathematical modeling, (H):

Swelling stress calculated from the ratio of hyaluronan to collagen content using Eq. *(5.4)*. Error bars represent the standard error.

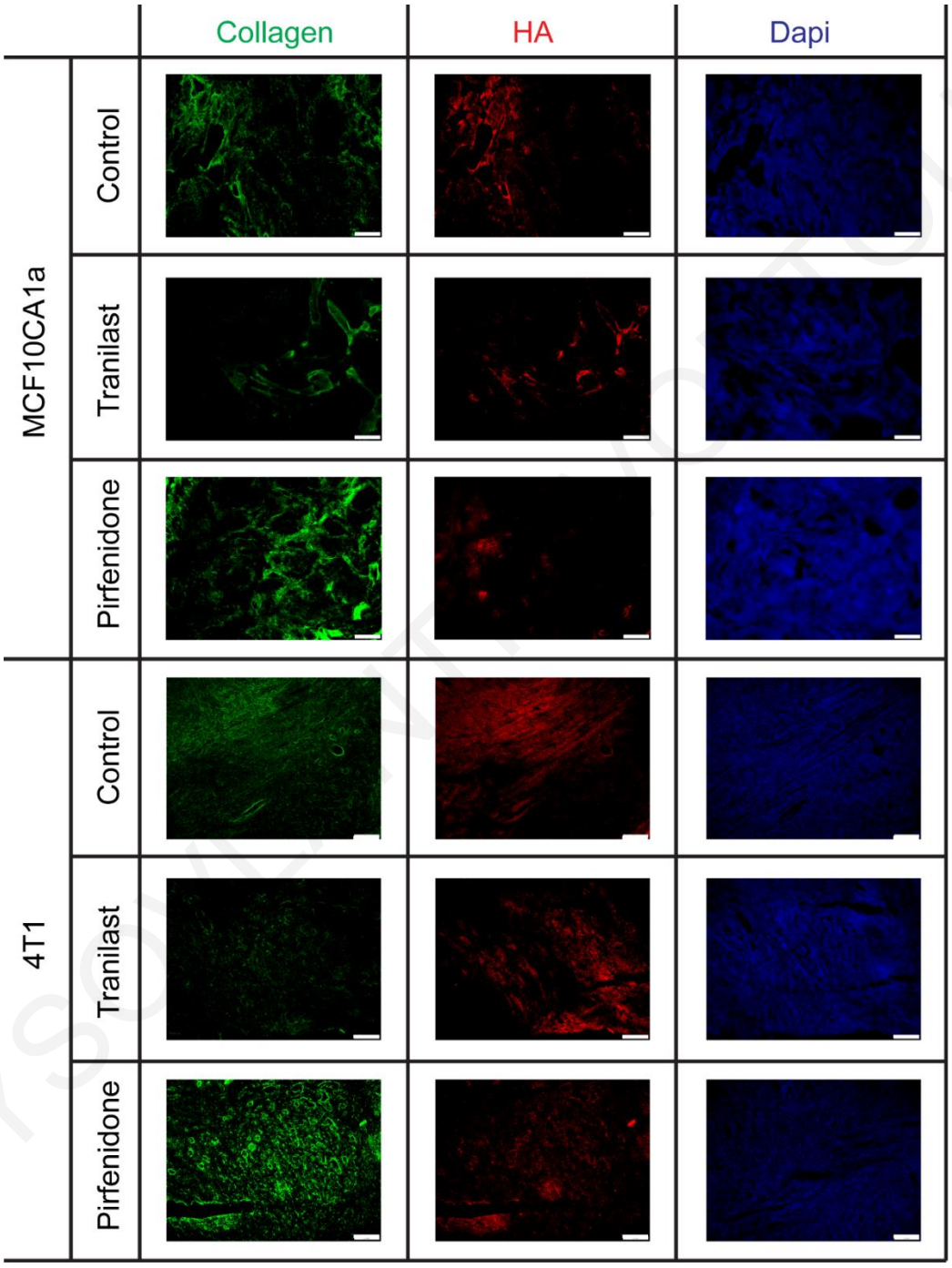

Fig. *5-6.* Representative immunofluorescence staining for collagen, hyaluronan (HA) and Dapi. The different compositions and organization is shown. Scale bar 100 μm

5.3.2 Tumor opening increases with hyaluronan area fraction

To investigate any potential correlation between the accumulation of growth-induced stress with the extracellular matrix structure, we plotted in **Fig. *5-7*** the tumor opening as a function of collagen or hyaluronan area fraction and also as a function of the ratio of the two. Even though there was no correlation between tumor opening and collagen content, there was a good linear correlation with hyaluronan area fraction and a partial correlation with the ratio of hyaluronan to collagen. These results indicate the critical role of hyaluronan in the accumulation of mechanical forces in tumors, further supporting the relationship between growth-induced and swelling stress.

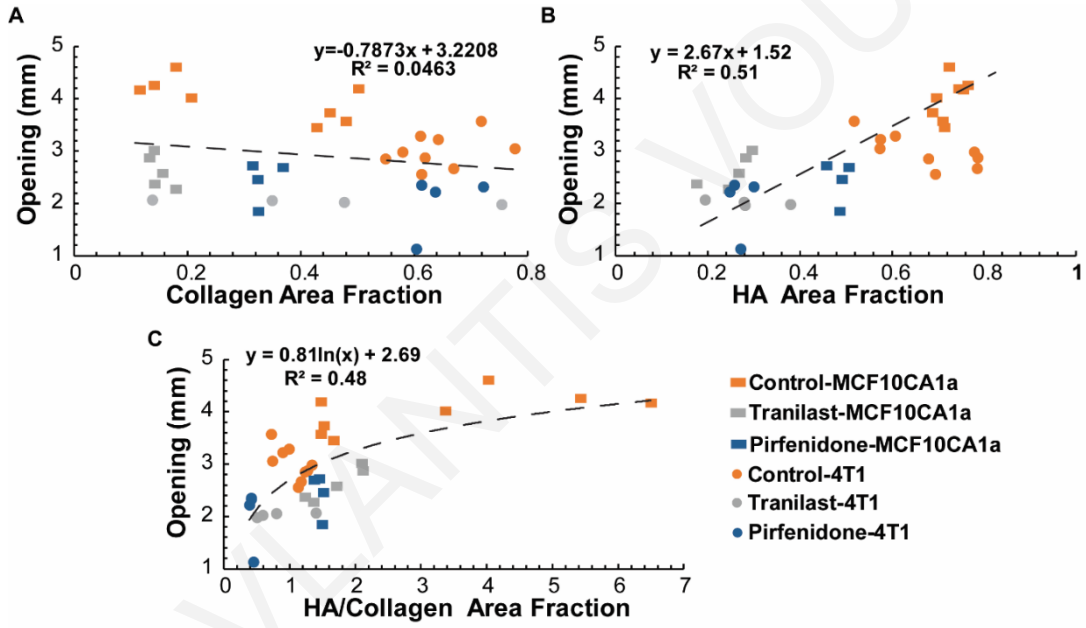

Fig. *5-7*. Effect of ECM composition on tumor opening. (A) Collagen area fraction does not correlate with opening, whereas there is a correlation of tumor opening with hyaluronan (HA) area fraction (B) and the ratio of HA/collagen area fraction (C). Five tumor specimens (n=5) from each tumor type were used.

5.3.3 Growth-induced stress is related to hyaluronan content and tissue stiffness

Subsequently, we estimated the growth-induced stress taking into account our experimental measurements of tumor opening and elastic modulus and using mathematical modeling. **Fig. *5-8*** presents the growth-induced stress as a function of tumor content as well as tumor opening and elastic modulus. In agreement with our findings in **Fig. *5-7***, there is a dependence of growth-induced stress on hyaluronan to collagen area fraction (**Fig. *5-8***C). Additionally, there is a good correlation of growth-induced stress with the elastic modulus of the tissue (**Fig. *5-8***E) as well as with the product of tumor opening with elastic modulus (**Fig. *5-8***F), implying that tissue stress relaxation follows a linear elastic behavior.

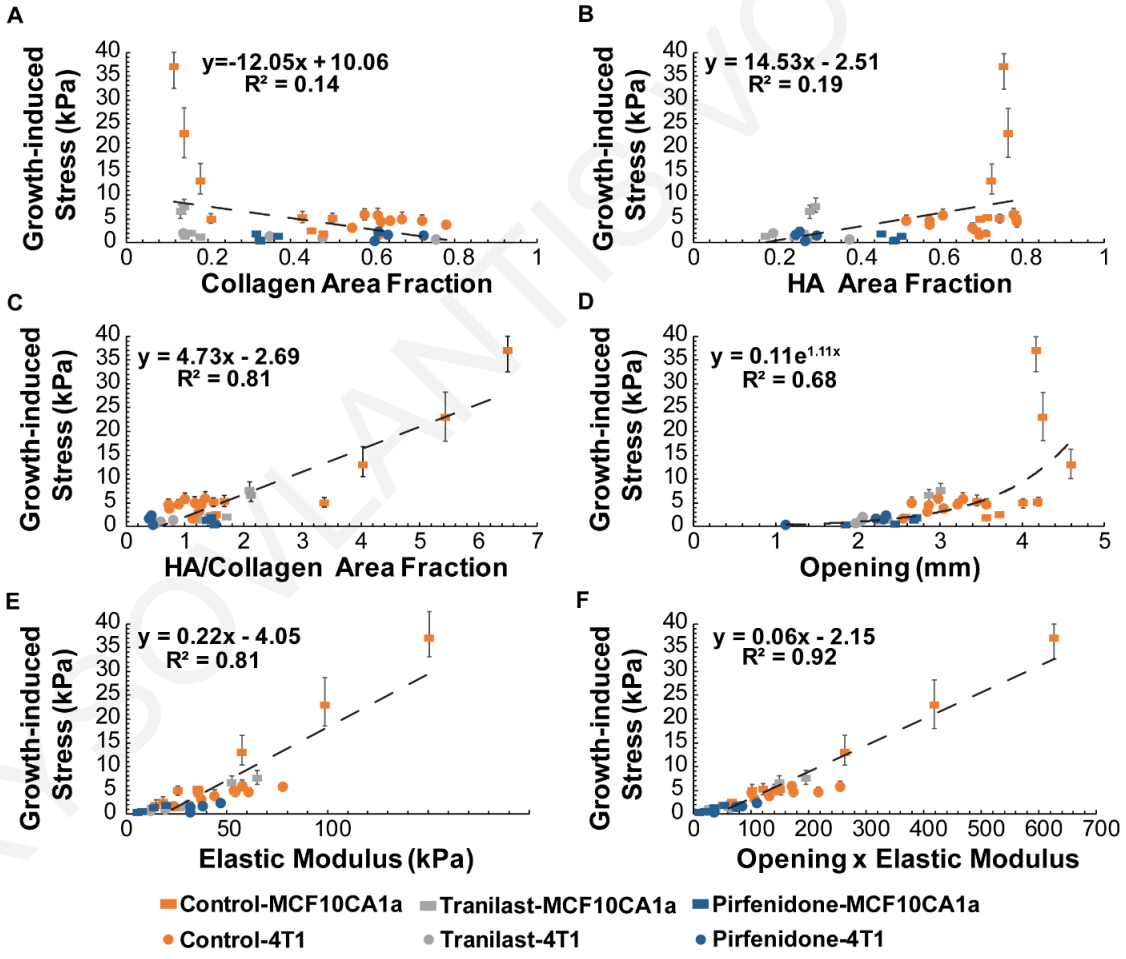

Fig. *5-8*. Effect of ECM composition and mechanical properties on growth-induced stress. (A) Collagen or (B) hyaluronan (HA) area fraction is not associated with growth-induced stress, whereas a relation seems to exist when (C) the ratio of HA/collagen area

fraction is employed. (D) Growth-induced stress does not depend on tumor opening but there is a good correlation between growth-induced stress and tumor elastic modulus (E) as well as with the product of tumor opening and elastic modulus (F). Error bars represent the range of estimated growth-induced stress.

5.3.4 Swelling stress is comparable to growth-induced stress levels

Using our previous analysis [10], we calculated the swelling stress from the ratio of hyaluronan to collagen content *(5.4)* and compared the values with the growth-induced stress levels (**Fig. *5-9***). Interestingly, there is a good correlation between the two types of stress that fits well along the y=x line (**Fig. *5-9***). Given the fact that hyaluronan swelling is a cause of growth-induced stress and taking collectively our results into account we can conclude that growth-induced stress is largely determined by tumor swelling and swelling associated stress.

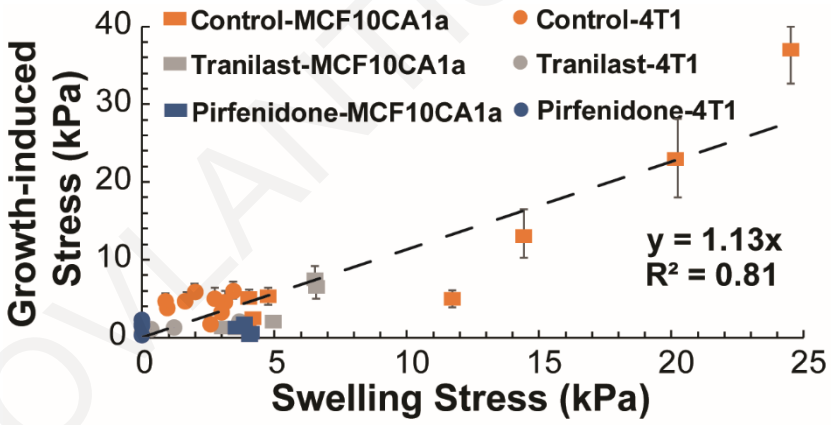

Fig. *5-9*. Swelling stress agrees well with growth-induced stress. The good correlation of the two types of stress is given by the good fit along the y=x dash line.-Error bars represent the range of estimated growth-induced stress.

5.3.5 Parametric analysis of geometrical and mechanical parameters for the calculation of growth-induced stress

Geometrical parameters that affect calculation of the tumor opening experiment are the thickness of the cut as well as the thickness of the peripheral capsule. For the baseline simulations, we took the thickness of the cut to be 80% of the tumor thickness and the thickness of the capsule 10% of that of the tumor according to our experimental protocol and previous research [2]. Additionally, the relative stiffness of the capsule to the stiffness of the tumor might also affect tumor opening. In our simulations, we assumed the peripheral capsule to be 10 times stiffer than the inner tumor region [2]. To test how the values of these parameters affect our calculations of growth-induced stress, we performed a parametric analysis. As shown in **Fig. *5-10***, the thickness of the cut as well as the stiffness of the capsule have a minor or small effect on tumor opening, whereas the thickness of the capsule compared to the tumor size is more critical in our calculations of growth-induced stress. However, histological analysis has shown that the thickness of this capsule, which is a result of remodeling of peripheral collagen fibers, does not exceed 10% of tumor thickness. Therefore, any change in the values of the parameters considered here is not expected to affect the conclusions of our study.

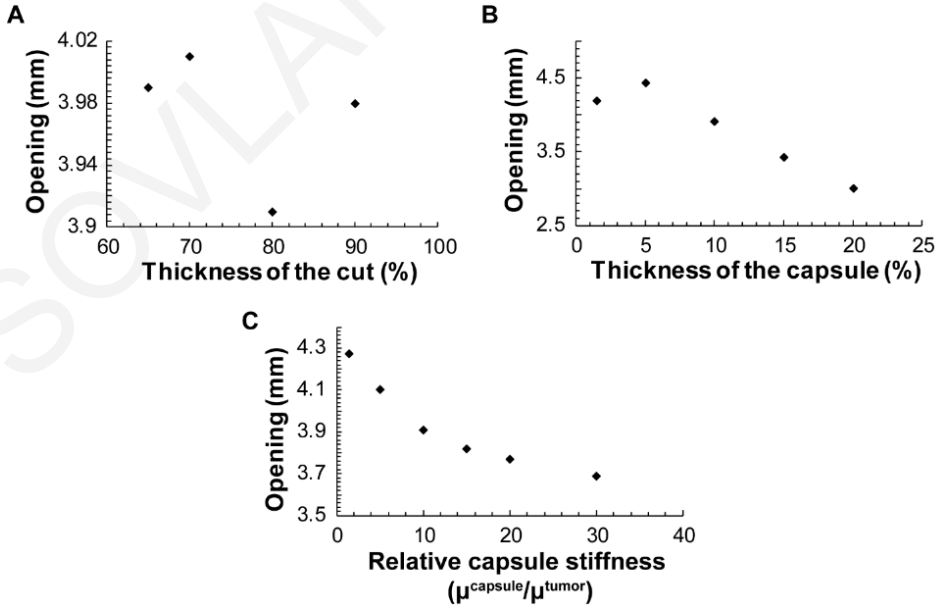

Fig. *5-10*. Results of the parametric analysis of the computational model. The plots show tumor opening calculations as a function of (A) thickness of the cut (percent to

tumor diameter), (B) thickness of the capsule (percentage of tumor diameter) and (C) capsule stiffness (ratio of capsule shear modulus to tumor shear modulus).

5.4 Discussion

Despite the crucial role that mechanical forces play in tumor growth and therapy, the study of the biomechanical behavior of solid tumors remains a relatively unexplored area of research as least compared to the biomechanics of other connective tissues, such as blood vessel, heart, tendons and articular cartilage [8,13]. The existence of growth-induced/residual stress in solid tumors was suspected for more than two decades but it was not until 2012 that we systematically studied its causes, consequences and remedies [2,6]. Furthermore, we and co-workers employed this simple tumor opening experiment as a technique to test the ability of common drugs to alleviate mechanical forces in tumors in order to improve the delivery of chemotherapy and nanomedicines by decompressing tumor blood vessels. Such drugs include: losartan (Cozaar®, Merck Pharmaceuticals) a common anti-hypertensive drug, pirfenidone (Esbriet®, Roche) approved for the treatment of idiopathic pulmonary fibrosis and tranilast (Rizaben®, Kissei Pharmaceuticals) approved in Japan and South Korea as an anti-allergic and anti-fibrotic drug[10,32,37,113,114]. Regarding the swelling behavior of tumors, it was only recently that the swelling of cancer cells in response to compressive stresses and the hyaluronan-derived swelling of tumors was systematically studied[9,10].

6 Chapter 6: Stress alleviation strategy in cancer treatment: Insights from a mathematical model.

This research is under review in ZAMM journal: Mpekris F.*, C. Voutouri*, P. Papageorgis and T. Stylianopoulos. Stress alleviation strategy in cancer treatment: Insights from a mathematical model. ZAMM * Equal contribution.

6.1 Introduction

Based on the knowledge acquired from the constitutive modeling of solid tumors (Chapter 2), the experiments to alleviate mechanical stresses (Chapter 3), and to measure swelling (Chapter 4) and residual stress (Chapter 5), in this chapter we developed a mathematical model including all these in a unified modeling framework. We used the experimental data from Chapter 3 to specify the model and present model predictions for the stress alleviation treatment.

Solid stresses are the stresses of the solid phase of a tumor and can be divided to three types: i) externally applied stress by the host tissue to the tumor due to mechanical interactions between the two tissues [6-8], ii) growth-induced or residual stress which are the stresses that remain in the tumor when it is excised, and external loads are removed [2], and iii) swelling stress, which is developed owing to the negatively charged hyaluronan chains that exert repulsive electrostatic forces on each other as they are closely packed in the dense tumor extracellular matrix, causing tissue swelling [9,10].

The stresses of the fluid phase of tumors mainly consist of the hydrostatic fluid pressure of the tumor interstitial space as well as the vascular pressure and the fluid shear on the luminal side of the tumor blood vessel wall [11-13]. Within tumor interior, the interstitial fluid pressure (IFP) is uniformly elevated owing to the hyper-permeability (i.e., leakiness) of the tumor blood vessels and can be as high as the vascular pressure [11,13].

Solid stresses affect cancer cell growth both directly, by compressing cancer cells, or indirectly by compressing blood and lymphatic vessels. Depending on its levels, compression of cancer cells could either induce apoptosis or increase their proliferation rate and upsurge their invasive and metastatic potential [8,20-22,24,25]. On the other hand,

compression of blood vessels results in hypoxia and hypo-perfusion [6,8,10,26,27]. In turn, hypoxia provides a survival advantage for cancer cells, enhances their ability to invade and metastasize, maintains the cancer stem cell population and compromises the efficacy of radiotherapy [28,77]. Furthermore, hypo-perfusion drastically reduces the systemic delivery of drugs to the tumor site and consequently, the efficacy of chemo- and nanotherapeutics [29]. As far as the elevation of the IFP is concerned, it can eliminate pressure gradients across the tumor vessel wall and thus, hinder the transvascular transport of macromolecules and nanomedicines [14], rendering it a major barrier for drug delivery [13,30,61,74,93,102].

Recent studies have shown that normalization of the tumor microenvironment by targeting specific components of the ECM, such as collagen and/or hyaluronan can reduce mechanical stresses, decompress tumor blood and lymphatic vessels and improve perfusion [10,35,36,77,122]. Therefore, pharmacological depletion of collagen and/or hyaluronan by repurposing approved anti-fibrotic agents can increase drug delivery and improve therapeutic outcomes. More specifically, repurposing of the anti-fibrotic drug tranilast (Rizaben®, Kissei pharmaceuticals), pirfenidone (Esbriet®, Roche) - approved for the treatment of idiopathic pulmonary fibrosis – and the angiotensin receptor blocker losartan (Cozaar®, Merck & Co) has shown to improve the delivery of therapeutics by inducing blood vessel decompression and improving perfusion in a variety of breast and pancreatic tumor mouse models [32,37,113,114].

In this Chapter, we show both mathematically and experimentally that stress alleviation strategy increases functional vascular density by decompressing blood vessels and improving drug delivery. We developed a mathematical model based on our previous studies [6,7,10,38,120,121], in which we accounted for the reduction in elastic modulus, hydraulic conductivity and tumor swelling stress owing to depletion of collagen and hyaluronan [10] using published experimental data [113]. Subsequently, we performed in vivo experiments in mice bearing breast tumors to validate the model predictions of the stress alleviation strategy. Finally, using the mathematical model we predicted the combined effect of stress alleviation and reduction in vessel wall leakiness – to model vascular normalization - on drug delivery.

6.2 Material and methods

Cell culture, Drugs, animal tumor models and experimental protocols detailed description given in (chapter 3).

6.2.1 Mathematical model description

Vascular density

To evaluate the tumor vascular density, we considered that it is affected independently both by solid stress and tumor-induced angiogenesis. Assuming that solid stress does not influence the number or length of vessels, but only their diameter, the change in vascular density because of vessel compression was expressed as

$$S_V(\bar{\sigma}) = (d/d_0)\, S_{V0}, \qquad (6.1)$$

where S_{V0} and d_0 are the vascular density and vessel diameter values when no compression is applied. The dependence of the ratio d/d_0 on solid stress was determined in previous work [120].

Oxygen Transport

The rate of change of oxygen in tissues depends on the amount that enters the tissue from the blood vessels, its transport through convection and diffusion, minus the amount of oxygen consumed by cells [41,49] i.e.,

$$\frac{\partial c_{ox}}{\partial t} + \nabla \cdot \left(c_{ox} \mathbf{v}^f \right) = D\nabla^2 c_{ox} - \frac{A_{ox} c_{ox}}{c_{ox} + k_{ox}} S_f \varphi^C + P_{er} S_V \left(C_{iox} - c_{ox} \right) \qquad (6.2)$$

where c_{ox} is the oxygen concentration, D is the diffusion coefficient of oxygen in the interstitial space, A_{ox} and k_{ox} are oxygen uptake parameters, P_{er} is the vascular permeability of oxygen that describes diffusion across the tumor vessel wall and C_{iox} is the oxygen concentration in the vessels.

Drug transport

We assumed that chemotherapy influences the growth of the tumor by killing cancer cells but has no effect on endothelial cells and the tumor vascular density. The chemotherapeutic agent can exist in three distinct states: travel free in the tumor interstitial space (c_f), bind to

cancer cells (c_b), and get internalized by cells (c_{int}). Hence, drug transport in the interstitial space was expressed as [29]

$$\frac{\partial c_f}{\partial t} + \nabla \cdot \left(c_f \mathbf{v}^f \right) = D_f \nabla^2 c_f + Q_{sta} - \frac{k_{on} c_e c_f}{\varphi} + k_{off} c_b ,$$

$$\frac{\partial c_b}{\partial t} + \nabla \cdot \left(c_b \mathbf{v}^s \right) = \frac{k_{on} c_e c_f}{\varphi} - k_{off} c_b - k_{int} c_{int} , \qquad (6.3)$$

$$\frac{\partial c_{int}}{\partial t} + \nabla \cdot \left(c_{int} \mathbf{v}^s \right) = k_{int} c_b ,$$

where D_f is the diffusion coefficient of the drug in the tumor interstitial space, c_e is the concentration of cell surface receptors, k_{on}, k_{off} and k_{int} are the association (binding), dissociation and internalization rate constants of the drug with the cells, respectively, and φ is the volume fraction of tumor accessible to the drug. The term Q_{sta} on the right hand side of Eq. *(6.3)* denotes the transport of the drug across the tumor vessel wall and is given by Starling's approximation as [29]

$$Q_{sta} = P_{er} S_V \left(C_{iv} - c_f \right) + L_p S_V \left(P_V - p_i \right) \left(1 - \sigma_f \right) C_{iv} \qquad (6.4)$$

where L_p is the hydraulic conductivity of the vessel wall, $C_{iv} = \exp(-(t-t_0)/k_d)$ is the vascular concentration of the drug, describing a bolus injection, with t_0 the time of drug injection, k_d the blood circulation decay, and σ_f is the reflection coefficient. The parameter L_p was calculated as a function of the vessel wall pore radius and the parameters P_{er} and σ_f as a function of the ratio of the drug radius to the radius of the pores of the vessel wall [120,123,124].

6.2.2 Implementation of biphasic theory for soft biological tissues

The biphasic theory for soft tissues where applicable to this chapter, is the same as the triphasic theory, detailed description in Chapter 4. The different in the biphasic theory is that not included ions (c^f and c^k) concentration.

According to the biphasic theory for soft tissues [80], the total stress tensor $\boldsymbol{\sigma}_{tot}$ is the sum of the fluid phase stress tensor $\boldsymbol{\sigma}^f = -p_i \mathbf{I}$ of the interstitial fluid pressure p_i, the

solid phase stress tensor $\boldsymbol{\sigma}^s$ and swelling stress, $\boldsymbol{\sigma}^w$ owing to tumor swelling. As a result, the stress balance is written as

$$\nabla \cdot \boldsymbol{\sigma}_{tot} = \mathbf{0} \Rightarrow \nabla \cdot \left(\boldsymbol{\sigma}^s - p_i \mathbf{I} - \boldsymbol{\sigma}^w \right) = \mathbf{0}, \tag{6.5}$$

where the Cauchy stress tensor of the solid phase $\boldsymbol{\sigma}^s$ is given by [55]

$$\boldsymbol{\sigma}^s = J_e^{-1} \mathbf{F}_e \frac{\partial W}{\partial \mathbf{F}_e^T}. \tag{6.6}$$

where W is the strain energy density function and J_e is the determinant of the elastic deformation gradient tensor $\mathbf{F}_e$.

The tumor mechanical behaviour was modelled to be nearly-incompressible and described by the modified neo-Hookean strain energy density function [7,43,52,125]:

$$W = \frac{1}{2} \mu \left(-3 + II_1 \right) - p \left(J_e - 1 \right) - \frac{p^2}{2k}, \tag{6.7}$$

where μ and k are the shear and bulk modulus of the material, respectively, $II_1 = I_1 J_e^{-2/3}$, where $I_1 = \mathrm{tr}\mathbf{C}_e$ is the first invariant of the elastic Cauchy-Green deformation tensor $\mathbf{C}_e = \mathbf{F}_e^{\mathrm{T}} \mathbf{F}_e$, p is a Lagrange multiplier enforcing the material constraint of incompressibility and the third term on the right hand side of Eq. (7) is a penalty term introduced for nearly incompressible materials that regularizes the constraint involved in the second term. The surrounding normal tissue was assumed to be compressible and neo-Hookean with a Poisson ratio of 0.2. The values of the parameters μ and k were determined from in vivo experiments for control and tranilast-treated tumors [113] and are presented in Table 1.

The swelling stress, $\boldsymbol{\sigma}^w$ was calculated from the ratio of hyaluronan to collagen area fraction based on immunofluorescence staining images from the empirical linear equation [10]:

$$\boldsymbol{\sigma}^w = 4.089(\mathrm{HA/Coll}) - 2.0569, \tag{6.8}$$

where the area fraction of hyaluronan (HA) and collagen (Coll) were taken from our previously published in-vivo experiments with control or tranilast-treated tumors [113].

The term S^c in the right hand side of Eq.*(4.5)* describes the creation and degradation of solid phase and is given by:

$$S^c = G\left(1+\beta\bar{\sigma}\right)S_f\varphi^c\left(1-\varphi^c\right) \qquad (6.9)$$

To account for the effect of drug delivery on growth, the fraction of survived cells S_f is included in Eq. *(6.9)*, so that in the absence of drugs S_f equals unity. The fraction of survived cells with respect to drug concentration has been previously measured experimentally for doxorubicin [126], and the results were fitted to an exponential expression as a function of the internalized chemotherapy concentration c_{int}, i.e.,

$$S_f = \exp(-\omega c_{int}), \qquad (6.10)$$

where ω is a fitting parameter defined in [53].

6.2.3 Multiplicative decomposition of the deformation gradient tensor

A detailed description of the multiplicative decomposition is given in (4.3.1). Specifically, in this chapter the tensor, **F**, is decomposed into two independent motions: the growth of the tumor, $\mathbf{F}_g$, and the elastic mechanical interactions, $\mathbf{F}_e$, the component that accounts for the generation of residual stresses $\mathbf{F}_r$ equal **I**.

6.2.4 Solution methodology

Eqs. *(6.1)-(6.10)* were solved simultaneously using the commercial finite element software COMSOL Multiphysics (COMSOL, Inc., Burlington, MA, USA). To this end, the model comprises of a spherical tumor domain with initial diameter of 500 μm, installed at the focal point of a cubic host domain, because of symmetry only one eighth of the system was considered (**Fig. *6-1***). Values of the model parameters are given in Table 3. The boundary conditions employed are illustrated in **Fig. *6-1***. The boundary conditions for the continuity of the stress and displacement fields, as well as the concentration of the oxygen and the drug at the interface between the tumor and the normal tissue were applied automatically by the software.

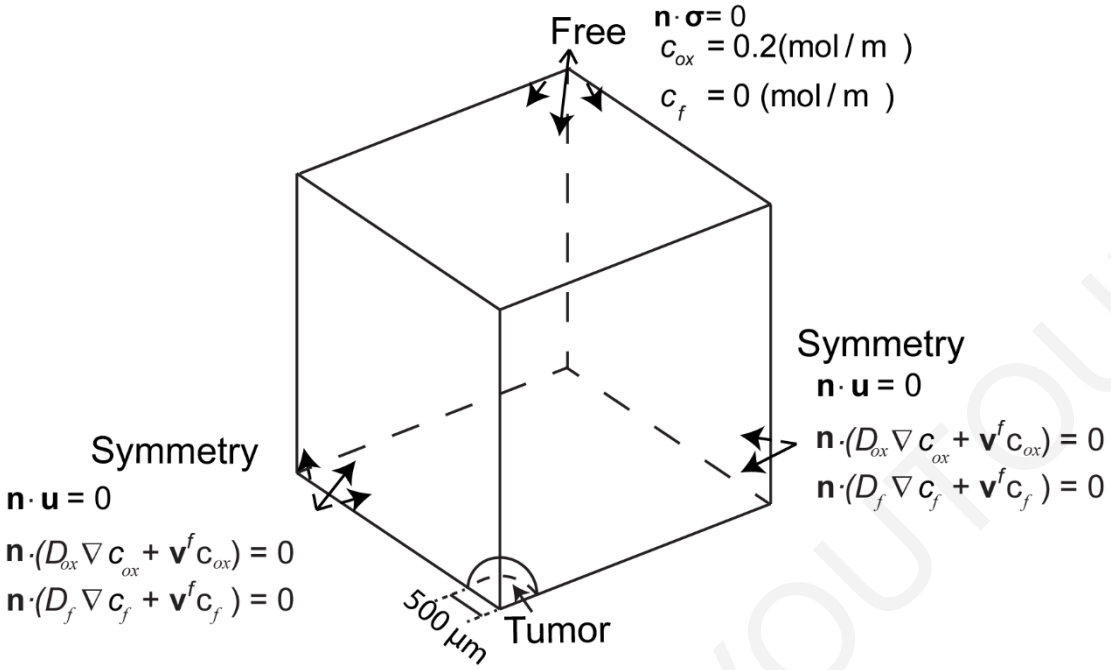

Fig. *6-1*. Computational domain and boundary conditions employed.

Table 3**. Parameter values used in the model.**

Parameter	Description	Value	Reference
v	Poisson ratio	0.2 [-] for host tissue; 0.45 [-] for tumor	[7]
β	growth stress dependence	0.000025 Pa^{-1}	[7]
μ	shear modulus	22.4 kPa for control treated for tumor; 5 kPa for control treated for host tissue; 8.5 kPa for tranilast treated for tumor; 8.9 kPa for tranilast treated for host tissue;	[113]

k	bulk moduls	216.5 kPa for control treated for tumor; 6.67 kPa for control treated for host tissue; 82.17 kPa for tranilast treated for tumor; 8.9 kPa for tranilast treated for host tissue;	[113]
k_{th}	the hydraulic conductivity of the interstitial space	2×10^{-7} $cm^2/(mmHg\cdot s)$ for control treated. 1.2×10^{-6} $cm^2/(mmHg\cdot s)$ for tranilast treated;	[113]
S_{V0}	initial functional vascular density	70 cm^{-1}	[127]
C_{iox}	initial oxygen concentration	0.2 $mol\cdot m^{-3}$	[91]
D_{ox}	oxygen diffusion coefficient	1.55×10^{-4} $m^2\cdot day^{-1}$	[49]
A_{ox}	oxygen uptake	2,200 $mol\cdot m^{-3}\cdot day^{-1}$	[49,91]
k_{ox}	oxygen uptake	0.00464 $mol\cdot m^{-3}$	[49,91]
k_1	growth rate parameter	2.13 day^{-1}	---
k_2	growth rate parameter	0.0083 $mol\cdot m^{-3}$	[91]
c_e	receptor concentration	0.01 $mol\cdot m^{-3}$	[128,129]

φ	volume fraction of tumor accessible to drug	0.3 [-]	[128,129]
k_{on}	binding rate	1.296×10^6 $m^3 \cdot mol^{-1} \cdot day^{-1}$	[128,129]
k_{off}	dissociation rate	691.2 day^{-1}	[128,129]
k_{int}	internalization rate	3.7 day^{-1}	[128,129]
D_f	drug diffusion coefficient	8.64×10^{-6} $m^2 \cdot day^{-1}$	[130]
ω	cell survival constant	0.6603 m^3/mol	[53]
k_d	blood circulation decay	0.417 day^{-1}	[74]

6.3 **Results**

6.3.1 Mathematical modelling of tranilast-induced stress alleviation

In a previous study, we showed that tranilast reduces mechanical stresses, decreases interstitial fluid pressure, improves tumor perfusion and significantly enhances the efficacy of different-sized drugs, by suppressing transforming growth factor-β (TGFβ) signalling and expression of extracellular matrix components [113]. In this study, we modelled the alterations in mechanical parameters affecting tumor growth to validate the experimental measurements. First, using the data of the increase in hydraulic conductivity, i.e. the ease by which interstitial fluid percolates through the interstitial tumor space, observed experimentally in tranilast-treated compared to control-treated tumors [113,131], we employed our mathematical model to calculate IFP and compare our results with the experimentally measured IFP values. Our model predictions were in very good agreement with the experimental data (**Fig. *6-2***A) [113]. To study changes in solid stress, we accounted for the decrease in the elastic modulus in tranilast-treated tumors versus the control group in [113]. Additionally, to calculate the solid stress of the tumor, we

considered changes in tumor swelling stress, which is determined by collagen and hyaluronan content, as measured experimentally [10,113]. A decrease in the elastic modulus and swelling stress resulted in reduction of intratumoral solid stresses (**Fig. *6-2***B). Conclusively, our model verified that changes in mechanical properties of the tumor results in alleviation of solid and fluid stresses.

In a previous study [120], we have shown that heterogeneous distribution of solid stress results in heterogeneous compression of blood vessels and, thus, heterogeneous vascular density inside the tumor. Alleviation of tumor solid stress by tranilast treatment caused an increase in functional vascular density (**Fig. *6-2***C) due to decompression of tumor vessels. The large amount of compressed vessels in the tumor often renders its interior hypo-perfused, which, in turn, can decrease dramatically drug delivery and compromise therapeutic outcomes [13,68]. Improvement of functional vascular density enhanced drug delivery and increased internalized drug concentration (**Fig. *6-2***D). These observations are in accordance with our previous experimental results [113].

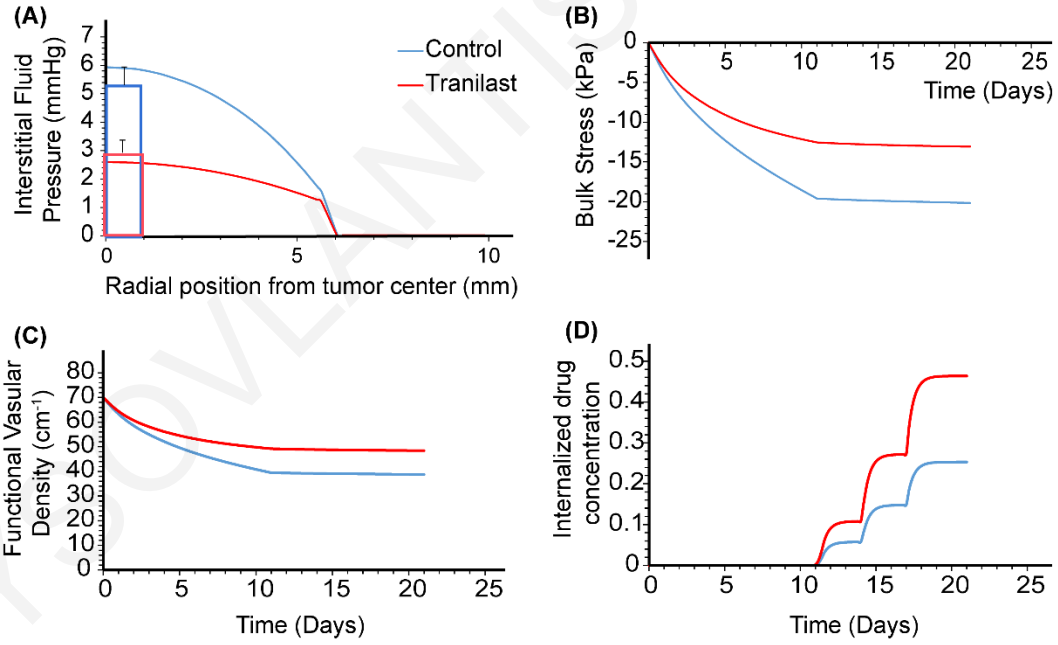

Fig. *6-2*. Mathematical model validates tranilast-induced stress alleviation strategy. (A) Experimentally observed increase in hydraulic conductivity reported in [113] results in decrease in IFP using the mathematical model. Our model predictions are in good agreement with our previous experimental data [35], presented with bars at the center of tumor. (B) Reduction of bulk stress, $\bar{\sigma} = \mathrm{tr}\boldsymbol{\sigma}^s/3 = (\sigma_{rr} + \sigma_{\theta\theta} + \sigma_{\varphi\varphi})/3$, due to decrease in

elastic modulus and swelling stresses in tranilast-treated tumors according to experimental data. (C) Alleviation of solid stress improves functional vascular density and (D) cancer cell drug uptake (drug administration started on day 11 and it was repeated every 3 days, following experimental protocol) via decompression of tumor blood vessels.

6.3.2 Mathematical modelling validates the improved efficacy of chemotherapy using tranilast

As described above, our mathematical model predicts increased functional vascular density and internalized drug concentration. To further validate our model's predictions, we performed *in vivo* experiments to evaluate whether tranilast improves the efficacy of chemotherapy *via* stress alleviation. We developed an orthotopic syngeneic mouse model using the 4T1 breast cancer cell line and employed doxorubicin as the chemotherapeutic drug. Mice received orally mock treatment or tranilast (200mg/kg) from 4 days post-implantation of cancer cells in the mammary fat pad, whereas doxorubicin administration begun on day 11. We found that tranilast alone or doxorubicin alone did not influence primary tumor growth (**Fig. *6-3***). However, combinatorial treatment using tranilast and doxorubicin significantly delayed tumor growth (**Fig. *6-3***). To validate the mathematical model, we compared the model to our experiments varying only one model parameter, $k_{1,}$ which describes the dependence of tumor proliferation on oxygen concentration (Table 1). The value of k_1 was assigned to match model predictions with the final tumor volume reported in the experimental data. The values of tumor volume predicted *via* mathematical modelling were in a good agreement with the experimental data, since tranilast or chemotherapy alone did not result in significant differences compared to control-treated group. On the other hand, the overall tumor volume decreased for the combinatorial treatment. Our model verifies that combining chemotherapy with drug-induced changes in tumor mechanical properties, synergistically inhibits tumor growth.

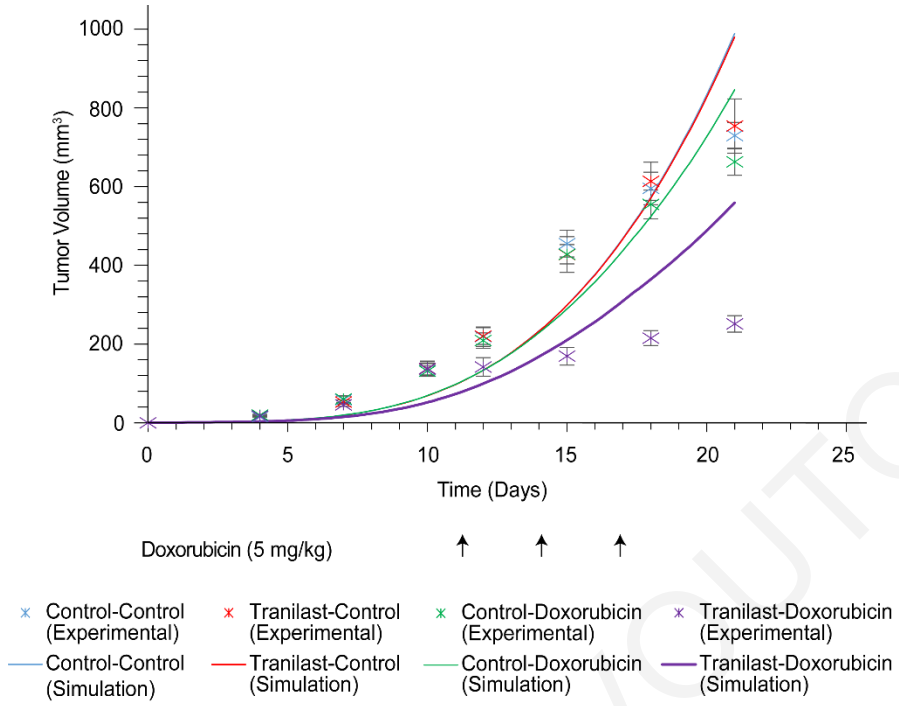

Fig. *6-3.* Tranilast increases anti-tumor efficacy of chemotherapy both mathematically and experimentally. Tumor volume growth rates of orthotopic murine breast cancer cells implanted in BALB/c mice (dots) and mathematical model predictions (lines). The control treatments ($NaHCO_3$ or saline, respectively) as well as tranilast or doxorubicin alone had no effect on tumor growth in both cases. Combination of tranilast (200mg/kg) and doxorubicin (5mg/kg) significantly delayed tumor growth of 4T1 breast tumors compared to doxorubicin monotherapy (p = 1E-10 on day 21, n = 6-8). Mathematical model confirms that combination of changes in mechanical properties of tumor and chemotherapy treatment inhibits tumor growth.

6.3.3 Vascular normalization improves drug delivery

Another mechanism to improve perfusion and delivery of therapeutic agents is vascular normalization, which aims to decrease leakiness of the hyper-permeable tumors and normalize the structure of the vascular network [77]. Vascular normalization fortifies the tumor vasculature by increasing pericyte coverage of blood vessels and decreasing the size of vessel wall pores, which results in decreased vessel leakiness. Here, to model vascular normalization, we considered only changes in vessel wall pore size. We performed a parametric analysis varying the radius of vessel wall pores from 70nm to 110nm based on

pertinent experimental studies [5]. We found that reducing vessel pore size resulted in increased functional vascular density and decreased IFP (**Fig. *6-4***A). Therefore, the pressure difference across the vessel wall can be restored which, in turn, can enhance the transport of drugs through the vessel wall and the (internalized) drug concentration that is taken up by cancer cells (**Fig. *6-4***B). These observations are consistent with previous studies [72,74,124,132]. Importantly, our model predictions suggest that stress alleviation and vascular normalization strategies can be combined to further increase the drug concentration that is taken up by cancer cells (**Fig. *6-4***C).

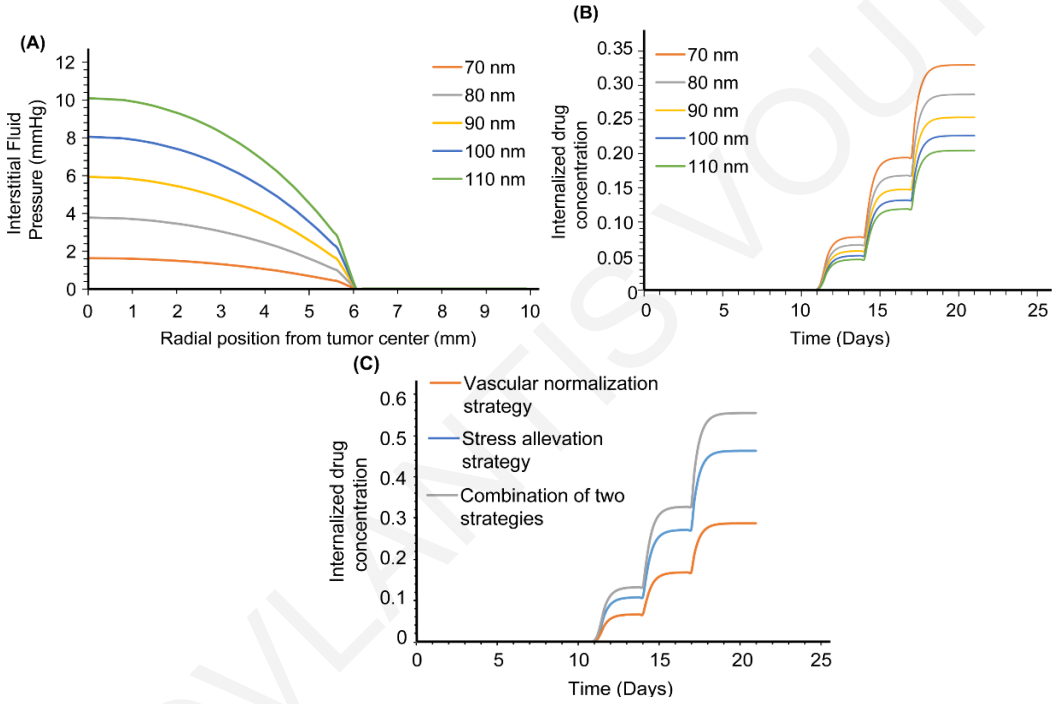

Fig. *6-4*. Model predictions for vascular normalization strategy *via* decrease in vessel wall pore size. (A) Lowering the size of vessel wall pores decreases IFP and (B) increases internalized drug concentration. (C) Combination of stress alleviation and vascular normalization strategies further improves drug delivery.

6.4 **Discussion**

Abnormalities in tumor microenvironment prevent efficient drug delivery and compromise therapeutic outcomes. To enhance treatment efficacy, stress alleviation and vascular normalization strategies have been recently developed towards this goal [29,77]. In this study, we developed a mathematical model to study stress alleviation based on our

previously published experimental data [113]. We accounted for the variations in hydraulic conductivity, elastic modulus and tumor swelling caused by alterations in extracellular matrix components that are modulated using anti-fibrotic drugs to induce stress alleviation. Our model predicted a reduction in IFP during stress alleviation, which is quantitavely similar to our previous experimental measurements. Furthermore, this model was employed to assess the solid stress of tumors and verify that solid stress was reduced in the presence of stress alleviating drugs. Alleviation of solid stress increased functional vascular density, enhanced drug delivery and improved therapeutic outcomes. To further validate our model, we carried out new experiments in mice bearing breast tumors using tranilast to alleviate mechanical stresses. We showed that while tranilast or chemotherapy alone had no effect on overall tumor volume, combinatorial treatment with tranilast and chemotherapy delayed significantly tumor growth.

As it has been shown previously [2,32,113,114], treatment with stress alleviating agents has the ability to reopen compressed blood vessels and, thus, improve perfusion and drug delivery in hypo-perfused tumors. Our mathematical model simulated the experimental procedure of stress alleviation strategy and verified that changes in mechanical properties of the tumor and alterations in tumor components, such as collagen or hyaluronan, results in alleviation of solid and fluid stresses. Furthermore, the model enables us to calculate parameters such as the total tissue stress, which are difficult to be measured experimentally. On the other hand, our model is subject to certain limitations since we did not account for biological parameters affecting tumor progression, such as the role of vascular endothelial growth factor (VEGF) on tumor-induced angiogenesis or changes in gene expression, which could alter the mechanical properties of the tissue during growth. However, we expect that incorporation of these parameters would not change our results qualitatively.

7 Chapter 7: Mechanisms of non-angiogenic tumor growth in brain tumors following anti-angiogenic treatment.

This is a collaborative research with the research group of Professor Rakesh K. Jain at Harvard Medical School: C. Voutouri, N. D. Kirkpatrick, Chung E., Baish J. W., Fukumura D., Stylianopoulos T., Jain R. K. Mechanisms of non-angiogenic tumor growth in brain tumors following anti-angiogenic treatment. In preparation.

7.1 **Introduction**

Adequate oxygen and nutrients supply are crucial for cancer cell survival and proliferation, as mentioned above. As that the role of blood vessels in tumor growth has been a subject of intense study, with the pioneering work of Judah Folkman to shape the field for many years, suggesting that tumor progression must be preceded by an angiogenic response [133]. According to this notion, avascular cancer cell proliferation leads to hypoxia and initiation of hypoxia-induced angiogenesis, guided by increased expression of pro-angiogenic factors [134,135]. As a consequence, anti-angiogenic treatments to prune the tumor vasculature have been proposed and tested in a plethora of preclinical and clinical studies with various degrees of success [73,108]. To complement the angiogenic growth of tumors, it is now accepted that some solid tumors can grow in a non-angiogenic fashion by exploiting the pre-existing, host vasculature in a process that is termed vessel co-option. Non-angiogenic tumors have been reported in brain, lung, liver, and skin in both mouse tumor models and humans [136-138]. In this case, cancer cells co-opt existing host vessels to maintain oxygen supply. It is also possible, however, that the co-opted vessels become dysfunctional, creating hypoxia and leading to robust hypoxia-induced angiogenesis [135,139-141]. Cancer cells can also co-opt blood vessels when they extravasate to the metastatic site to form a metastatic lesion.

Interestingly, vessel co-option has been related to resistance to anti-angiogenic treatment and anti-vascular endothelial growth factor (VEGF) therapies using monoclonal antibodies or multitargeted tyrosine kinase inhibitors (TKIs) have shown modest efficacy in recurrent glioblastoma multiforme (rGBM). Specifically, in some orthotopic murine models, increased survival with these agents could primarily be attributed to a reduction in edema

rather than any direct anti-tumor effect [142]. Furthermore, studies have suggested that gliomas may respond to anti-angiogenic therapy with an increased invasive phenotype although direct evidence has not yet been established [143,144]. It has also been shown that anti-angiogenic treatment can support and maintain vessel co-option, acting as a compensatory strategy for cancer cells to maintain blood supply and thus, evade anti-angiogenic therapy [145-147]. To support that, it is now accepted that glioblastoma invasion to the brain can be achieved not only by cell migration along the brain's fiber tracks but also by co-opting brain blood vessels [148]. Based on these findings, it has been postulated that vessel co-option is a mechanism of tumor resistance to anti-angiogenic treatment.

Given the important role of non-angiogenic tumor growth and because non-angiogenic tumors do not follow the classical hypoxia-induced angiogenic pathways, two of the main questions as far as their biology is concerned is how do cancer cells interact with the host vasculature to co-opt existing vessels and how vessel co-option resists to anti-angiogenic treatment. Despite the intense research in the field, a mechanistic understanding of these processes is still incomplete [149].

To this end, we used intravital multiphoton laser scanning microscopy (MPLSM, [150]) and two orthotopic invasive glioma models (CNS-1 and GL261) to study the kinetics of vessel co-option and test the invasive tumor response of glioblastoma cells to the anti-angiogenic agent, cediranib. Using *in vivo* dynamics, we were able to directly probe tumor cell migration into the normal brain and correlate these invaded regions to structural and molecular markers of the brain parenchyma. In addition, we employed a brain metastasis model from MDA-231BR breast cancer cells to provide evidence that metastatic cells co-opt the brain vasculature and that co-option causes blood vessel compression. Furthermore, in order to provide insights into the mechanisms involved in vessel co-option and resistance to anti-VEGF therapy, a new mathematical model for vessel co-option and tumor growth was developed, connecting events that take place at the microscopic cellular/subcellular level of cancer and endothelial cells with the macroscopic tumor behavior.

In this study, we focused on the development of a new mathematical model to study the mechanisms of angiogenic and non-angiogenic tumor growth in brain tumors. The group of Professor Rakesh K. Jain at Harvard Medical School and Massachusetts General Hospital provided us with the experimental data to validate the model. Specifically, in the model, cancer cells migrate towards better oxygenated intratumoral regions, co-opting and

eventually compressing blood vessels. Blood vessel compression results in reduced vessel functionality and hypoxia, which in turn triggers the production of angiopoietins 1 and 2 (Ang1 and Ang2) by tumor endothelial cells as well as production of VEGF by cancer cells and stroma cell-derived factor 1 alpha (SDF1α) by both cancer and endothelial cells. Ang1 stabilizes endothelial cells, whereas Ang2 destabilizes them increasing their migration potential. Endothelial cell migration inside and outside the tumor is co-ordinated by VEGF and SDF1α gradients giving rise to angiogenesis. Based on the concentration of endothelial cells (both stable and unstable), a functional tumor blood vessel density is calculated for use at the macroscopic scale to predict tumor growth. The processes involved at each level and their interactions are summarized in **Fig. *7-1***. Model predictions were compared and validated against a large number of independent experimental data – including our experiments - for the different stages of tumor growth and provided a mechanistic understanding of the experimental observations.

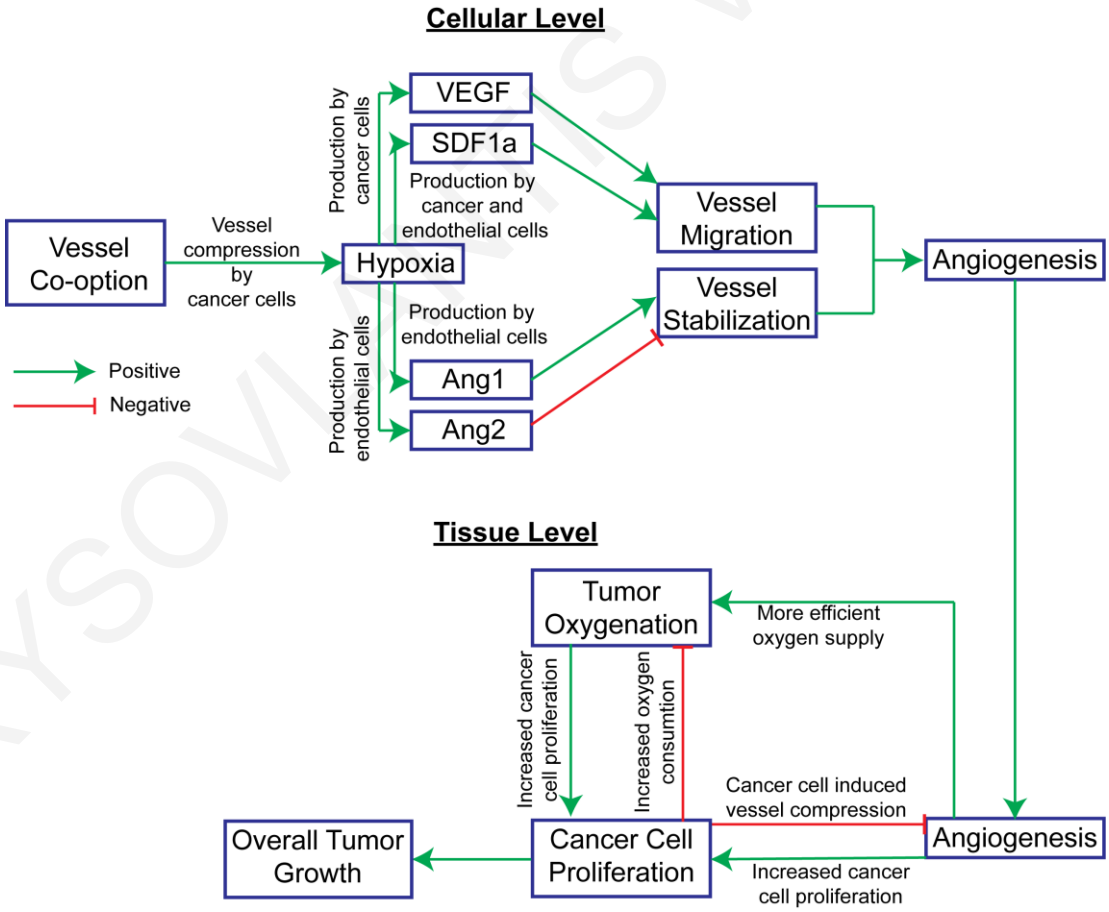

Fig. *7-1.* Schematic of components comprising the mathematical model and their interactions. The model consists of the cellular and the tissue level. At the cellular level, cancer cells are moving towards the more oxygenated regions of the tumor, co-opting blood vessels. Cancer cell attachment to blood vessels causes vessel compression and hypoxia, which drives a secondary angiogenic response owing to Ang1, Ang2, VEGF and SDF1α that causes the migration of stable and unstable endothelial cells. From endothelial cell migration, a tissue level functional vascular density is calculated that determines macroscopic oxygen transport, cancer cell proliferation and overall tumor growth.

7.2 **Methods**

7.2.1 Intravital imaging of glioblastomas

CNS-1 (rat glioma) and GL261 (mouse glioma) were obtained from Dr. William F. Hickey (Dartmouth Medical School) and National Cancer Institute, Repository, respectively and were cultured according to previous studies [151,152]. Both cell lines were transfected with DsRed fluorescent protein, sorted for 100% expression, and were maintained in culture as neurospheres. Using mice with surgically implanted cranial windows [1,153], we injected 10,000 tumor cells into the cerebrum of 8-12 week old male NOD/SCID (CNS-1 cells/xenograft) or 8-12 week old male C57/BL6 (GL261/syngeneic) mice. The tumor cells were imaged within the first week after implantation with a custom built multiphoton microscope. Mice were injected intravenously with FITC Dextran (80 kDa), and an excitation wavelength of 840 nm was used to simultaneously excite FITC and dsRed. Mice were imaged every 1 to 2 days and locations tracked via vessel landmarks. When tumors had established a primary lesion as determined by intravital microscopy (typically 2 to 3 weeks), we treated animals with 6 mg/kg cediranib (daily oral gavage) with control groups treated with the corresponding drug vehicle. Tumor cell dynamics relative to brain microvessels were measured with multiphoton microscopy. Following treatment and imaging, brain sections were assessed with immunofluorescence of tumor cells dsRed combined with CD31 staining.

7.2.2 Brain metastasis model from breast cancer cells

MDA-231BR cells were obtained from Dr. Patricia S. Steeg, National Cancer Institute. To form the brain metastasis model, a suspension of (0.25 million/0.1ml PBS) MDA-231BR cells transfected with green fluorescence protein (GFP) were transferred by intracardiac injection to the circulation of female nude mice that carried a cranial window. Mice were imaged every 3 days and locations were tracked via vessel landmarks. Transfection of cancer cells with GFP, immunofluorescence staining for cell nuclei (DAPI) and for functional blood vessels (biotynilated lectin) as well as Hematoxylin and Eosin (H&E) staining were performed according to previous studies [103,154].

All animal procedures were carried out following the Public Health Service Policy on Humane Care of Laboratory Animals and were approved by the Institutional Animal Care and Use Committee of Massachusetts General Hospital. All cell lines were repeatedly tested negative for mycoplasma using the Mycoalert Plus Mycoplasma Detection Kit (Lonza), authenticated before use by IDEXX laboratories.

7.2.3 Description of mathematical model

Several proteins and other molecules have been shown to coordinate alterations in the host and tumor vasculature including Ang1 and Ang2, VEGF and SDF1α. The common basis of all these proteins is that they are over-produced under hypoxic conditions. Ang1 and Ang2 are mainly produced by endothelial cells and act in an autocrine fashion: Ang1 has been shown to stabilize endothelial cells leading to mature vessels, while Ang2 has the opposite effect, destabilizing endothelial cells causing angiogenesis [135,139,149,155]. VEGF and SDF1a are mainly produced by tumor cells and co-ordinate endothelial cell migration and angiogenesis [140,155,156]. It has been further suggested that vessel co-option firstly induces high autocrine expression of Ang2 that initiates endothelial cell migration and at a second stage, the formation of VEGF gradients guides the angiogenic procedure [139,157]. Interestingly, this could imply that even in the absence of VEGF gradients, angiogenesis can still exist, but it would not be directed to high VEGF concentrations.

In the literature, most pertinent mathematical models focus on VEGF-induced angiogenesis with only a few accounting for vessel co-option and these models do not relate explicitly the effect of co-option on tumor growth [158-163]. Our mathematical framework for tumor

growth accounts both for vessel co-option and VEGF-induced angiogenesis and couples events at both cellular and tissue scales (**Fig. *7-1***).

Cellular level: cancer cells move towards high oxygen levels (blood vessels) causing vessel co-option and compression. Vessel compression reduces oxygenation and creates hypoxia and production of VEGF, SDF1α, Ang1, and Ang2. Ang1 stabilizes endothelial cells, whereas Ang2 destabilizes them. VEGF and SDF1α gradients drive endothelial cell migration and angiogenesis.

Cancer cell proliferation depends on oxygen concentration through a Michaelis-Menten kinetics equation, while cancer cell movement is described by the diffusion equation as a function of the cancer cell, oxygen and SDF1α gradients[164].

Two populations of endothelial cells are considered, stable and unstable. Production rates of both types of endothelial cells depend on VEGF and SDF1α (chemotactic term) concentrations as well as on their concentrations. Endothelial cells migration is assumed to be diffusive and depend on endothelial cells, VEGF and SDF1α gradients [164].

VEGF concentration is determined by diffusion, production from cancer cells under hypoxic conditions and binding to endothelial cells [164].

SDF1α is also known as C-X-C motif chemokine 12 (CXCL12). We suggest in the model that VEGF released by hypoxic cancer cells up-regulates SDF1α from cancer cells and that SDF1α is also produced by endothelial cells also in a VEGF dependent manner.

Ang1 and Ang2 are assumed to be produced by unstable and stable endothelial cells, respectively. Their production is enhanced by hypoxia based on VEGF levels [165].

Tissue level: The tumor is assumed to be composed of a solid phase containing all cell types and extracellular matrix and an interstitial fluid phase. Tumor growth is modeled based on principles of continuum mechanics and specifically employing the multiplicative decomposition of the deformation gradient tensor [10,39,47,124,166]. As the tumor grows, it mechanically displaces the surrounding host tissue giving rise to the development of mechanical forces. A compressible neo-Hookean constitutive equation is used to describe the mechanical behavior of both the tumor and the host tissue [7,43]. The solution of a force

balance (i.e., linear momentum equation) between the tumor and the host determines the equilibrium position of the tumor.

Macroscopic tumor growth depends on the proliferation rate of cancer cells, which is a function of oxygen concentration [91,92]. A common convection-diffusion-reaction equation is employed to govern oxygen transport to the tumor, with the reaction term to describe oxygen supply from the vessels to the tumor tissue, rendering tumor oxygenation a function of functional vascular density. Functional vascular density is compromised owing to vessel compression by cancer cells. A relationship between cancer cells attached to blood vessels and the decrease in vessel diameter was derived previously based on experiments [120], and it was validated here for a different set of experimental data (**Fig. *7-3***).

Coupling of two length scales: the cellular level equations provide a detailed description of the formation and remodeling of the tumor vasculature to calculate the functional vascular density, used at the tissue level, based on the endothelial cells population and the degree of vessel compression. The functional vascular density determines the oxygenation of the tumors and subsequently the proliferation rate of cancer cells and the overall tumor growth. A summary of model parameters, their values, and corresponding references are shown in Table 4.

7.2.4 Cancer and endothelial cell transport equations

Cancer cell transport equation

The rate of change of cancer cell density is given by the equation [164]:

$$\frac{\partial \hat{T}}{\partial t} = \nabla \cdot (D_{cell} \nabla \hat{T} - x_T \hat{T} H(1-\hat{T}) c_{ox}^{v} \nabla \hat{c}_{ox} - x_T W_{ST} \hat{T} H(1-\hat{T}) C_s^0 \nabla \hat{C}_s) + S^s \qquad (7.1)$$

where $\hat{T}$ is a dimensionless cancer cell density, D_{cell} is the cancer cell diffusion coefficient, χ_T is a chemotactic term, $\hat{c}_{ox}$ is the dimensionless oxygen concentration and c_{ox}^{v} the reference oxygen concentration of the normal tissue. $\hat{C}_s$ and C_s^0 is the dimensionless and reference SDF1α concentration, W_{ST} is a weighting function for the contribution of oxygen and SDF1 on cancer cell migration and S^s is the proliferation rate of cancer cells. H is the Heaviside function. The dimensionless cancer cell density is given division of cancer cell

density to their reference density, $\hat{T} = \frac{T}{T_0}$. The proliferation rate is given as a function of oxygen concentration via a Michaelis -Menten kinetic

$$S^s = \frac{\lambda_c c_{ox}}{k_c + c_{ox}} \hat{T} \qquad (7.2)$$

where λ_c and k_c are constant parameters derived from experimental data.

Values of all model parameters are given in Table 4.

Stable endothelial cell transport equation

The flux of endothelial cell is given by the equation [164]:

$$\frac{\partial \hat{e}}{\partial t} = \nabla \cdot (D_{EC}(a1, a2)\nabla \hat{e} - x_n \hat{e} H(1-\hat{e}) C_v^0 \nabla \hat{C}_v - W_{Se} x_n \hat{e} H(1-\hat{e}) C_s^0 \nabla \hat{C}_s) + \frac{1}{e_0}(\lambda_1 C_v^0 e_{un}^0 \hat{C}_v \hat{e}_{un} + \lambda_2 C_v^0 e_0 \hat{C}_v \hat{e}) H(1-\hat{e}) - (\lambda_3 e_{un}^0 \hat{e}_{un} + \lambda_4 e_0 \hat{e})\hat{e} \qquad (7.3)$$

Endothelial cell proliferation is based on VEGF and SDF1α concentration as well as endothelial cell density. $\hat{e}$ and $\hat{e}_{\text{un}}$ is the dimensionless stable and unstable endothelial cell density, respectively. $\hat{C}_v$ and C_v^0 is the dimensionless and reference VEGF concentration. Endothelial cells diffusion coefficient depends on Ang1 and Ang2: $D_{EC}(a_1,a_2) = D_{ec}(1+ s_1 a_1)^{-a}(1+ s_2 a_2)^b$ with a and b to be unity [165]. χ_n is a chemotactic term and W_{Se} is a weighting function describing the contribution of VEGF and SDF1α on endothelial cells transport. The dimensionless concentration of the stable and unstable endothelial cells is calculated by division with the reference concentration $\hat{e} = \frac{e}{e_0}, \hat{e}_{\text{un}} = \frac{e_{un}}{e_{un}^0}$, respectively.

Loss terms describing killing of endothelial cells are also included. The parameters λ_1, λ_2, λ_3 and λ_4 are constant positive parameters.

Unstable endothelial cell transport equation

Similar to the stable endothelial cells, the transport equation of the unstable endothelial cell density is [164]

$$\frac{\partial \hat{e}_{\text{un}}}{\partial t} = \nabla \cdot (D_{EC}(a1, a2)\nabla \hat{e}_{\text{un}} + AD_{EC}\hat{e}_{\text{un}}\nabla \hat{e} - Ax_n \hat{e}_{\text{un}}(\hat{e})H(1-\hat{e})C_v^0 \nabla \hat{C}_v$$
$$-Ax_n W_{Se}\hat{e}_{\text{un}}(\hat{e})H(1-\hat{e})C_s^0 \nabla \hat{C}_s) + (\lambda_5 G_b(\hat{c}_{ox})\hat{e}_{\text{un}}(1-\hat{e}_{\text{un}})) \quad (7.4)$$

where A is a constant that describes the increased motility of unstable endothelial cells compared to the stable. λ_5 is a positive constant and G_b is a tumor oxygen tension term given as

$$G_b(\hat{c}_{ox}) = \begin{cases} 0 \text{ for } 0 < \hat{c}_{ox} < 0.5 \\ 2\hat{c}_{ox} - 1 \text{ for } 0.5 < \hat{c}_{ox} \end{cases}$$ Ref.[164]

7.2.5 VEGF, SDF1α, Ang1 and Ang2 transport equations

VEGF transport equation

VEGF concentration is governed by the equation [164]:

$$\frac{\partial \hat{C}_v}{\partial t} = \nabla \cdot (D_{VEGF}\nabla \hat{C}_v) + \frac{\lambda_{10}}{C_v^0} G_a(\hat{c}_{ox})T - (\lambda_{11}e^0\hat{e} + \lambda_{12}e_{un}^0\hat{e}_{un} + \lambda_{13})\hat{C}_v \quad (7.5)$$

where $\hat{C}_v$ is the dimensionless VEGF concentration calculated with division with a reference value $\hat{C}_v = \frac{C_v}{C_v^0}$. VEGF is assumed to be produced by cancer cells only and its production is enhanced under hypoxic conditions as described by the oxygen tension term G_a.

$$G_a(\hat{c}_{ox}) = \begin{cases} 3\hat{c}_{ox} \text{ for } 0 < \hat{c}_{ox} < 0.5 \text{ (hypoxia)} \\ 2 - \hat{c}_{ox} \text{ for } 0.5 < \hat{c}_{ox} < 1 \text{ (normoxia)} \\ \hat{c}_{ox} \text{ for } 1 < \hat{c}_{ox} \text{ (hyperoxia)} \end{cases}$$ Ref.[164]

VEGF disappears due to binding to endothelial cells VEGF receptors and it can also diffuse in the tumor with a diffusion coefficient D_{VEGF}. λ_{10}, λ_{11}, λ_{12} and λ_{13} are positive constants.

SDF1a transport equation

The stromal cell-derived factor 1 (SDF1α) is produced by both cancer cells and endothelial cells and it is also up-regulated by hypoxia and VEGF [156]. The transport of SDF1α is governed by:

$$\frac{\partial \hat{C}_S}{\partial t} = \frac{\lambda_{10}}{C_S^0} G_a(\hat{c}_{ox})\hat{T} + \frac{\lambda_{13}}{C_S^0} C_v^0 \hat{C}_v H(1-\hat{e}) H(1-\hat{e}_{\text{un}}) - \lambda_{13}\hat{C}_S \qquad (7.6)$$

where λ_{10}, and λ_{13} are positive parameters. The dimensionless SDF1α concentration is given by division with a reference concentration, $\hat{C}_s = \frac{C_s}{C_s^0}$,

Ang1 and Ang2 transport equations

Angiopoietin 1(Ang1, α_1) and angiopoietin 2 (Ang2, α_2) are up-regulated by hypoxia and produced by unstable and stable endothelial cells, respectively.

$$\frac{\partial \hat{a}_1}{\partial t} = \frac{b_1}{a_1^0} G_a(\hat{c}_{ox})\hat{e}_{un} e_{un}^0 + \mu_1(1-\hat{a}_1) \qquad (7.7)$$

$$\frac{\partial \hat{a}_2}{\partial t} = \frac{b_2}{a_2^0} G_a(\hat{c}_{ox})\hat{e} e_0 - \mu_2 \hat{a}_2 \qquad (7.8)$$

where b_1, b_2, m_1 and m_2 are positive constants. The dimensionless Ang1 and Ang2 are given by division with a reference concentration $\hat{a}_1 = \frac{a_1}{a_1^0}$, $\hat{a}_2 = \frac{a_2}{a_2^0}$. The oxygen tension term G_a is the same as used for VEGF and SDF1α.

7.2.6 Tissue Level Equations

Calculation of vascular density

The functional vascular density is calculated by the initial vascular density (S_v^0) multiplied by the changes in the endothelial cell population (ρ_v^{EC}) [159]. To account for vessel compression, the functional vascular density is multiplied by the relative decrease in vessel diameter, a function of cancer cell density derived in [120]

$$S_v = \frac{d}{d_0} S_v^0 \rho_v^{EC} \qquad (7.9)$$

where $\rho_v^{EC} = \hat{e}$, the stable endothelial cells.

Oxygen transport equation

Oxygen (c_{ox}) diffuses across the tumor vessel wall and through the tumor interstitial space and it is consumed by cancer and normal cells, N_c. To simplify the model N_c is assumed to be a percentage of cancer cells (βT_0) with the understanding that this changes from tumor type to tumor type and during growth/regression for the same tumor. The dimensionless oxygen concentration is given by division with the oxygen concentration in the vessels, $\hat{c}_{ox} = \frac{c_{ox}}{c_{ox}^{v}}$,

$$\frac{\partial \hat{c}_{ox}}{\partial t} = D_{ox}\nabla^2 \hat{c}_{ox} - \hat{T}\frac{a_{ox}\hat{c}_{ox}}{k_{ox} + c_{ox}^{v}\hat{c}_{ox}} - \hat{N}c\frac{a_{ox}\hat{c}_{ox}}{k_{ox} + c_{ox}^{v}\hat{c}_{ox}} + P_{er}S_v(1-\hat{c}_{ox}) \qquad (7.10)$$

where a_{ox} and k_{ox} are oxygen uptake constants, D_{ox} is the diffusion coefficient of oxygen in the interstitial space and P_{er} is the vascular permeability of oxygen that describes diffusion across the tumor vessel wall.

7.2.7 Biomechanical model of tumor growth

To model tumor growth we used the multiplicative decomposition of the deformation gradient tensor. The tensor, **F**, is decomposed into two independent motions: the growth of the tumor, $\mathbf{F}_g$, and the elastic mechanical interactions, $\mathbf{F}_e$ [39,47,124,166]:

$$\mathbf{F} = \mathbf{F}_e\mathbf{F}_g. \qquad (7.11)$$

Tumor growth was taken to be isotropic, i.e., $\mathbf{F}_g = \lambda_g \mathbf{I}$, where the growth stretch ratio, λ_g is calculated as a function of the oxygen concentration in the tissue:

$$\frac{d\lambda_g}{dt} = \frac{1}{3}\lambda_g S^S \qquad (7.12)$$

where S^s is the creation/degradation of the cancer cells.

The elastic component of the deformation gradient tensor is given by

$$\mathbf{F}_e = \mathbf{F}(\mathbf{F}_g)^{-1} \qquad (7.13)$$

The tumor mechanical behavior is governed by the compressible neo-Hookean constitutive equation with strain energy density function given by

$$W = 0.5\mu\left(-3 + II_1\right) + 0.5\kappa\left(-1 + J_e\right)^2 \qquad (7.14)$$

where μ is the shear modulus, κ is the bulk modulus, J_e is the determinant of the elastic deformation gradient tensor $\mathbf{F}_e$, $II_1 = I_1 J_e^{-2/3}$, and I_1 is the first invariant of the right Cauchy-Green deformation tensor, evaluated from $\mathbf{F}_e$.

The equations for solid (cells and extracellular matrix) and interstitial fluid phase conservation are:

$$\frac{d\varphi^s}{dt} + \nabla \cdot \left(\mathbf{v}^s \varphi^s\right) = S^s \qquad (7.15)$$

$$\frac{d\varphi^w}{dt} + \nabla \cdot \left(\mathbf{v}^w \varphi^w\right) = Q \qquad (7.16)$$

where φ^s and φ^w are the volume fractions of the solid and fluid phase, respectively and $\mathbf{v}^s$ and $\mathbf{v}^w$ are the corresponding solid and fluid velocities. The rate of cancer cell proliferation S^c is given in Eq.*(7.2)*. The quantity Q describes the fluid entering the tissue from the blood vessels and exiting the tissue through the lymphatics and it is calculated from Starling's approximation:

$$Q = L_p S_v \left(p_v - p\right) - L_{pl} S_{vl} \left(p - p_l\right) \qquad (7.17)$$

where p_v, L_p and S_v are the micro-vascular pressure, hydraulic conductivity and vascular density of the blood vessels, respectively, and p_l, L_{pl} and S_{vl} are the corresponding quantities for the lymphatics.

The total stress of the tissue is the sum of the stress of the solid phase and the interstitial fluid pressure. The equilibrium position of the tumor at each time is calculated by the solution of a force balance between and within the tumor and the host tissue, which is described by the linear momentum balance:

$$\boldsymbol{\sigma}^{total} = \boldsymbol{\sigma}^s - p\mathbf{I} \qquad (7.18)$$

$$\nabla \cdot \left(\boldsymbol{\sigma}^{total}\right) = \mathbf{0} \qquad (7.19)$$

where $\boldsymbol{\sigma}^s$ is the solid stress tensor and *p* is the IFP. The solid stress (i.e., stress of the solid phase) is calculated from the strain-energy density function as

$$\boldsymbol{\sigma}^s = J_e^{-1}\mathbf{F}_e \frac{\partial W}{\partial \mathbf{F}_e^T} \qquad (7.20)$$

Finally, the fluid pressure *p* is calculated by taking the sum of the mass conservation equations (Eqs. *(7.14)*and *(7.15)*), taking into account that the sum of the volume fractions of the two phases should equal unity and incorporating Darcy's law for the calculation of the fluid velocity. It yields:

$$-k\nabla^2 p + \nabla \cdot \mathbf{v}^s = Q + S^s \qquad (7.21)$$

7.2.8 Computational domain and boundary conditions

The model equations were solved simultaneously using the commercial finite elements software Comsol Multiphysics v. 5.2a (COMSOL, Inc., Burlington, MA, USA). Values of the model parameters are provided in Table 4**.** The computational domain consists of a spherical tumor that grows within a cube. Because of symmetry we solved only for the one eight of the domain (**Fig. *7*-*5*B**). We simulated a murine tumor that grows within a period of 30 days based on published experimental results. The boundary conditions for the continuity of the stress and displacement fields, as well as the concentration of the oxygen at the interface between the tumor and the host tissue were applied automatically by the software, the remaining symmetry boundary conditions are no flux of $((-\boldsymbol{n} \cdot (J_i) = 0$, *i*=*T*,C_v,*e*,e_{un},a_1,a_2,C_S) and stress free in the displacement parameters is ($\boldsymbol{n} \cdot \boldsymbol{\sigma} = 0$).

7.3 **Results**

7.3.1 Kinetics of co-option of host vessels in a GBM mouse model

We first set out to investigate the kinetics of vessel co-option in an invasive glioblastoma tumor model. The CNS-1 tumor cell line was employed with cells growing into the cerebrum of SCID mice. Using a transparent cranial window model, we performed intravital (MPLSM) microscopy imaging of the tumor cells and blood vessels every two or three days.

Fig. *7-2A* depicts representative images of the kinetics of vessel co-option. The invasive tumor cell line CNS-1 (red) invades (arrows) along the large meningeal vessels (green) of the brain. Within the first 11 days from cell implantation, significant vessel co-option occurs.

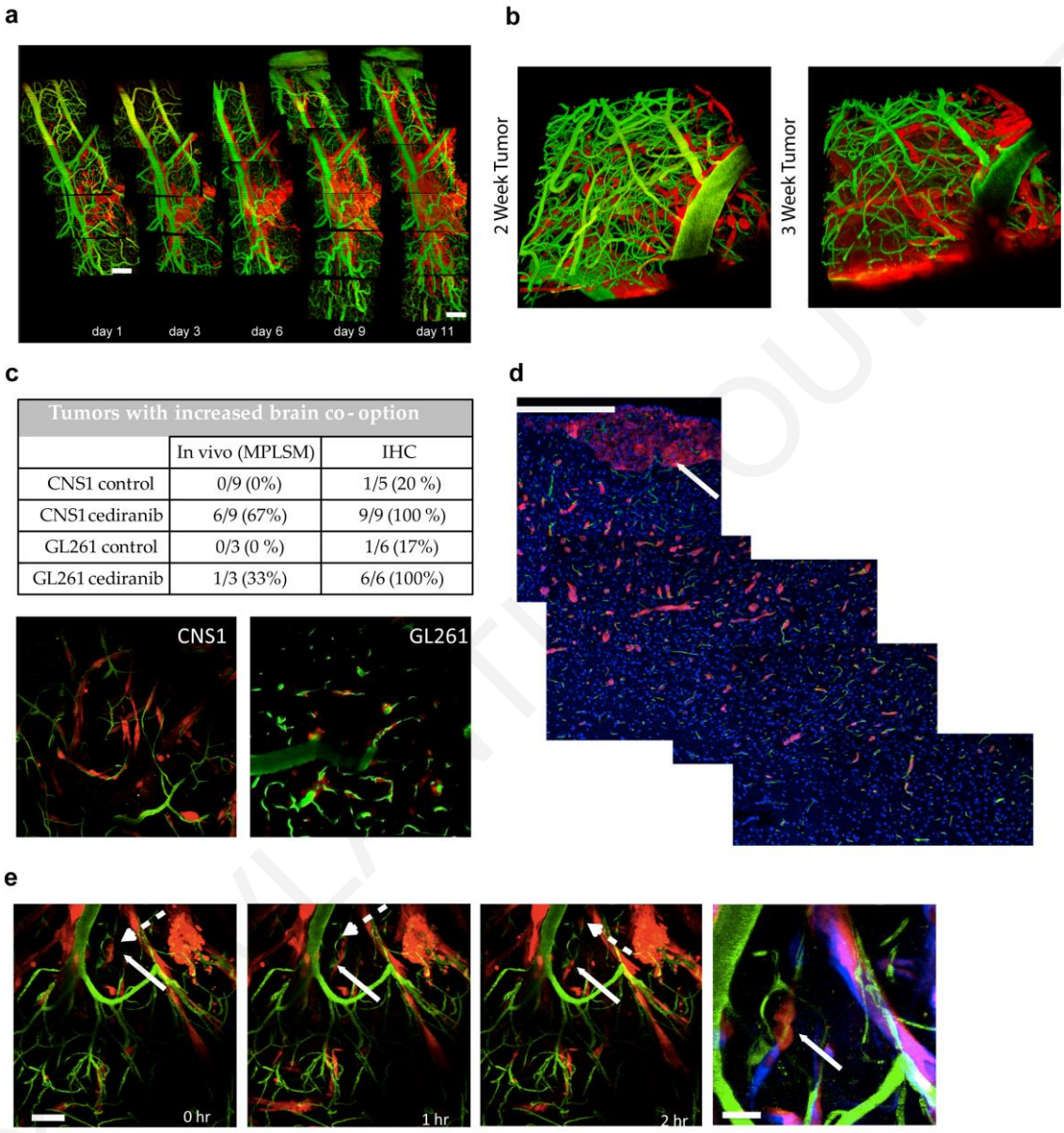

Fig. *7-2.* Experimental model of co-option. (A) Using intravital microscopy, CNS-1 tumor cells (red) growing along the brain vasculature (green) are observed. Over time the tumor cells proliferate but the infiltration of surrounding parenchyma is via vessel co-option. Scale bar is 50 μm (B) After 2 to 3 weeks (Day 16 and 21, respectively), the tumor has fully established in the brain as illustrated with the 3D projections. It should be noted that a central tumor mass has formed at this stage below the displayed 3D volume. (C) Anti-

angiogenic treatment increases vessel co-option. Quantification of both *in vivo* and the immunofluorescence staining of tissue shows an increased vessel co-option by tumor cells with less central mass growth and more preferential tumor growth along brain vessels. (D) The extent of tumor spread from tumor mass (white arrow) by co-option is shown in immunofluorescence sections of GL261 tumors following cediranib treatment (red = GL261 tumor cells, green = CD31+ vessels, blue = nuclei, scale bar = 200 μm. (E) An interesting observation with co-opting tumor cells. A single cell division was followed (arrows) with the daughter cells subsequently migrating in opposite directions along the vessel (bottom right panel, blue color indicates final position of cells, red is original position).

7.3.2 Increased brain vessel co-option by glioma cells following anti-angiogenic treatment

Subsequently, we studied the effect of anti-angiogenic treatment on the formation of co-opted vessels in glioblastomas. The invasive CNS-1 and GL261 glioma cell lines were employed in orthotopic models of brain tumors and mice were treated with 6 mg/kg cediranib, an anti-angiogenic TKI. **Fig. *7-2*B** shows that during anti-angiogenic treatment outside the main established tumor mass infiltrative tumor cells are observed along brain vessels (tumor mass below rendered 3D volume). We further quantified brain co-option by scoring tumor cell association with and infiltration along brain vessels outside of the tumor mass from *in vivo* and immunohistochemistry data. Both modalities suggest an increase in co-option in the two different tumor cell lines, following chronic cediranib treatment (>2 weeks, **Fig. *7-2*C**). Additionally, we observed that both CNS-1 and GL261 tumors invade deep into the perivascular space of the brain parenchyma following cediranib treatment. Multiphoton microscopy optical sections at depths over 200 μm in the brain (**Fig. *7-2*C**) show a clear preference of tumor cells (red) to invade along brain microvessels (green). On the side, using immunohistochemistry, we measured co-opted regions that extended over 1 mm from the primary lesion. Sections were stained with a CD31 antibody (green) and DAPI (blue) to co-localize with tumor cells (red). As observed *in vivo*, the invasion is primarily perivascular in nature **Fig. *7-2*D**. Finally, we were also able to perform time-lapse imaging of tumor cells during cediranib treatment (**Fig. *7-2*E**, panels, 1-3). We observed throughout

the invaded regions that tumor cell doublets (red, arrows) were the most motile cells invading along vessels (green) up to 54 μm/hr. We also observed that the initial location of the tumor cell doublet (red, arrow) overlayed with the displacement of the cells after 2 hours (blue), (**Fig. *7-2*E**, panel 4).

7.3.3 Mechanical compression of co-opted blood vessels

To study the effect of vessel co-option on the morphology of tumor blood vessels, we developed a brain metastasis model formed by intracardiac injection of MDA-231BR breast cancer cell suspension in nude mice carrying a cranial window to allow for intravital (MPLSM) microscopy. The formation of co-opted vessels in the brain was observed 4 weeks after injection, whereas robust co-option was observed after 7 weeks. **Fig. *7-3*A,B** depict MPLSM images of the co-option of blood vessels (red) by metastatic cells transfected with green fluorescent protein (GFP, green) and **Fig. *7-3*C** is an immunofluorescence image of cancer cells (green), blood vessels (red) and cell nuclei (DAPI, blue), showing blood vessel co-option. Vessel co-option can cause the compression of the co-opted vessels as shown in Fig. 3d-f, using H&E staining. Arrows indicate blood vessels with red blood cells. Blood vessels co-opted by cancer cells appear to have elliptical shapes (**Fig. *7-3*D,E**) or a smaller lumen than vessels that are not surrounded by cells (**Fig. *7-3*F**). Both modes of vessel deformation are typical of vessel compression owing to mechanical forces that cancer cells exert on the vessels [6,26,27].

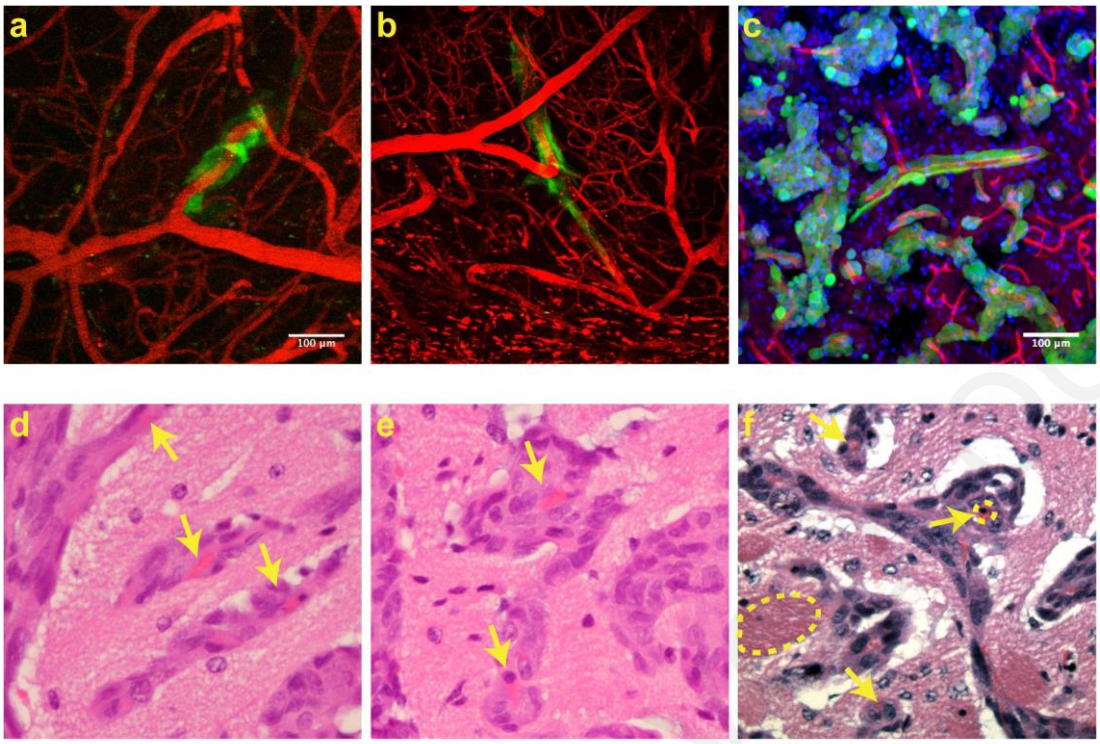

Fig. *7-3.* Vessel co-option compresses tumor blood vessels. (A-B) Using intravital microscopy, co-option of tumor blood vessels (red) by metastatic MDA-231BR cells (green) is observed. (C) Vessel co-option is further supported by immunofluorescence imaging. (D-F) H&E images of brain tumor sections show the compression of blood vessels by forces exerted by cancer cells (arrows) (Blood vessels diameters: compressed 4-6µm and uncompressed 22-45µm).

7.3.4 Validation of model predictions for vessel co-option kinetics and tumor blood vessel compression

Following, our analysis was focused on validating our mathematical modeling framework. The model first accounted only for cellular events and we compared model predictions to two independent studies to illustrate the capacity of the model to predict cancer cell co-option around a single vessel and the reduction in vessel diameter owing to cancer cell-induced vessel compression. The computational domain of the single vessel geometry is shown in **Fig. *7-5***. It has an orthogonal shape, cancer cells are located on one side of the domain, and the vessel is placed in the middle. Model results are compared to our previous

experimental observations of single vessel co-option in orthotopic glioblastoma cells (DsRed-expressing CNS-1 cells) [108] showing that the model can predict the time scale of cancer cell attachment to the vessel wall (**Fig. *7-4*A**). Additionally, in the study by Watkins et al. [167] vessel diameters in gliomas implanted in the cerebrum of immunodeficient mice were related to the number of cancer cells attached to the vessel wall. The good agreement of the model predictions with the experimental data is shown in **Fig. *7-4*B,C** and also comparing **Fig. *7-4*C** with our experimental data in Fig. 3d-f. Therefore, the model provides reasonable predictions for the evolution of cancer cell co-option around blood vessels and the corresponding decrease in the co-opted vessel diameter.

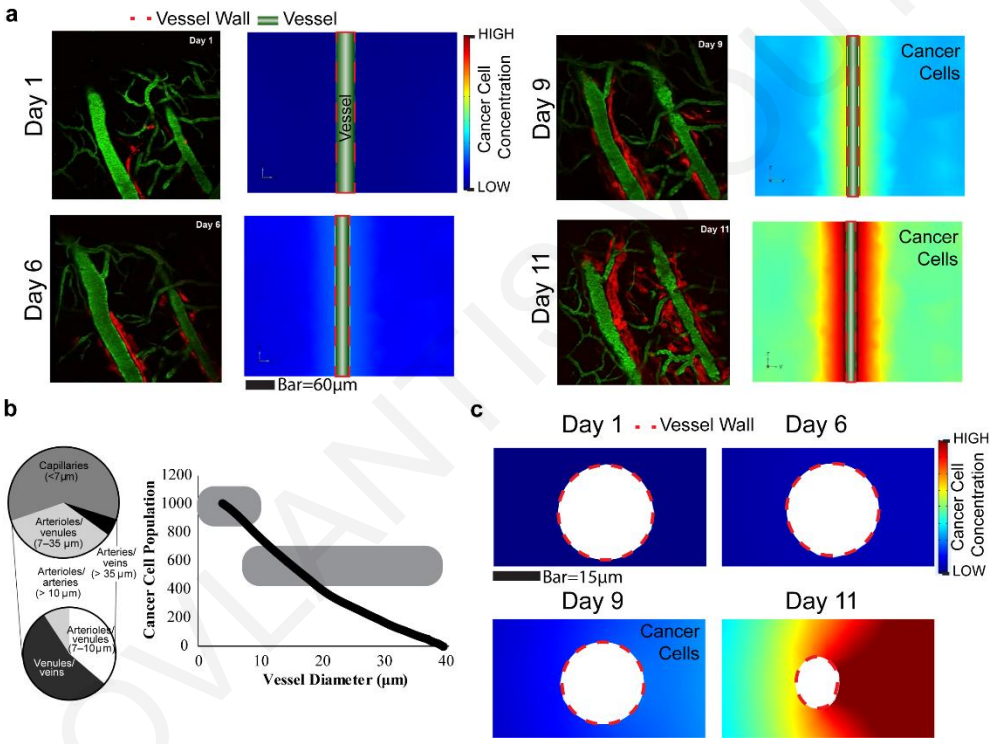

Fig. *7-4*. Model validation for co-option kinetics and vessel compression. (A) Model predictions are compared with experimental data [108] for the temporal evolution of vessel co-option around a single vessel. Red represents glioblastoma cells (DsRed-expressing CNS-1 cells), and green represents perfused blood vessels (FITC-dextran injected intravenously). In our model we adapted the migration/diffusion coefficient of cancer cells so as the co-option to resemble the experimental observations. (B) The decrease in vessel diameter as a function of cancer cells attached to the vessel wall agrees well with pertinent experimental data for gliomas [167]. (C) Model predictions for the evolution of cancer

cell co-option around blood vessel and decrease in co-opted vessel diameter are in agreement with experimental data in **Fig. *7-2*d**.

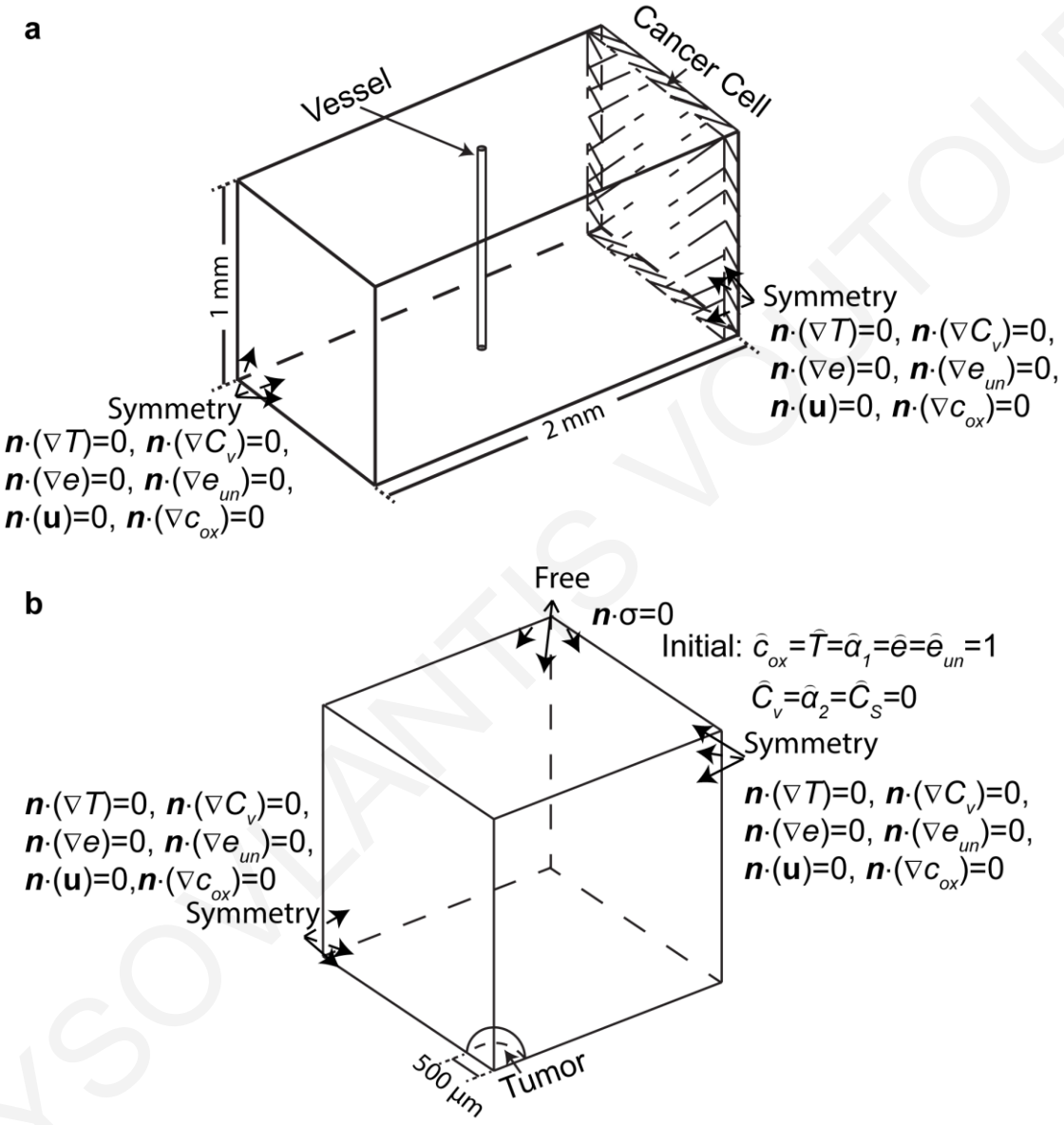

Fig. *7-5*. Geometry and boundary conditions employed in the model.

.

7.3.5 Validation of model predictions for tumor oxygenation, Ang2, VEGF and vascular density

Subsequently, we employed the coupled cellular and tissue level model assuming a spherical tumor growing within a cubic host tissue. Assuming symmetry we solved the complete model equations only for the one-eighth of the domain (**Fig. *7-5*B**) and compared model predictions to two separate studies [139,168]. In the first study, Cao et al., [168] studied the incipient tumor angiogenesis that is independent of hypoxia using genetically engineered HCT116 human colon carcinoma cells and found that incipient tumor vessel formation, presumably owing to co-option, preceded hypoxic response, whereas a secondary, more intensive angiogenesis appeared after hypoxia. Specifically, they found that hypoxia appeared on day 3 following cancer cell implantation and it was observed at the interior region of the tumor. **Fig. *7-6*** presents the experimentally measured spatiotemporal evolution of hypoxia along with the model predictions taken from a section of the computational domain. In agreement with the experiments, the model predicted a significant decrease in oxygen concentration at the center of the tumor starting from day 3 of tumor growth.

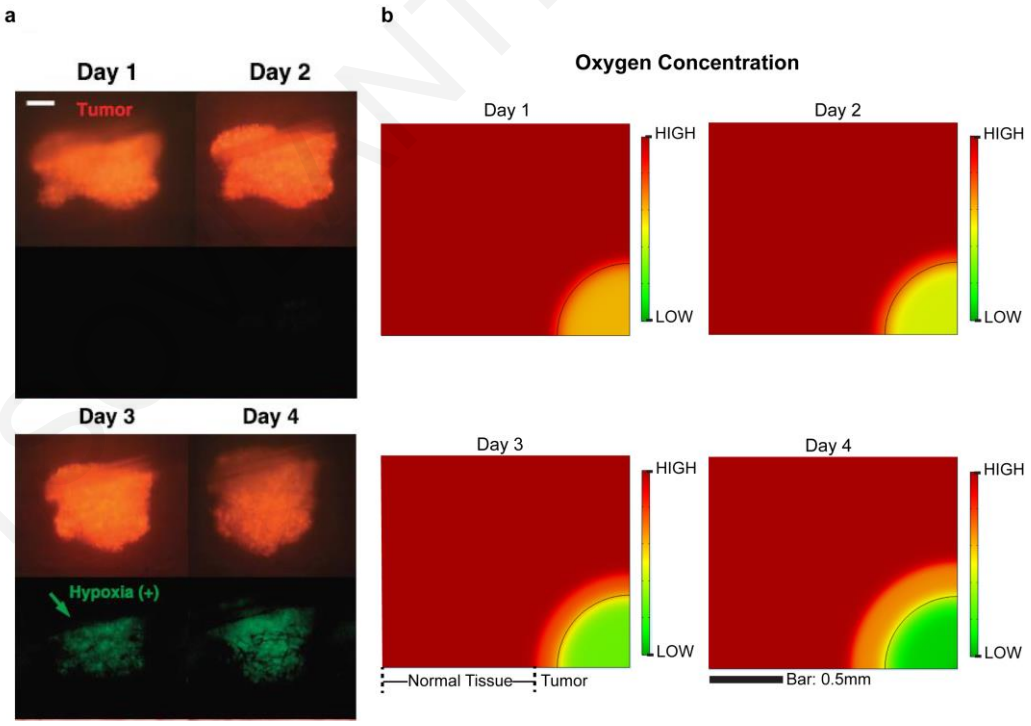

Fig. *7-6*. Validation of model predictions for tumor oxygenation against experimental data by Cao et al. [168]. (A) representative window chamber images of a saline-treated

HCT116 tumor showing the hypoxic response (Day 3; green arrow). (B) Model results are in agreement with the experiments, predicting formation of hypoxia from day 3 of tumor growth. In the experiments douple-fluorescent reporter cells were established to be activated by fluorescence (dsRed) and hypoxia (GFP).

The hypoxic response, in turn, up-regulates Ang2 and VEGF levels, driving VEGF depended tumor angiogenesis. Vessel co-option and its effects on the spatiotemporal evolution of Ang2 and VEGF as well as on the resulting vascular network was thoroughly studied by Holash et al.[139] using a rat glioma model. They found that the co-opted host vasculature does not immediately undergo angiogenesis but first regresses and after an onset of hypoxia is rescued by robust angiogenesis regulated by Ang2 and VEGF. Specifically, it was shown that these two proteins are up-regulated during the 4th week of glioblastomas growth and are concentrated at the tumor periphery where significant angiogenesis is observed. Experimental data along with the corresponding model results are depicted in **Fig. *7-7***. Our model predicts well both the spatial and temporal evolution of Ang2, VEGF, and angiogenesis. Additionally, model predictions for cancer cell population, Ang1 and SDF1α that were not measured in Holash et al. [139] are presented in **Fig. *7-8*** showing an increase in cancer cell density and Ang1 at the periphery of the tumor, whereas the distribution of SDF1α is higher at the tumor center and decreases towards the periphery.

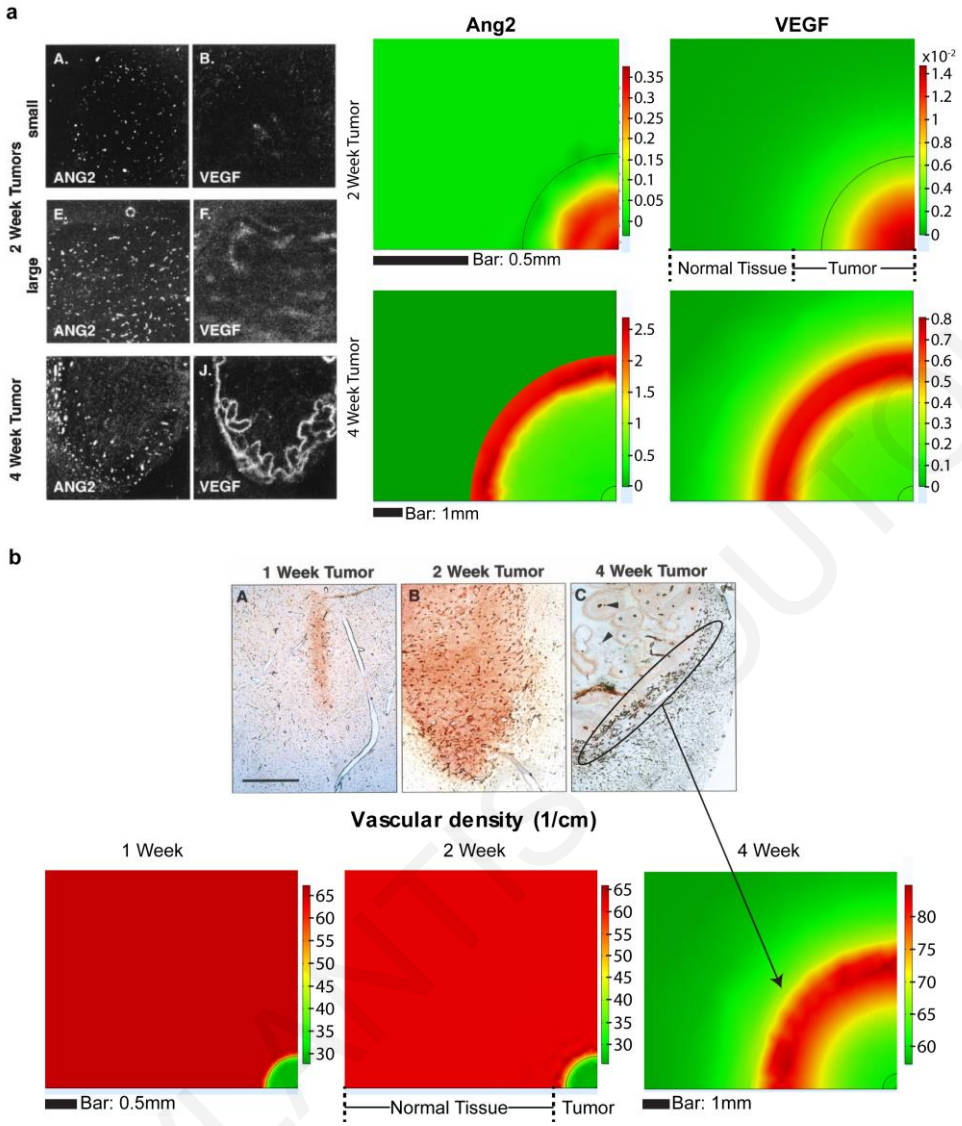

Fig. *7-7.* Model validation for VEGF, Ang2 and vascular density from data taken from Holash et al. [139] using a rat glioma model.(A) In situ hybridization analysis of Ang-2 and VEGF mRNA in 2-week rat gliomas (small and large) and a 4-week rat glioma (left). Model predictions of Ang-2 and VEGF during tumor growth showing the concentration of the two proteins at the tumor periphery at the 4-week of tumor growth (right). (B) Sections from rat C6 gliomas showing vessel growth. Two-week tumors continue to have extensive internal vasculature, although the vessel density is less than that in the surrounding brain tissue. In 4-week tumors internal vessels regress but robust angiogenesis is apparent at the tumor periphery (top). Model predictions are able to capture the experimental observations (bottom).

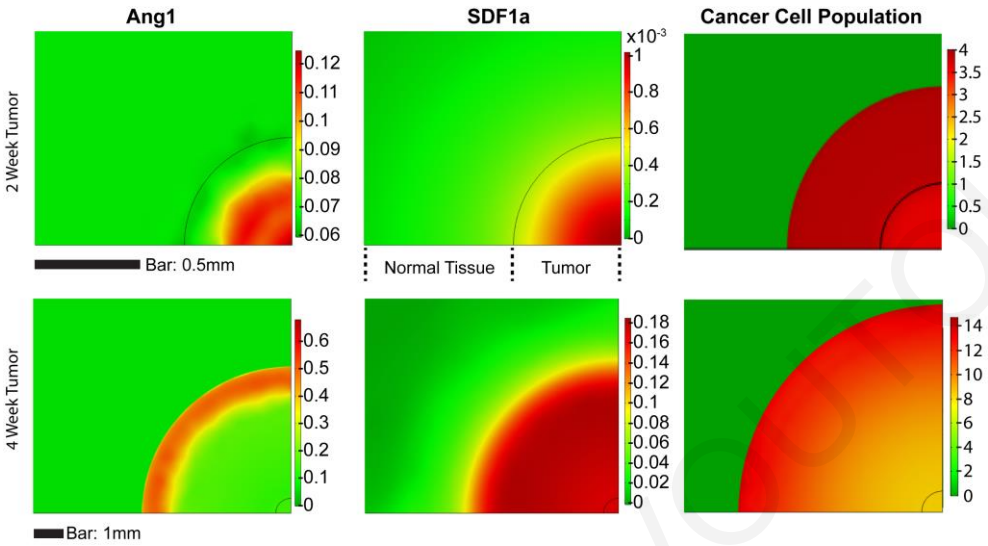

Fig. *7-8*. Cancer cells move towards the high oxygen levels (tumor periphery, red color). Ang1 is concentrated at the periphery of the tumor, and SDF1a is mainly produced at the tumor center.

7.3.6 Vessel co-option resists to anti-angiogenic treatment and coordinates cancer cell diffusion to the invasive front

It has been reported in the literature [145-147] that VEGF blockade and the subsequent inhibition of angiogenesis in glioblastomas can be compensated by persistent co-option, which has been proposed as a mechanism for tumor resistance to anti-angiogenic treatment. In the model, we blocked the effect of VEGF on endothelial cell migration and observed changes in vascular density, cancer cell population, and tumor growth. Interestingly, the model predicted a reduced but still significant and more uniform distribution of blood vessels throughout the tumor and a more coordinated movement of cancer cells towards the tumor periphery (**Fig. *7-9*A**) in agreement with our experimental observations in Fig. 2b. The model also suggests that VEGF blockage does not lead to blood vessel pruning but instead, the tumor remains well vascularized and tumor growth remains unaffected (**Fig. *7-9*B**)

confirming pertinent experimental studies. Subsequently, we repeated simulations blocking both vessel co-option and VEGF. The model predicts a decrease in tumor vascular density, which was related to a significant reduction in tumor growth rate. Therefore, we can conclude that in tumors that are resistant to anti-VEGF therapy, both mechanisms of vascular modification should be targeted to achieve tumor regression.

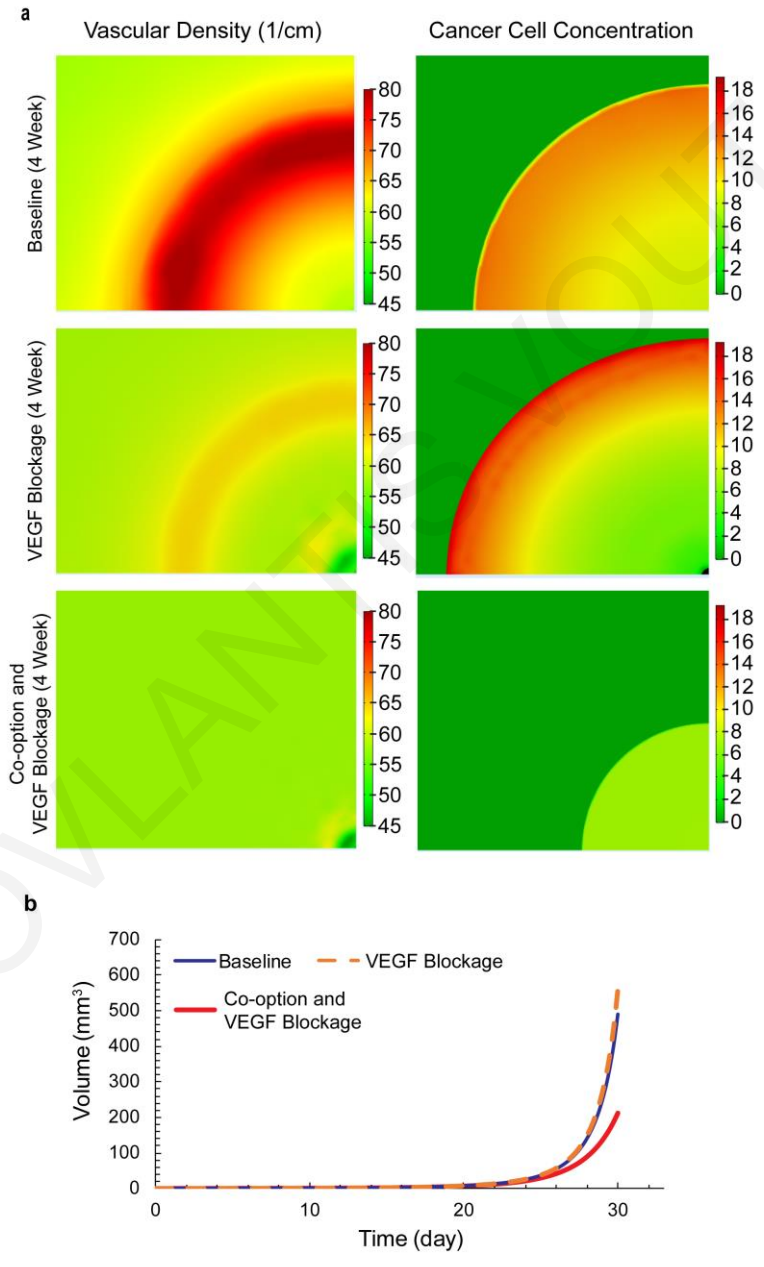

Fig. *7-9.* Model predictions for tumor response in anti-VEGF treatment and for both VEGF and co-option blockage. (A) Vascular density and cancer cell population as well as (B) tumor growth are plotted for the baseline simulations, in the absence of VEGF binding

to cancer cells, for both VEGF and vessel co-option blockage. Only for the latter case significant reduction in vascular density and tumor growth is predicted.

7.4 Discussion

With the recent US approval of bevacizumab for treatment of rGBM, anti-VEGF therapy in these tumors is quickly becoming part of the standard of care. It is therefore critical to understand the tumor response to this therapy. Here, we found that long-term treatment of established GBMs with anti-angiogenic TKIs leads to an increase in tumor invasion along existing brain vessels. This work provides a foundation for dynamic imaging of this process and further investigation of the mechanisms governing tumor co-option in the brain.

Furthermore, to provide more insights of the vessel co-option mechanism, we developed a mathematical framework for tumor growth taking into account mechanistic events involved in the early stage of vascular modification through co-option of the host vasculature and the secondary, VEGF-dependent angiogenic process. The model was tested against a large set of experimental data and provided a good qualitative agreement for the spatiotemporal evolution of vessel co-option, VEGF and Ang2 levels, vascular density distribution and tumor oxygenation. A fully quantitative comparison was not possible because the experimental results were not quantified so that they could be directly employed and compared by the model. Interestingly, according to the model, vessel co-option and the subsequent compression by cancer cells takes place from the early stages of carcinogenesis and leads to the formation of a hypoxic tumor microenvironment at the tumor interior, which in turn drives a more robust angiogenic response localized at the tumor periphery. In the absence of the secondary VEGF dependent angiogenesis, an effective tumor vasculature will still be maintained owing to co-option. When both co-option and VEGF are blocked tumor vasculature and growth are decreased drastically, suggesting that anti-angiogenic therapy should be combined with blockage of co-option.

The model is subject to certain limitations including the incorporation of only a subset of proteins (Ang1, Ang2, VEGF, and SDF1α) that participate in the vascular response of tumors. Other proteins such as hypoxia-inducible factor 1 (HIF1), platelet-derived growth factor, and thrombospondin 1 (TSP-1)are also involved in tumor angiogenesis and are not considered by the model [140]. Also for the proteins incorporated into the model, some

mechanisms might not be included, such as the fact that VEGF can be produced not only by cancer cells but also by host cells [169]. Additionally, the model does not account for other types of cancer and host cells, such as stem-cell-like cancer cells and immune cells that play a key role in the therapeutic effect of the drug [124]. Given its complexity and comprehensiveness, our model includes a large number of parameters (Table 4) that are associated with cancer and endothelial cell proliferation and motility, angiogenic protein transport, tumor properties, and other functions. Baseline values of the model parameters were determined independently using data from the literature.

Table 4. Parameter values used in the model.

Parameter	**Description**	**Value**		**Ref**
		Cellular	Tissue	
Dcell	Cell diffusion coefficient	5.11x10-14 [m2/s]	1.5x10-12 [m2/s]	tw/tw
Dox	Oxygen diffusion coefficient	1.78x10-9 [m2/s]	1.78x10-9 [m2/s]	[49,124]
DVEGF	VEGF diffusion coefficient	3.1x10-11 [m2/s]	3.1x10-11 [m2/s]	[164,170]
Dec	Endothelial cell diffusion coefficient	1x10-15 [m2/s]	1x10-15 [m2/s]	[165]
χT	Chemotactic cancer cell	7x10-14 [m5/kg-s]	7x10-14 [m5/kg-s]	tw
xn	Chemotactic endothelial cell	2x10-15 [m5/kg-s]	1x10-12 [m5/kg-s]	tw
WST	Weight between oxygen-SDF1	1	1	tw
WSe	Weight between VEGF-SDF1	1	1	tw
C_s^0	Reference SDF1 concentration	1x10-3 [g/m3]	1x10-3 [g/m3]	tw
C_v^0	Reference VEGF concentration	1x10-3 [g/cm3]	1x10-3 [g/cm3]	[164,170]
e0	Reference value of stable endothelial cell	1x10-3 [g/cm3]	1x10-3 [g/cm3]	[164,171]
e_{un}^0	Reference value of unstable endothelial cell	1x10-3 [g/cm3]	1x10-3 [g/cm3]	[164,171]
a_1^0	Reference a1 concentration	1x10-3 [g/cm3]	1x10-3 [g/cm3]	tw
a_2^0	Reference a2 concentration	1x10-3 [g/cm3]	1x10-3 [g/cm3]	tw
c_{ox}^v	Vascular oxygen concertation	0.2 [mole/m3] 6.4 [g/m3]	0.2 [mole/m3] 6.4 [g/m3]	[49,124,172]

T0	Reference cancer cell density	1x10-3 [g/cm3]	1x10-3 [g/cm3]	[164]
λ1	Positive parameters	1x10-3 [cm3/g-s]	1x10-3 [cm3/g-s]	tw
λ2	Positive parameters	1x10-5 [cm3/g-s]	1x10-2 [cm3/g-s]	tw
λ3	Positive parameters	1x10-3 [cm3/g-s]	1x10-3 [cm3/g-s]	[164,173]
λ4	Positive parameters	1x10-1 [cm3/g-s]	1x10-1 [cm3/g-s]	[164,173]
λ5	Positive parameters	5.56x10-7[1/s]	5.56x10-7[1/s]	[164,174,175]
λ10	Positive parameters	6.8x10-3 [1/s]	6.8x10-6 [1/s]	tw
λ11	Positive parameters	4 [cm3/g-s]	4 [cm3/g-s]	[164,176,177]
λ12	Positive parameters	4 [cm3/g-s]	4 [cm3/g-s]	[164,176,177]
λ13	Positive parameters	4x10-5 [1/s]	4x10-5 [1/s]	[164,166,178]
b1	Positive parameters	2280 [1/h]	2280 [1/h]	[165]
b2	Positive parameters	18240 [1/h]	18240 [1/h]	[165]
μ1	Positive parameters	456 [1/h]	456 [1/h]	[165]
μ2	Positive parameters	456 [1/h]	456 [1/h]	[165]
s1	Positive parameters	1x103 [cm3/ g]	1x103 [cm3/ g]	tw
s2	Positive parameters	1x103 [cm3/ g]	1x103 [cm3/ g]	tw
A	Positive parameters	30	30	tw
aox	Oxygen uptake parameter	2200 [mole/m3d]	2200 [mole/m3d]	[49,91,124]
kox	Oxygen uptake parameter	0.00464 [mole/m3]	0.00464 [mole/m3]	[49,91,124]
Per	Vascular permeability	3.58x10-4 [m/s]	3.58x10-4 [m/s]	[124]
β	Percentage Normal Cells	0.3	0.3	tw
μ	Shear modulus	---	60 [103] Tumor 21 [103] Host	[38,121]
ν	Poison's ratio	---	0.45 Tumor 0.2 Host	[38,121]
λc	Contact parameter	---	0.07 [1/d]	tw
κc	Contact parameter	---	0.0083 [mole/m3]	[91,124]
Lp	Hydraulic conductivity of blood vessel	---	2.7x10-12 [m/Pas]	[124]
LplxSvl	Hydraulic conductivity of lymphatics vessel	---	3.75x10-4 [1/Pa-s]	[124]

S_v^0	Initial vessel density	---	70 [1/cm]	[124]
k	Hydraulic conductivity of interstitial space	---	6.5x10-11 [m2/Pad]	[121]

8 Contribution and Future Directions

In this work, we have shown that the mechanical behavior of solid tumors is highly nonlinear even at low strains and it can be better described by an exponential constitutive equation. The state of stress of a growing tumor, however, does not depend so much on the selection of the constitutive equation, but it is determined by the mechanical interactions with the surrounding host tissue, and particularly by the mechanical properties of the host. According to our calculations and in agreement with *in vitro* studies, solid tumors must exceed a critical stiffness compared with the host tissue in order to be able to displace the host tissue and grow. With the use of our mathematical model, we estimated this critical value to be on the order of 1.5. Therefore, the direct effect of solid stress on tumor growth involves not only the inhibitory effect of stress on cancer cell proliferation and the induction of apoptosis[24], but also the resistance of the surrounding tissue to tumor expansion. Conclusively, our model and findings provided important insights about the role of host tissue-tumor interactions in cancer progression and may serve as the basis for the design of novel therapeutic strategies. Furthermore, we performed unconfined compression experiments of tumor specimens in a dynamic mechanical analysis system to characterize their response and subsequently, using in vivo experiments we showed that stress alleviation improves the delivery of chemotherapeutic drugs and nanomedicines. We proposed the repurposing of Tranilast, a clinically approved and inexpensive antifibrotic drug, as a stress-alleviating agent. Using two breast cancer cell lines and three chemo- and nano-therapeutic drugs we showed that Tranilast significantly reduced mechanical stresses, decreased IFP, improved perfusion, and markedly enhanced efficacy of drugs and therapeutic outcomes.

Also, we performed a comprehensive study that provided new insights on the mechanopathology of solid tumors, highlighting the effect of tumor structure on the tissue function and pathophysiology and the role of ECM components in tumor mechanical response, and tissue swelling in particular. Our findings and especially the direct, linear correlation of swelling stress to tumor ECM content as well as the inverse correlation of perfusion to tumor swelling provide novel considerations for the use of stress alleviation

strategies to modify the microenvironment of solid tumors in order to enhance therapeutic outcome. As well, using a series of experimental data and computational calculations, we concluded that growth-induced stress is largely determined by tumor content and it is affected by tumor stiffness. Thus, stress-alleviating drugs targeting both collagen and hyaluronan can alleviate intratumoral solid stresses both by reducing tumor swelling and by making the tumor less stiff. Furthermore, to quantify perfusion clinically approved, immunochemistry-based techniques could be employed and a software package could be developed, which could calculate the ratio of collagen and hyaluronan and could be potentially used by clinical oncologists as a predictive tool for patient-specific treatment.

Co-option of the host vasculature is a strategy with which some cancer cells can sustain tumor progression without or prior to initiation of an angiogenic response, orchestrated by vascular growth factors. It has also been related to tumor resistance against anti-angiogenic treatments and brain tumor metastasis. However, the underlying mechanisms of vessel co-option are not fully understood. In Chapter 7, performing a series of experiments in orthotopic gliomas and brain metastasis from breast cancer cells we presented the kinetics of vessel co-option, its evolution during anti-angiogenic treatment and evidence of compression of co-opted vessels. Subsequently, we employed mathematical modeling to provide insights into the experimental observations. The model predicted that co-option induced vessel compression resulting in hypoxia, which in turn upregulates angiogenic factors for the formation of new tumor blood vessels. In the absence of tumor angiogenic factors, co-option of existing vessels sustains, providing resistance to anti-angiogenic treatments and supporting tumor progression.

In future work, the model can be extended to incorporate a district blood vessel network accounting explicitly for tumor-induced angiogenesis and for the remodeling of the vascular network owing to compression of tumor vessels, changes in shear stress and in response to biochemical factors, such as gradients of angiogenic growth factors. The model can be also further extended to account for the immune system. Immunotherapy has been a promising area of cancer research and therapy and our model can be further developed to incorporate the population of immune cells that play key role in cancer treatment such as CD4 and CD8 Tcells and macrophages. As far as the experimental part of the work is concerned, we have shown that tranilast can be used to improve delivery of drugs to solid tumors and ongoing studies have shown that combined used of tranilast with nanomedicine can improve

significantly the overall survival in mice bearing breast tumors. Given the fact that tranilast is an approved anti-fibrotic drug, it could be repurposed and used to enhance cancer therapy. Clinical trials are required for the promise of this new strategy to be realized by cancer patients.

List of Tables

List of Figures

References

1. Vakoc BJ, Lanning RM, Tyrrell JA, Padera TP, Bartlett LA, et al. (2009) Three-dimensional microscopy of the tumor microenvironment in vivo using optical frequency domain imaging. Nat Med 15: 1219-1223.
2. Stylianopoulos T, Martin JD, Chauhan VP, Jain SR, Diop-Frimpong B, et al. (2012) Causes, consequences, and remedies for growth-induced solid stress in murine and human tumors. Proceedings of the National Academy of Sciences of the United States of America 109: 15101-15108.
3. Jain RK (2008) Taming vessels to treat cancer. Sci Am 298: 56-63.
4. Baluk P, Hashizume H, McDonald DM (2005) Cellular abnormalities of blood vessels as targets in cancer. Curr Opin Genet Dev 15: 102-111.
5. Hobbs SK, Monsky WL, Yuan F, Roberts WG, Griffith L, et al. (1998) Regulation of transport pathways in tumor vessels: role of tumor type and microenvironment. Proc Natl Acad Sci U S A 95: 4607-4612.
6. Stylianopoulos T, Martin JD, Snuderl M, Mpekris F, Jain SR, et al. (2013) Coevolution of solid stress and interstitial fluid pressure in tumors during progression: Implications for vascular collapse. Cancer research 73: 3833-3841.
7. Voutouri C, Mpekris F, Papageorgis P, Odysseos AD, Stylianopoulos T (2014) Role of constitutive behavior and tumor-host mechanical interactions in the state of stress and growth of solid tumors. PLoS One 9: e104717.
8. Stylianopoulos T (2017) The Solid Mechanics of Cancer and Strategies for Improved Therapy. J Biomech Eng 139.
9. McGrail DJ, McAndrews KM, Brandenburg CP, Ravikumar N, Kieu QM, et al. (2015) Osmotic Regulation Is Required for Cancer Cell Survival under Solid Stress. Biophys J 109: 1334-1337.
10. Voutouri C, Polydorou C, Papageorgis P, Gkretsi V, Stylianopoulos T (2016) Hyaluronan-Derived Swelling of Solid Tumors, the Contribution of Collagen and Cancer Cells, and Implications for Cancer Therapy. Neoplasia 18: 732-741.
11. Boucher Y, Jain RK (1992) Microvascular pressure is the principal driving force for interstitial hypertension in solid tumors: implications for vascular collapse. Cancer Res 52: 5110-5114.
12. Koumoutsakos P, Pivkin I, Milde F (2013) The fluid mechanics of cancer and its therapy. Annual Review of Fluid Mechanics 45: 325-355.
13. Jain RK, Martin JD, Stylianopoulos T (2014) The role of mechanical forces in tumor growth and therapy. Annu Rev Biomed Eng 16: 321-346.
14. Jain RK, Stylianopoulos T (2010) Delivering nanomedicine to solid tumors. Nat Rev Clin Oncol 7: 653-664.
15. Wiig H, Swartz MA (2012) Interstitial fluid and lymph formation and transport: physiological regulation and roles in inflammation and cancer. Physiol Rev 92: 1005-1060.
16. Alexandrakis G, Brown EB, Tong RT, McKee TD, Campbell RB, et al. (2004) Two-photon fluorescence correlation microscopy reveals the two-phase nature of transport in tumors. Nat Med 10: 203-207.
17. Eisenberg SR, Grodzinsky AJ (1985) Swelling of articular cartilage and other connective tissues: electromechanochemical forces. J Orthop Res 3: 148-159.

18. Wilson W, van Donkelaar CC, van Rietbergen R, Huiskes R (2005) The role of computational models in the search for the mechanical behavior and damage mechanisms of articular cartilage. Med Eng Phys 27: 810-826.
19. Swartz MA, Fleury ME (2007) Interstitial flow and its effects in soft tissues. Annu Rev Biomed Eng 9: 229-256.
20. Helmlinger G, Netti PA, Lichtenbeld HC, Melder RJ, Jain RK (1997) Solid stress inhibits the growth of multicellular tumor spheroids. Nat Biotechnol 15: 778-783.
21. Kaufman LJ, Brangwynne CP, Kasza KE, Filippidi E, Gordon VD, et al. (2005) Glioma expansion in collagen I matrices: analyzing collagen concentration-dependent growth and motility patterns. Biophys J 89: 635-650.
22. Demou ZN (2010) Gene expression profiles in 3D tumor analogs indicate compressive strain differentially enhances metastatic potential. Ann Biomed Eng 38: 3509-3520.
23. Egeblad M, Rasch MG, Weaver VM (2010) Dynamic interplay between the collagen scaffold and tumor evolution. Current opinion in cell biology 22: 697-706.
24. Cheng G, Tse J, Jain RK, Munn LL (2009) Micro-environmental mechanical stress controls tumor spheroid size and morphology by suppressing proliferation and inducing apoptosis in cancer cells. PLoS One 4: e4632.
25. Tse JM, Cheng G, Tyrrell JA, Wilcox-Adelman SA, Boucher Y, et al. (2012) Mechanical compression drives cancer cells toward invasive phenotype. Proceedings of the National Academy of Science 109: 911-916.
26. Griffon-Etienne G, Boucher Y, Brekken C, Suit HD, Jain RK (1999) Taxane-induced apoptosis decompresses blood vessels and lowers interstitial fluid pressure in solid tumors: clinical implications. Cancer Res 59: 3776-3782.
27. Padera TP, Stoll BR, Tooredman JB, Capen D, di Tomaso E, et al. (2004) Pathology: cancer cells compress intratumour vessels. Nature 427: 695.
28. Wilson WR, Hay MP (2011) Targeting hypoxia in cancer therapy. Nat Rev Cancer 11: 393-410.
29. Stylianopoulos T, Jain RK (2013) Combining two strategies to improve perfusion and drug delivery in solid tumors. Proc Natl Acad Sci U S A 110: 18632-18637.
30. Jain RK, Tong RT, Munn LL (2007) Effect of vascular normalization by antiangiogenic therapy on interstitial hypertension, peritumor edema, and lymphatic metastasis: insights from a mathematical model. Cancer Res 67: 2729-2735.
31. Swartz MA, Lund AW (2012) Lymphatic and interstitial flow in the tumour microenvironment: linking mechanobiology with immunity. Nat Rev Cancer 12: 210-219.
32. Chauhan VP, Martin JD, Liu H, Lacorre DA, Jain SR, et al. (2013) Angiotensin inhibition enhances drug delivery and potentiates chemotherapy by decompressing tumor blood vessels. Nature Communications 4: 10.1038/ncomms.3516.
33. Liu J, Liao S, Diop-Frimpong B, Chen W, Goel S, et al. (2012) TGF-beta blockade improves the distribution and efficacy of therapeutics in breast carcinoma by normalizing the tumor stroma. Proc Natl Acad Sci U S A 109: 16618-16623.
34. Provenzano PP, Cuevas C, Chang AE, Goel VK, Von Hoff DD, et al. (2012) Enzymatic targeting of the stroma ablates physical barriers to treatment of pancreatic ductal adenocarcinoma. Cancer cell 21: 418-429.
35. Gkretsi V, Stylianou A, Papageorgis P, Polydorou C, Stylianopoulos T (2015) Remodeling Components of the Tumor Microenvironment to Enhance Cancer Therapy. Front Oncol 5: 214.
36. Papageorgis P, Stylianopoulos T (2015) Role of TGFbeta in regulation of the tumor microenvironment and drug delivery (review). Int J Oncol 46: 933-943.

37. Diop-Frimpong B, Chauhan VP, Krane S, Boucher Y, Jain RK (2011) Losartan inhibits collagen I synthesis and improves the distribution and efficacy of nanotherapeutics in tumors. Proc Natl Acad Sci U S A 108: 2909-2914.
38. Pirentis AP, Polydorou C, Papageorgis P, Voutouri C, Mpekris F, et al. (2015) Remodeling of extracellular matrix due to solid stress accumulation during tumor growth. Connect Tissue Res 56: 345-354.
39. Ambrosi D, Mollica F (2002) On the mechanics of a growing tumor. International Journal of Engineering Science 40: 1297-1316.
40. Byrne H, Preziosi L (2003) Modelling solid tumour growth using the theory of mixtures. Math Med Biol 20: 341-366.
41. Roose T, Netti PA, Munn LL, Boucher Y, Jain RK (2003) Solid stress generated by spheroid growth estimated using a linear poroelasticity model. Microvasc Res 66: 204-212.
42. Sarntinoranont M, Rooney F, Ferrari M (2003) Interstitial stress and fluid pressure within a growing tumor. Ann Biomed Eng 31: 327-335.
43. Ciarletta P (2013) Buckling instability in growing tumor spheroids. Phys Rev Lett 110: 158102.
44. Netti PA, Berk DA, Swartz MA, Grodzinsky AJ, Jain RK (2000) Role of extracellular matrix assembly in interstitial transport in solid tumors. Cancer Res 60: 2497-2503.
45. Levental I, Levental KR, Klein EA, Assoian R, Miller RT, et al. (2010) A simple indentation device for measuring micrometer-scale tissue stiffness. J Phys Condens Matter 22: 194120.
46. Plodinec M, Loparic M, Monnier CA, Obermann EC, Zanetti-Dallenbach R, et al. (2012) The nanomechanical signature of breast cancer. Nat Nanotechnol 7: 757-765.
47. Rodriguez EK, Hoger A, McCulloch AD (1994) Stress-dependent finite growth in soft elastic tissues. J Biomech 27: 455-467.
48. Ambrosi D, Preziosi L (2009) Cell adhesion mechanisms and stress relaxation in the mechanics of tumours. Biomechanics and modeling in mechanobiology 8: 397-413.
49. Kim Y, Stolarska MA, Othmer HG (2011) The role of the microenvironment in tumor growth and invasion. Progress in biophysics and molecular biology 106: 353-379.
50. MacLaurin J, Chapman J, Jones GW, Roose T (2012) The buckling of capillaries in solid tumours. Proc R Soc A 468: 4123-4145.
51. Omens JH, Vaplon SM, Fazeli B, McCulloch AD (1998) Left ventricular geometric remodeling and residual stress in the rat heart. J Biomech Eng 120: 715-719.
52. Xu G, Bayly PV, Taber LA (2009) Residual stress in the adult mouse brain. Biomech Model Mechanobiol 8: 253-262.
53. Eikenberry S (2009) A tumor cord model for doxorubicin delivery and dose optimization in solid tumors. Theor Biol Med Model 6: 16.
54. Fung Y-c (2013) Biomechanics: mechanical properties of living tissues: Springer Science & Business Media.
55. Taber LA (2008) Theoretical study of Beloussov's hyper-restoration hypothesis for mechanical regulation of morphogenesis. Biomech Model Mechanobiol 7: 427-441.
56. Hagendoorn J, Tong R, Fukumura D, Lin Q, Lobo J, et al. (2006) Onset of abnormal blood and lymphatic vessel function and interstitial hypertension in early stages of carcinogenesis. Cancer Res 66: 3360-3364.
57. Branton MH, Kopp JB (1999) TGF-beta and fibrosis. Microbes Infect 1: 1349-1365.
58. Butcher DT, Alliston T, Weaver VM (2009) A tense situation: forcing tumour progression. Nat Rev Cancer 9: 108-122.

59. Shieh AC (2011) Biomechanical forces shape the tumor microenvironment. Ann Biomed Eng 39: 1379-1389.
60. Roy S, Silacci P, Stergiopulos N (2005) Biomechanical properties of decellularized porcine common carotid arteries. Am J Physiol Heart Circ Physiol 289: H1567-1576.
61. Boucher Y, Baxter LT, Jain RK (1990) Interstitial pressure gradients in tissue-isolated and subcutaneous tumors: implications for therapy. Cancer Res 50: 4478-4484.
62. Kalluri R, Zeisberg M (2006) Fibroblasts in cancer. Nat Rev Cancer 6: 392-401.
63. Nagy JA, Dvorak AM, Dvorak HF (2012) Vascular hyperpermeability, angiogenesis, and stroma generation. Cold Spring Harb Perspect Med 2: a006544.
64. Stylianopoulos T, Barocas VH (2007) Volume averaging theory for the study of the mechanics of collagen networks. Computer methods in applied mechanics and engineering 196: 2981-2990.
65. Sander EA, Stylianopoulos T, Tranquillo RT, Barocas VH (2009) Image-based biomechanics of collagen-based tissue equivalents. IEEE Eng Med Biol Mag 28: 10-18.
66. Gerlowski LE, Jain RK (1986) Microvascular permeability of normal and neoplastic tissues. Microvasc Res 31: 288-305.
67. Maeda H, Wu J, Sawa T, Matsumura Y, Hori K (2000) Tumor vascular permeability and the EPR effect in macromolecular therapeutics: a review. J Control Release 65: 271-284.
68. Chauhan VP, Stylianopoulos T, Boucher Y, Jain RK (2011) Delivery of molecular and nanomedicine to tumors: Transport barriers and strategies. Annual Reviews Chemical and Biomolecular Engineering 2: 281-298.
69. Perrault SD, Walkey C, Jennings T, Fischer HC, Chan WC (2009) Mediating tumor targeting efficiency of nanoparticles through design. Nano Lett 9: 1909-1915.
70. Cabral H, Matsumoto Y, Mizuno K, Chen Q, Murakami M, et al. (2011) Accumulation of sub-100 nm polymeric micelles in poorly permeable tumours depends on size. Nat Nanotechnol 6: 815-823.
71. Stylianopoulos T (2013) EPR-effect: utilizing size-dependent nanoparticle delivery to solid tumors. Ther Deliv 4: 421-423.
72. Tong RT, Boucher Y, Kozin SV, Winkler F, Hicklin DJ, et al. (2004) Vascular normalization by vascular endothelial growth factor receptor 2 blockade induces a pressure gradient across the vasculature and improves drug penetration in tumors. Cancer Res 64: 3731-3736.
73. Goel S, Duda DG, Xu L, Munn LL, Boucher Y, et al. (2011) Normalization of the vasculature for treatment of cancer and other diseases. Physiol Rev 91: 1071-1121.
74. Chauhan VP, Stylianopoulos T, Martin JD, Popovic Z, Chen O, et al. (2012) Normalization of tumour blood vessels improves the delivery of nanomedicines in a size-dependent manner. Nature Nanotechnology 7: 383-388.
75. Jiang W, Huang Y, An Y, Kim BY (2015) Remodeling Tumor Vasculature to Enhance Delivery of Intermediate-Sized Nanoparticles. ACS Nano 9: 8689-8696.
76. Kindler HL, Niedzwiecki D, Hollis D, Sutherland S, Schrag D, et al. (2010) Gemcitabine plus bevacizumab compared with gemcitabine plus placebo in patients with advanced pancreatic cancer: phase III trial of the Cancer and Leukemia Group B (CALGB 80303). J Clin Oncol 28: 3617-3622.
77. Jain RK (2013) Normalizing tumor microenvironment to treat cancer: bench to bedside to biomarkers. J Clin Oncol 31: 2205-2218.

78. Fadnes HO, Reed RK, Aukland K (1977) Interstitial fluid pressure in rats measured with a modified wick technique. Microvasc Res 14: 27-36.
79. Chauhan VP, Boucher Y, Ferrone CR, Roberge S, Martin JD, et al. (2014) Compression of pancreatic tumor blood vessels by hyaluronan is caused by solid stress and not interstitial fluid pressure. Cancer Cell 26: 14-15.
80. Mow VC, Kuei SC, Lai WM, Armstrong CG (1980) Biphasic creep and stress relaxation of articular cartilage in compression? Theory and experiments. J Biomech Eng 102: 73-84.
81. Platten M, Wick W, Wischhusen J, Weller M (2001) N-[3,4-dimethoxycinnamoyl]-anthranilic acid (tranilast) suppresses microglial inducible nitric oxide synthase (iNOS) expression and activity induced by interferon-gamma (IFN-gamma). Br J Pharmacol 134: 1279-1284.
82. Hiroi M, Onda M, Uchida E, Aimoto T (2002) Anti-tumor effect of N-[3,4-dimethoxycinnamoyl]-anthranilic acid (tranilast) on experimental pancreatic cancer. J Nippon Med Sch 69: 224-234.
83. Chakrabarti R, Subramaniam V, Abdalla S, Jothy S, Prud'homme GJ (2009) Tranilast inhibits the growth and metastasis of mammary carcinoma. Anticancer Drugs 20: 334-345.
84. Emblem KE, Mouridsen K, Bjornerud A, Farrar CT, Jennings D, et al. (2013) Vessel architectural imaging identifies cancer patient responders to anti-angiogenic therapy. Nat Med 19: 1178-1183.
85. Stockmann C, Doedens A, Weidemann A, Zhang N, Takeda N, et al. (2008) Deletion of vascular endothelial growth factor in myeloid cells accelerates tumorigenesis. Nature 456: 814-818.
86. Rhim AD, Mirek ET, Aiello NM, Maitra A, Bailey JM, et al. (2012) EMT and dissemination precede pancreatic tumor formation. Cell 148: 349-361.
87. Qiu W, Su GH (2013) Development of orthotopic pancreatic tumor mouse models. Methods Mol Biol 980: 215-223.
88. Kelm JM, Timmins NE, Brown CJ, Fussenegger M, Nielsen LK (2003) Method for generation of homogeneous multicellular tumor spheroids applicable to a wide variety of cell types. Biotechnol Bioeng 83: 173-180.
89. Del Duca D, Werbowetski T, Del Maestro RF (2004) Spheroid preparation from hanging drops: characterization of a model of brain tumor invasion. J Neurooncol 67: 295-303.
90. Eisenberg SR, Grodzinsky AJ (1987) The kinetics of chemically induced nonequilibrium swelling of articular cartilage and corneal stroma. J Biomech Eng 109: 79-89.
91. Casciari JJ, Sotirchos SV, Sutherland RM (1992) Variations in tumor cell growth rates and metabolism with oxygen concentration, glucose concentration, and extracellular pH. J Cell Physiol 151: 386-394.
92. Casciari JJ, Sotirchos SV, Sutherland RM (1992) Mathematical modelling of microenvironment and growth in EMT6/Ro multicellular tumour spheroids. Cell Prolif 25: 1-22.
93. Baxter LT, Jain RK (1989) Transport of fluid and macromolecules in tumors. I. Role of interstitial pressure and convection. Microvasc Res 37: 77-104.
94. Mattern KJ, Nakornchai C, Deen WM (2008) Darcy permeability of agarose-glycosaminoglycan gels analyzed using fiber-mixture and donnan models. Biophys J 95: 648-656.

95. Jin M, Grodzinsky AJ (2001) Effect of electrostatic interactions between glycosaminoglycans on the shear stiffness of cartilage: a molecular model and experiments. Macromolecules 34: 8330-8339.
96. Wilson W, van Donkelaar CC, van Rietbergen B, Huiskes R (2005) A fibril-reinforced poroviscoelastic swelling model for articular cartilage. J Biomech 38: 1195-1204.
97. Netti PA, Baxter LT, Boucher Y, Skalak R, Jain RK (1995) Time-dependent behavior of interstitial fluid pressure in solid tumors: implications for drug delivery. Cancer Res 55: 5451-5458.
98. Lesperance LM, Gray ML, Burstein D (1992) Determination of fixed charge density in cartilage using nuclear magnetic resonance. J Orthop Res 10: 1-13.
99. Jackson AR, Yuan TY, Huang CY, Gu WY (2009) A conductivity approach to measuring fixed charge density in intervertebral disc tissue. Ann Biomed Eng 37: 2566-2573.
100. Sun DN, Gu WY, Guo XE, Lai WM, Mow VC (1999) A mixed finite element formulation of triphasic mechano-electrochemical theory for charged, hydrated biological soft tissues. Int J Numer Meth Engng 45: 1375-1402.
101. Sun DN, Gu WY, Guo XE, Lai WM, Mow VC (1999) A mixed finite element formulation of triphasic mechano-electrochemical theory for charged, hydrated biological soft tissues. International Journal for Numerical Methods in Engineering 45: 1375-1402.
102. Baxter LT, Jain RK (1990) Transport of fluid and macromolecules in tumors. II. Role of heterogeneous perfusion and lymphatics. Microvasc Res 40: 246-263.
103. Peterson TE, Kirkpatrick ND, Huang Y, Farrar CT, Marijt KA, et al. (2016) Dual inhibition of Ang-2 and VEGF receptors normalizes tumor vasculature and prolongs survival in glioblastoma by altering macrophages. Proc Natl Acad Sci U S A 113: 4470-4475.
104. Muellerklieser WF, Sutherland RM (1984) Oxygen-Consumption and Oxygen Diffusion Properties of Multicellular Spheroids from 2 Different Cell-Lines. Advances in Experimental Medicine and Biology 180: 311-321.
105. Maroudas AI (1976) Balance between swelling pressure and collagen tension in normal and degenerate cartilage. Nature 260: 808-809.
106. Mow VC, Ratcliffe A, Poole AR (1992) Cartilage and diarthrodial joints as paradigms for hierarchical materials and structures. Biomaterials 13: 67-97.
107. Lai VK, Nedrelow DS, Lake SP, Kim B, Weiss EM, et al. (2016) Swelling of Collagen-Hyaluronic Acid Co-Gels: An In Vitro Residual Stress Model. Ann Biomed Eng 44: 2984-2993.
108. Jain RK (2014) Antiangiogenesis strategies revisited: from starving tumors to alleviating hypoxia. Cancer Cell 26: 605-622.
109. Facciabene A, Peng X, Hagemann IS, Balint K, Barchetti A, et al. (2011) Tumour hypoxia promotes tolerance and angiogenesis via CCL28 and T(reg) cells. Nature 475: 226-230.
110. Guo X, Lanir Y, Kassab GS (2007) Effect of osmolarity on the zero-stress state and mechanical properties of aorta. Am J Physiol Heart Circ Physiol 293: H2328-2334.
111. Azeloglu EU, Albro MB, Thimmappa VA, Ateshian GA, Costa KD (2008) Heterogeneous transmural proteoglycan distribution provides a mechanism for regulating residual stresses in the aorta. Am J Physiol Heart Circ Physiol 294: H1197-1205.
112. Lanir Y (2012) Osmotic swelling and residual stress in cardiovascular tissues. J Biomech 45: 780-789.

113. Papageorgis P, Polydorou C, Mpekris F, Voutouri C, Agathokleous E, et al. (2017) Tranilast-induced stress alleviation in solid tumors improves the efficacy of chemo- and nanotherapeutics in a size-independent manner. Sci Rep 7: 46140.
114. Polydorou C, Mpekris F, Papageorgis P, Voutouri C, Stylianopoulos T (2017) Pirfenidone normalizes the tumor microenvironment to improve chemotherapy. Oncotarget 8: 24506-24517.
115. Wirtz D, Konstantopoulos K, Searson PC (2011) The physics of cancer: the role of physical interactions and mechanical forces in metastasis. Nat Rev Cancer 11: 512-522.
116. Nia HT, Liu H, Seano G, Datta M, Jones D, et al. (2016) Solid stress and elastic energy as measures of tumour mechanopathology. Nature Biomedical Engineering 1: 0004.
117. Buschmann MD, Grodzinsky AJ (1995) A molecular model of proteoglycan-associated electrostatic forces in cartilage mechanics. J Biomech Eng 117: 179-192.
118. Nieskoski MD, Marra K, Gunn JR, Kanick SC, Doyley MM, et al. (2017) Separation of Solid Stress From Interstitial Fluid Pressure in Pancreas Cancer Correlates With Collagen Area Fraction. J Biomech Eng 139.
119. Alessandri K, Sarangi BR, Gurchenkov VV, Sinha B, Kießling TR, et al. (2013) Cellular capsules as a tool for multicellular spheroid production and for investigating the mechanics of tumor progression in vitro. Proceedings of the National Academy of Sciences 110: 14843-14848.
120. Mpekris F, Angeli S, Pirentis AP, Stylianopoulos T (2015) Stress-mediated progression of solid tumors: effect of mechanical stress on tissue oxygenation, cancer cell proliferation, and drug delivery. Biomech Model Mechanobiol.
121. Voutouri C, Stylianopoulos T (2014) Evolution of osmotic pressure in solid tumors. J Biomech 47: 3441-3447.
122. Martin JD, Fukumura D, Duda DG, Boucher Y, Jain RK (2016) Reengineering the Tumor Microenvironment to Alleviate Hypoxia and Overcome Cancer Heterogeneity. Cold Spring Harb Perspect Med 6.
123. Deen WM (1987) Hindered Transport of Large Molecules in Liquid-Filled Pores. Aiche Journal 33: 1409-1425.
124. Mpekris F, Baish JW, Stylianopoulos T, Jain RK (2017) Role of vascular normalization in benefit from metronomic chemotherapy. Proc Natl Acad Sci U S A 114: 1994-1999.
125. Xu G, Kemp PS, Hwu JA, Beagley AM, Bayly PV, et al. (2010) Opening angles and material properties of the early embryonic chick brain. J Biomech Eng 132: 011005.
126. Kerr DJ, Kerr AM, Freshney RI, Kaye SB (1986) Comparative intracellular uptake of adriamycin and 4'-deoxydoxorubicin by non-small cell lung tumor cells in culture and its relationship to cell survival. Biochem Pharmacol 35: 2817-2823.
127. Stylianopoulos T, Economides EA, Baish JW, Fukumura D, Jain RK (2015) Towards Optimal Design of Cancer Nanomedicines: Multi-stage Nanoparticles for the Treatment of Solid Tumors. Ann Biomed Eng 43: 2291-2300.
128. Mok W, Stylianopoulos T, Boucher Y, Jain RK (2009) Mathematical modeling of herpes simplex virus distribution in solid tumors: implications for cancer gene therapy. Clin Cancer Res 15: 2352-2360.
129. Schmidt MM, Wittrup KD (2009) A modeling analysis of the effects of molecular size and binding affinity on tumor targeting. Mol Cancer Ther 8: 2861-2871.

130. Pluen A, Boucher Y, Ramanujan S, McKee TD, Gohongi T, et al. (2001) Role of tumor-host interactions in interstitial diffusion of macromolecules: cranial vs. subcutaneous tumors. Proc Natl Acad Sci U S A 98: 4628-4633.
131. Jackson GW, James DF (1986) The Permeability of Fibrous Porous-Media. Canadian Journal of Chemical Engineering 64: 364-374.
132. Izumi Y, Xu L, di Tomaso E, Fukumura D, Jain RK (2002) Tumour biology: herceptin acts as an anti-angiogenic cocktail. Nature 416: 279-280.
133. Folkman J (1990) What is the evidence that tumors are angiogenesis dependent? J Natl Cancer Inst 82: 4-6.
134. Folkman J (1971) Tumor angiogenesis: therapeutic implications. N Engl J Med 285: 1182-1186.
135. Yancopoulos GD, Davis S, Gale NW, Rudge JS, Wiegand SJ, et al. (2000) Vascular-specific growth factors and blood vessel formation. Nature 407: 242-248.
136. Wesseling P, van der Laak JA, de Leeuw H, Ruiter DJ, Burger PC (1994) Quantitative immunohistological analysis of the microvasculature in untreated human glioblastoma multiforme. Computer-assisted image analysis of whole-tumor sections. J Neurosurg 81: 902-909.
137. Pezzella F, Pastorino U, Tagliabue E, Andreola S, Sozzi G, et al. (1997) Non-small-cell lung carcinoma tumor growth without morphological evidence of neo-angiogenesis. Am J Pathol 151: 1417-1423.
138. Pezzella F, Gatter K (2015) Non-angiogenic tumours unveil a new chapter in cancer biology. J Pathol 235: 381-383.
139. Holash J, Maisonpierre PC, Compton D, Boland P, Alexander CR, et al. (1999) Vessel cooption, regression, and growth in tumors mediated by angiopoietins and VEGF. Science 284: 1994-1998.
140. Jain RK, di Tomaso E, Duda DG, Loeffler JS, Sorensen AG, et al. (2007) Angiogenesis in brain tumours. Nat Rev Neurosci 8: 610-622.
141. Hardee ME, Zagzag D (2012) Mechanisms of glioma-associated neovascularization. Am J Pathol 181: 1126-1141.
142. Kamoun WS, Ley CD, Farrar CT, Duyverman AM, Lahdenranta J, et al. (2009) Edema control by cediranib, a vascular endothelial growth factor receptor-targeted kinase inhibitor, prolongs survival despite persistent brain tumor growth in mice. J Clin Oncol 27: 2542-2552.
143. Rubenstein JL, Kim J, Ozawa T, Zhang M, Westphal M, et al. (2000) Anti-VEGF antibody treatment of glioblastoma prolongs survival but results in increased vascular cooption. Neoplasia 2: 306-314.
144. Du R, Lu KV, Petritsch C, Liu P, Ganss R, et al. (2008) HIF1alpha induces the recruitment of bone marrow-derived vascular modulatory cells to regulate tumor angiogenesis and invasion. Cancer Cell 13: 206-220.
145. Kunkel P, Ulbricht U, Bohlen P, Brockmann MA, Fillbrandt R, et al. (2001) Inhibition of glioma angiogenesis and growth in vivo by systemic treatment with a monoclonal antibody against vascular endothelial growth factor receptor-2. Cancer Res 61: 6624-6628.
146. Kim ES, Serur A, Huang J, Manley CA, McCrudden KW, et al. (2002) Potent VEGF blockade causes regression of coopted vessels in a model of neuroblastoma. Proc Natl Acad Sci U S A 99: 11399-11404.
147. Kuczynski EA, Yin M, Bar-Zion A, Lee CR, Butz H, et al. (2016) Co-option of Liver Vessels and Not Sprouting Angiogenesis Drives Acquired Sorafenib Resistance in Hepatocellular Carcinoma. J Natl Cancer Inst 108.

148. Bentolila LA, Prakash R, Mihic-Probst D, Wadehra M, Kleinman HK, et al. (2016) Imaging of Angiotropism/Vascular Co-Option in a Murine Model of Brain Melanoma: Implications for Melanoma Progression along Extravascular Pathways. Sci Rep 6: 23834.
149. Reiss Y, Knedla A, Tal AO, Schmidt MH, Jugold M, et al. (2009) Switching of vascular phenotypes within a murine breast cancer model induced by angiopoietin-2. J Pathol 217: 571-580.
150. Winkler F, Kienast Y, Fuhrmann M, Von Baumgarten L, Burgold S, et al. (2009) Imaging glioma cell invasion in vivo reveals mechanisms of dissemination and peritumoral angiogenesis. Glia 57: 1306-1315.
151. Kruse CA, Molleston MC, Parks EP, Schiltz PM, Kleinschmidt-DeMasters BK, et al. (1994) A rat glioma model, CNS-1, with invasive characteristics similar to those of human gliomas: a comparison to 9L gliosarcoma. J Neurooncol 22: 191-200.
152. Szatmari T, Lumniczky K, Desaknai S, Trajcevski S, Hidvegi EJ, et al. (2006) Detailed characterization of the mouse glioma 261 tumor model for experimental glioblastoma therapy. Cancer Sci 97: 546-553.
153. Kodack DP, Askoxylakis V, Ferraro GB, Sheng Q, Badeaux M, et al. (2017) The brain microenvironment mediates resistance in luminal breast cancer to PI3K inhibition through HER3 activation. Sci Transl Med 9.
154. Kodack DP, Chung E, Yamashita H, Incio J, Duyverman AMMJ, et al. (2012) Combined targeting of HER2 and VEGFR2 for effective treatment of HER2-amplified breast cancer brain metastases. Proceedings of the National Academy of Sciences of the United States of America 109: E3119-E3127.
155. Lobov IB, Brooks PC, Lang RA (2002) Angiopoietin-2 displays VEGF-dependent modulation of capillary structure and endothelial cell survival in vivo. Proc Natl Acad Sci U S A 99: 11205-11210.
156. Zagzag D, Lukyanov Y, Lan L, Ali MA, Esencay M, et al. (2006) Hypoxia-inducible factor 1 and VEGF upregulate CXCR4 in glioblastoma: implications for angiogenesis and glioma cell invasion. Lab Invest 86: 1221-1232.
157. Holash J, Wiegand SJ, Yancopoulos GD (1999) New model of tumor angiogenesis: dynamic balance between vessel regression and growth mediated by angiopoietins and VEGF. Oncogene 18: 5356-5362.
158. Chaplain MA (2000) Mathematical modelling of angiogenesis. J Neurooncol 50: 37-51.
159. Stoll BR, Migliorini C, Kadambi A, Munn LL, Jain RK (2003) A mathematical model of the contribution of endothelial progenitor cells to angiogenesis in tumors: implications for antiangiogenic therapy. Blood 102: 2555-2561.
160. Gevertz JL, Torquato S (2006) Modeling the effects of vasculature evolution on early brain tumor growth. J Theor Biol 243: 517-531.
161. Macklin P, McDougall S, Anderson AR, Chaplain MA, Cristini V, et al. (2009) Multiscale modelling and nonlinear simulation of vascular tumour growth. J Math Biol 58: 765-798.
162. Cai Y, Wu J, Li Z, Long Q (2016) Mathematical Modelling of a Brain Tumour Initiation and Early Development: A Coupled Model of Glioblastoma Growth, Pre-Existing Vessel Co-Option, Angiogenesis and Blood Perfusion. PLoS One 11: e0150296.
163. Vilanova G, Colominas I, Gomez H (2017) Computational Modeling of Tumor-Induced Angiogenesis. Archives of Computational Methods in Engineering.

164. Schugart RC, Friedman A, Zhao R, Sen CK (2008) Wound angiogenesis as a function of tissue oxygen tension: a mathematical model. Proc Natl Acad Sci U S A 105: 2628-2633.
165. Plank MJ, Sleeman BD, Jones PF (2004) The role of the angiopoietins in tumour angiogenesis. Growth Factors 22: 1-11.
166. Skalak R, Zargaryan S, Jain RK, Netti PA, Hoger A (1996) Compatibility and the genesis of residual stress by volumetric growth. J Math Biol 34: 889-914.
167. Watkins S, Robel S, Kimbrough IF, Robert SM, Ellis-Davies G, et al. (2014) Disruption of astrocyte-vascular coupling and the blood-brain barrier by invading glioma cells. Nat Commun 5: 4196.
168. Cao Y, Li CY, Moeller BJ, Yu D, Zhao Y, et al. (2005) Observation of incipient tumor angiogenesis that is independent of hypoxia and hypoxia inducible factor-1 activation. Cancer Res 65: 5498-5505.
169. Fukumura D, Xavier R, Sugiura T, Chen Y, Park EC, et al. (1998) Tumor induction of VEGF promoter activity in stromal cells. Cell 94: 715-725.
170. Olsen L, Sherratt JA, Maini PK (1995) A mechanochemical model for adult dermal wound contraction and the permanence of the contracted tissue displacement profile. J Theor Biol 177: 113-128.
171. Namy P, Ohayon J, Tracqui P (2004) Critical conditions for pattern formation and in vitro tubulogenesis driven by cellular traction fields. J Theor Biol 227: 103-120.
172. Hermann PC, Huber SL, Herrler T, Aicher A, Ellwart JW, et al. (2007) Distinct populations of cancer stem cells determine tumor growth and metastatic activity in human pancreatic cancer. Cell Stem Cell 1: 313-323.
173. Gaffney EA, Pugh K, Maini PK, Arnold F (2002) Investigating a simple model of cutaneous wound healing angiogenesis. J Math Biol 45: 337-374.
174. Sherratt JA, Murray JD (1990) Models of epidermal wound healing. Proc Biol Sci 241: 29-36.
175. Stokes CL, Lauffenburger DA (1991) Analysis of the roles of microvessel endothelial cell random motility and chemotaxis in angiogenesis. J Theor Biol 152: 377-403.
176. Baldwin ME, Catimel B, Nice EC, Roufail S, Hall NE, et al. (2001) The specificity of receptor binding by vascular endothelial growth factor-d is different in mouse and man. J Biol Chem 276: 19166-19171.
177. Makinen T, Veikkola T, Mustjoki S, Karpanen T, Catimel B, et al. (2001) Isolated lymphatic endothelial cells transduce growth, survival and migratory signals via the VEGF-C/D receptor VEGFR-3. EMBO J 20: 4762-4773.
178. Ristimaki A, Narko K, Enholm B, Joukov V, Alitalo K (1998) Proinflammatory cytokines regulate expression of the lymphatic endothelial mitogen vascular endothelial growth factor-C. J Biol Chem 273: 8413-8418.